Imperial College London

Department of Electrical and Electronic Engineering

Optical and Semiconductor Devices Group

Thin Film Detector for Internal MRI

By

Khoonsake Segkhoonthod

A thesis submitted in fulfilment for the degree of

Doctor of Philosophy

February 2014

Declaration

I herewith certify that all material in this dissertation entitled, '*Thin Film Detector for Internal MRI*' and the work in it is my own. Other work that is not my own has been appropriately referenced and acknowledged.

Khoonsake Segkhoonthod

Copyright Declaration

‘The copyright of this thesis rests with the author and is made available under a Creative Commons Attribution Non-Commercial No Derivatives licence. Researchers are free to copy, distribute or transmit the thesis on the condition that they attribute it, that they do not use it for commercial purposes and that they do not alter, transform or build upon it. For any reuse or redistribution, researchers must make clear to others the licence terms of this work’

Abstract

Thin film detectors that combine a flexible microcoil with a flexible transmission line are presented, for in vivo magnetic resonance imaging of the human bile duct. The thin-film format allows integration on a catheter, which may then be delivered into the duct with the help of a guidewire using a non-magnetic side opening endoscope. The high filling factor obtained using this approach provides very high Signal-to-Noise Ratio (SNR) and image quality, but the overall procedure is much less invasive than surgical intrabiliary MRI.

In this thesis, two models are proposed. The first has a multi-turn spiral with integrated tuning and matching capacitors as a detector coil, and a photonic bandgap structure with a periodically patterned ground plane as a transmission line. Commercial electromagnetic modelling software (AWR Microwave Office) is used to perform a detailed analysis of a complete detector system. Coil and cable are both modelled using Axiem, a method of moments solver. Analysis of the reflection and transmission coefficient is used to extract parameters such as characteristic impedance and propagation loss. Parameters are chosen for operation at 63.8 MHz (^{1}H MRI at 1.5T) with a 50 Ω system impedance.

Because the first design was implemented without considering MR-safety, a second-generation system was developed. This design uses a figure-of-eight shaped coil used as a detector and also as the resonant element in a magneto-inductive transmission line. As a result, coupling to both the B_1 and E fields of the transmitter is prevented. AWR Microwave Office is, again, used to perform a detailed design. Additional electrical parameters such as coupling coefficient, and mutual inductance of the cable are measured and extracted. Mismatch impedance is solved using transformer matching. Analytic models of both designs are also developed and compared with simulation data and to experimental data from prototypes fabricated using copper-clad Kapton.

Acknowledgements

This thesis was dedicated to my yearning to learn and experience new things even my undergraduate background was not directly related to my PhD project. I would like to express my deep gratitude to Professor Richard Syms for everything especially his excellent guidance, inspiration, encouragement, helpful suggestion, and insight feedback which I have learned to become an independent researcher throughout my PhD study. I also would like to thank him for offering me the opportunity to work in a wonderful research group, 'Optical and Semiconductor devices (OSD) research group', focusing on the health problems of Thailand (Cholangiocarcinoma in my hometown).

I am very thankful to my colleagues in OSD group – Dr. Ahmad Munir, Dr. Timmy Flume, Dr. Oleksiy Sydoruk, and all my friends in the group for a warm working environment at Imperial College London.

I would like to express my gratitude to my extended family, all my teachers and friends, my colleagues in Thailand and in the UK and the Thai music circle in the UK, who always encourage me throughout this journey. Special thanks must go to my parents, Serm and Sudjai Segkhoonthod, who always believe in me and support whatever decision I have made. I would not be a person who I am today without them.

Last but not least, I am greatly indebted to my beloved home country (the Kingdom of Thailand, where I was born, raised, and educated) for the sponsorship. It is my intention to use the knowledge and experiences I have learned in the UK to serve and develop my country.

Table of Contents

Declaration 2

Copyright Declaration 3

Abstract 4

Acknowledgements 5

Table of Contents 6

List of Figures 10

List of Tables 18

Abbreviations 19

1. THESIS OVERVIEW 21

2. BACKGROUND, MOTIVATION, AND OBJECTIVE 24

2.1 Anatomy of Liver and Ductal System Biliary 24

2.2 Cholangiocarcinoma 25

2.3 Endoscopic Retrograde Cholangiopancreatography (ERCP) 28

2.4 Magnetic Resonance Imaging 30

2.5 Magnetic Resonance Cholangiopancreatography (MRCP) 40

2.6 Intrabiliary MRI 41

2.7 Research Objective 43

3. LITERATURE REVIEW 46

3.1 RF Receiver Coil 46

3.2 Development of RF Coils for Internal MRI 50

3.3 Flexible RF Detector for Intrabiliary MRI 53

3.4 Periodically Loaded Transmission Lines 56

4. PERIODICALLY STRUCTURED THIN-FILM CABLES 61

4.1 System Overview 61

4.2 RF Microcoil Design 62

4.3 RF Microcoil Modeling and Simulation Set Up 63

4.4 RF Microcoil Simulation Result 64

4.5 RF Microcoil Experimental Performance 64

4.6 Thin-film Cable Design 66

4.7 Thin-film Cable Analytical Model and Theoretical Equation 70

4.8 Thin-film Cable Modelling and Simulation Set Up 72

4.9 Thin-film Cable Simulation Results 73

4.10 Thin-film Cable Capacitance and Inductance Extraction 80

4.11 Thin-film Cable Loss Estimation 82

4.12 Thin-film Cable Experimental Verification 85

4.13 Thin-film Cable Miniaturization 89

4.14 Whole System Simulation Result 91

4.15 Discussion 92

4.16 Magnetic Resonance Imaging 93

4.17 Publication 94

5. MR-Safe Thin-Film Cables 95

5.1 RF Heating 95

5.2 Safe Transmission Lines 98

5.2.1 Coaxial Cable with Chokes 99

5.2.2 Coaxial Cable with Transformers 100

5.2.3 Coaxial Cable with Figure-of-Eight-Shaped Transformers 100

5.2.4 Magneto-Inductive Cable 101

5.3 Second Generation MR-Safe Thin-Film Cable 107

5.4 MR-Safe Thin-Film Cable Simulation Results 108

5.5 MR-Safe Cable Experimental Verification 113

5.6 MR-Safe Thin-Film Cable Simulation Correction 115

5.7 Overall Receiver Design 119

5.8 Lumped Element Demonstration of Matching 122

5.9 Electromagnetic Demonstration of Matching 125

5.10 Simulation of Complete MR-safe Cable 128

5.11 Parasitic Capacitance 131

5.12 Experimental Verification of Detector Integrated with MR-Safe Thin-film Cable 132

5.13 Endoscopic Application 134

5.14 Magnetic Resonance Imaging 135

5.15 Discussion 137

5.16 Publication 137

6. HEATING EFFECT 138

6.1 MR Safety and Compatibility Standards 138

6.2 MR Biological Models 140

6.3 Capacitor-Segmented Transmission Lines 142

6.4 Numerical Evaluation of Parasitic Capacitance 153
6.5 Numerical Evaluation of Surface Wave Propagation 156
6.6 Magnetic Decoupling 161
6.7 Electric Decoupling 163
6.8 SAR Measurement 165
6.9 Numerical Simulation of Complete MR-safe Systems 167
6.10 Magnetic Resonance Imaging 169
6.11 Discussion 171
6.12 Publication 171

7. CONCLUSIONS AND FUTURE WORKS 172
7.1 Contributions 172
7.2 Future Work 174

APPENDIX A: Electromagnetic Analysis Software 176
Electromagnetic Solvers in Microwave Office (MWO) 177
Electromagnetic Solvers in Computer Simulation Technology (CST) 179

APPENDIX B: Measurement of tan δ 181

APPENDIX C: MATLAB Codes in the Study of MR-Safe Scattering Parameters Estimation 188

References 191

List of Figures

Chapter 2

Figure 2.1 The anatomy of the biliary system and related organs 25
Figure 2.2 (a) Three main regions of the biliary tract; (b) four types of CCA according to the Bismuth classification [1] 26
Figure 2.3 The incidence of Cholangiocarcinoma by province in Thailand [5] 27
Figure 2.4 Endoscope used in ERCP, and location of the endoscope during the procedure [7] 29
Figure 2.5 X-ray fluoroscopy image obtained during ERCP [8] 29
Figure 2.6 Non-aligned protons forming a random distribution of magnetic dipoles [11]..... 30
Figure 2.7 (a) The energy levels of a spin ½ system [9, 10] (b) The two orientations of a spinning proton aligned by an external magnetic field B_0 [11] 32
Figure 2.8 Division of magnetic moment into longitudinal (Mz) and transverse (Mxy) components 34
Figure 2.9 The NET magnetization when (a) before RF pulse (b) during the excitation (c) during the relaxation 35
Figure 2.10 Relaxations (a) T_1 (b) T_2 recorded by a RF receiver coil 36
Figure 2.11 Basic gradient echo MR imaging sequences [12] 37
Figure 2.12 K-space used to convert a signal into an MR image [12]..... 38
Figure 2.13 Cutaway image of a conventional MRI scanner [13] 39
Figure 2.14 Rigid and flexible RF chest coil [15] 40
Figure 2.15 X-ray image of the biliary tree, with a red arrow showing two gallstones in the common bile duct [8] 41
Figure 2.16 Rigid body coil versus miniature coil in a cross-section of the human body..... 42
Figure 2.17 The picture of tumour and adjacent tissue by intrabiliary MRI [18]..... 43
Figure 2.18 Nonferrous components used in this work (a) non-magnetic gastroscope (b) catheter passed through the biopsy channel and bent 90 degree at the distal end 44

Chapter 3

Figure 3.1 The receiver coil equivalent circuit 47
Figure 3.2 Frequency variation of impedance found from Equation (3.1), for the parameters of a typical experimental microcoil 49
Figure 3.3 L-C resonator used for signal reception with additional PIN diode-switched tank filter to decouple the resonator from the transmitter 49
Figure 3.4 (a) Opposed solenoid coil, (b) and equivalent circuit [21] 50
Figure 3.5 (a) Photograph of parallel conductor coil (b) 3D model of coil construction [22] 51
Figure 3.6 Loopless catheter antenna (A) inner conductor (B) primary shield (C) secondary shield (D) insulator [23] 51
Figure 3.7 a 3D model of a nonobstructive IV MR coil from [24] 52
Figure 3.8 Top view of planar microcoil [31] 53
Figure 3.9 A circular planar microcoil on glass substrate [36] 54
Figure 3.10 Two coil designs developed by Imperial College London (a) Type I catheter-based flexible micro coil [41] (b) Type II coil [41] 56
Figure 3.11 Equivalent circuit of a transmission line 57
Figure 3.12 Dispersion diagram for a periodic line calculated using Matlab following Equation (3.6) 58
Figure 3.13 Discontinuity in transmission line impedance at z = 0 [44] 59
Figure 3.14 Input impedance for a finite line [44] 59

Chapter 4

Figure 4.1 Thin-film RF detection system 61
Figure 4.2 Integration of the RF receiver on a catheter scaffold 62
Figure 4.3 Layout of flexible microcoil 62
Figure 4.4 Initial definition of layer structure, used for resonant coil 63
Figure 4.5 RF microcoil numerical testing: (a) arrangement in AWR, and (b) frequency variation of the reflection coefficient S_{11} of the detector 64
Figure 4.6 Experimental frequency variation of the scattering parameters of a thin-film RF detector; (a) arrangement of the RF detector with an additional transducer; (b) frequency

variation of the reflection coefficient S_{11}; (c) frequency variation of the transmission coefficient S_{21} 65
Figure 4.7 The microstrip with the physical variable used for calculating impedance [48].. 66
Figure 4.8 The coplanar waveguide with physical parameters for calculating impedance [49] 67
Figure 4.9 Variation of characteristic impedance with conductor width for microstrip and CPW on 25 mm polyimide 68
Figure 4.10 Variation of characteristic impedance with electrode gap for CPW 68
Figure 4.11 Photonic-bandgap transmission line 69
Figure 4.12 (a) Equivalent circuit for a diatomic electrical lattice [58] (b) physical structure of a microstrip with a periodically patterned ground plan 70
Figure 4.13 Equivalent circuit for a cable model based on a P unit cell 71
Figure 4.14 Meshed structure with (a) low and (b) high mesh density 73
Figure 4.15 (a) 9 sections of PBG microstrip with periodically patterned ground plane (b) Frequency dependence of S_{11} and S_{21} with b/a = 0.5 74
Figure 4.16 Comparison of the variations of impedance predicted by the numerical and analytic models (Equation (4.9)) 78
Figure 4.17 Frequency variation of impedance, for several values of β 78
Figure 4.18 Variation of DC impedance with β, for different PBG waveguide models 79
Figure 4.19 Extracted variation of the cutoff frequency f_m with β 80
Figure 4.20 Variation of extracted values of (a) capacitance and (b) inductance with $\beta = b/a$ 81
Figure 4.21 Equivalent circuit of lossy transmission line 82
Figure 4.22 Analytic variation of PBG waveguide propagation loss with $\beta = b/a$ 84
Figure 4.23 Numerical variation of PBG waveguide propagation loss with $\beta = b/a$ 85
Figure 4.24 Process for thin-film PBG cable fabrication 86
Figure 4.25 Experimental frequency variation of the scattering parameters of thin film PBG cable (a) S_{21} and (b) S_{11} 87
Figure 4.26 Experimental variation of DC characteristic impedance with the layout parameter b/a 87
Figure 4.27 Comparison between experimental and theoretical variations of impedance for conductor widths of (a) 0.5 mm and (b) 1.0 mm 88

Figure 4.28 Experimental variation of low-frequency propagation loss with ratio *b/a* 89
Figure 4.29 Photonic band gap waveguide (PBG) and alternative PBG waveguide (APBG) 90
Figure 4.30 Variation of DC impedance with β for designs aimed at improving flexibility .. 91
Figure 4.31 Simulated frequency variation of (a) whole system when the cable connected to RF coil (b) S_{11} and (c) S_{21} for a complete thin film receiver 92
Figure 4.32 (a) Cable array, and (b) cable mounted on catheter [45] 93
Figure 4.33 (a) Resected porcine liver, with the catheter receiver inserted into a duct; (b) ^{1}H MR image of biliary tissue [45] 94

Chapter 5

Figure 5.1 (a) experimental set-up for measuring RF heating during MRI showing an oblong bath filled with saline (b) variation of temperature with the immersed length of guidewire [64] 98
Figure 5.2 A safe transmission line based on periodically inserted chokes [83] 99
Figure 5.3 (a) layout and (b) realisation of a coaxial cable with transformer subdivision [86] 100
Figure 5.4 Figure-eight-shaped transformer (a) B_1 field decoupling in a figure-of-eight shaped coil (b) figure-of-eight shaped coils in a MR-safe transmission line [87] 101
Figure 5.5 Equivalent circuit of a magneto-inductive waveguide 103
Figure 5.6 MI waveguides in (a) axial and (b) planar configurations [112] 105
Figure 5.7 Dispersion relations of (a) axial arrangement supporting forward wave propagation, and (b) planar configuration supporting backward waves 105
Figure 5.8 3D model of a single resonant element of magneto-inductive cable developed at Imperial College [119] 106
Figure 5.9 Layout parameters and 3D structure of second-generation MR-safe cable 108
Figure 5.10 Single element of MI thin-film cable modelled by AWR MWO 109
Figure 5.11 Numerical frequency variation of scattering parameters of a single element obtains using MWO; (a) reflection coefficient – S_{11} and (b) transmission coefficient – S_{21} 110
Figure 5.12 Coupled resonant elements modelled by AWR MWO 111

Figure 5.13 Numerical frequency variation of scattering parameters of coupled resonant elements obtained using MWO; (a) reflection coefficient – S_{11} and (b) transmission coefficient – S_{21} 111
Figure 5.14 Array of MR-safe cables fabricated by the UK Company Clarydon 114
Figure 5.15 Experimental frequency variation of scattering parameters of different thin-film cables; (a) reflection coefficient – S_{11} (b) transmission coefficient – S_{21} 114
Figure 5.16 FastHenry simulation of coupled element system (a) two-inductor model (b) variation of κ with W_L, T_L, and the offset of the right hand side inductor..... 116
Figure 5.17 Variation of coupling coefficient κ with inductor width W_L obtained using AWR MWO 117
Figure 5.18 Variation of resonant frequency f_0 with capacitor length D_C 117
Figure 5.19 Variation of Q-factor Q_0 with conductivity σ 118
Figure 5.20 Complete receiver , with resonant detector, MR-safe cable and coupling transducer 120
Figure 5.21 Circuit arrangement during matching of the transducer..... 122
Figure 5.22 Frequency variation of S_{11} obtained at (a) the start, and (b) the end of the transducer matching process 123
Figure 5.23 Circuit arrangement during matching of the detector..... 124
Figure 5.24 S_{11} and S_{21} measurement after matching of the detector..... 124
Figure 5.25 Alternative RF detectors based on (a) single turn and (b) two-turn inductors .. 125
Figure 5.26 Detachable taps based on (a) single-turn and (b) two-turn transducers 126
Figure 5.27 Catheter mounting of the complete RF receiver..... 127
Figure 5.28 AWR model of a MR-safe cable with broadband transducers 128
Figure 5.29 Variations of S_{11} and S_{21} with frequency for a 9-section MR-safe cable with broadband transducers, predicted by Matlab and AWR MWO 129
Figure 5.30 AWR model of 9-section MI cable with a two-turn tap and a resonant detector 130
Figure 5.31 Variation of S_{11} and S_{21} with frequency for a MR-safe receiver based on a single turn detector and a two-turn transducer, as predicted by Matlab and AWR MWO 131
Figure 5.32 High frequency performance of the systems in Figure 5.27 and Figure 5.28 ... 132
Figure 5.33 Experimental PCB panel, showing resonant detectors integrated with MR-safe cables..... 133

Figure 5.34 Response of completed experimental catheter receiver in air 133
Figure 5.35 Catheter passing gastroscope, at (a) proximal and (b) distal ends 134
Figure 5.36 Response of completed experimental catheter receiver in gastroscope 135
Figure 5.37 Arrangements for magnetic resonance imaging 136
Figure 5.38 ^{1}H MR imaging results: (a) phantom, showing catheter track and (b) tomato . 136

Chapter 6

Figure 6.1 Material composition of immersed catheter receiver 140
Figure 6.2 Frequency variations of body tissue dielectric parameters: (a) dielectric permittivity and (b) conductivity [131] 141
Figure 6.3 HUGO anatomical model used to model heating effects in CST [132] 141
Figure 6.4 Infinite transmission line periodically loaded with capacitors 143
Figure 6.5 Dispersion diagram for an infinite capacitor-loaded line, for normalised impedances of (a) Z_n = 0.01 and (b) Z_n = 0.5 147
Figure 6.6 Finite transmission line periodically loaded with capacitors 148
Figure 6.7 Variation of the lowest-order normalised resonant frequency with Z_n, for lines with different numbers of segments 151
Figure 6.8 MR-safe cable (a) full 3D model, (b) and (b) 3D and 2D layout of the common mode path, (d) capacitors contributing to C_S (e) equivalent circuit of common mode path . 153
Figure 6.9 Layout used for simulation of parasitic capacitance 154
Figure 6.10 AWR model for parasitic capacitance simulation 154
Figure 6.11 Variation of parasitic capacitance with heatshrink thickness t_6 156
Figure 6.12 Electrical transducer: (a) half-wave dipole (b) corresponding frequency variation of S_{11} 157
Figure 6.13 Layout used for simulation of immersed wires 158
Figure 6.14 Variation of effective relative dielectric constant with cover layer thickness .. 158
Figure 6.15 Variation of κ with W_L, f_0 with L_C, and Q_0 with σ for MR-safe cable in different environments (air and polyolefin) 160
Figure 6.16 Simulation of magnetic decoupling (a) less uniform excitation (b) more uniform excitation 161

Figure 6.17 Frequency variation of S_{21} predicted by AWR during magnetic excitation by (a) small and (b) large external coils 162
Figure 6.18 Simulation of electric decoupling models 163
Figure 6.19 Frequency variation of transmission coefficient (S_{21}) predicted by AWR for (a) conductive wire and (b) MR-safe cable with electrical excitation 165
Figure 6.20 Excitation of MR-safe cable in the CST simulation 166
Figure 6.21 SAR maps on the XY, XZ, and YZ planes for (a) continuous conductor and (b) MR-safe cable 167
Figure 6.22 Frequency variation of S_{11} and S_{21}, as predicted by Matlab and AWR in air and plastic environments, for (a) point-to-point link, and (b) resonant detector with a MR-safe cable 168
Figure 6.23 Arrangement for MR imaging [136] 169
Figure 6.24 Coronal images of racetrack catheter on cuboid phantom obtained using (a) the body coil and (b) the catheter coil [136] 170

Appendix A

Figure A.1 Axiem's enclosure box environment [138] 178
Figure A.2 Excitation ports provided by MWO (a) edge and (b) differential [138] 178
Figure A.3 Meshing mechanism of MWO (a) original (b) meshed by EM Sight (c) meshed by Axiem 179
Figure A.4 Meshing types in CST MWS 180

Appendix B

Figure B.1 Non-ideal capacitor modelled as an ideal capacitor connected in series with ESR 181
Figure B.2 Frequency dependence of (a) dielectric constant (b) dissipation factor [59] 182
Figure B.3 Effect of humidity on the values of (a) dielectric constant (b) dissipation factor , and effect of temperature on the values of (c) dielectric constant (d) dissipation factor [59] 183
Figure B.4 L-C resonator using a piece of high quality wire and a Kapton-based capacitor 184

Figure B.5 Experimental L-C resonators for measuring Q-factor and dissipation factor.... 185
Figure B.6 Experimental variation of *tan δ* with frequency 186
Figure B.7 Comparison of experimental and numerical results obtained with tan δ = 0.0060 and 0.0018: (a) variation of Q factor with frequency (b) variation of loss with frequency.. 187

List of Tables

Chapter 3

Table 3.1 Properties of various plastic materials 55

Chapter 4

Table 4.1 Parameters of simulated PBG cable designs..... 70
Table 4.2 Parameters used for modelling 73
Table 4.3 The extracted impedance variation for b/a = 0.25 76
Table 4.4 Theoretical data predicted from Equation (4.9), for comparison with Table 4.3 .. 77
Table 4.5 Design variants investigated to improve mechanical performance 90

Chapter 5

Table 5.1 Capacitor length of second-generation MI cable variants 108
Table 5.2 Extracted data for the different types of resonant element 113
Table 5.3 Dimensional parameters of the old and new models used in the simulations 119
Table 5.4 Corresponding electrical parameters obtained from the designs in Table 5.3..... 119

Chapter 6

Table 6.1 Extracted values of parasitic capacitance with different cable environments 155

Chapter 7

Table 7.1 Designs of the cable presented in this thesis..... 173

Abbreviations

B_0	External Magnetic Field Produced by MRI Machine
B_1	Radio Frequency Produced by MRI Machine to Excite Protons
BEM	Boundary Element Method
CCA	Cholangiocarcinoma
CEM	Computational Electromagnetics
CPW	Coplanar Waveguide
CRLH	Composite right-/left handed
CST MWS	Computer Simulation Technology Microwave Studio
CT	Computed Tomography
DC	Direct Current
EM	Electromagnetic
ERCP	Endoscopic Retrograde Cholangiopancreatography
FID	Free Induction Decay
FIT	Finite Integration Technique
FOV	Field of View
LH	Left-Handed Materials
MI	Magneto-Inductive
MoM	Method of Moments

MR	Magnetic Resonance
MRCP	Magnetic Resonance Cholangiopancreatography
MRI	Magnetic Resonance Imaging
MWO	Microwave Office
NMR	Nuclear Magnetic Resonance
NRI	Negative Refraction Index
PEC	Perfect Electric Conductor
PET	Positron Emission Tomography
PBG	Photonic Bandgap
PC	Photonic Crystal
PCB	Printed Circuit Board
PI	Polyimide
PTC	Percutaneous Transhepatic Cholangiography
Q-factor	Quality Factor
RF	Radio Frequency
RH	Right-Handed Materials
SAR	Specific Absorption Rate
SNR	Signal-to-Noise Ratio
T_1	Spin-spin relaxation
T_2	Spin-lattice relaxation

1. THESIS OVERVIEW

This thesis presents the development of a catheter-based thin film radiofrequency (RF) detector system designed for use in internal magnetic resonance imaging (MRI). The detector is targeted at early diagnosis of an extremely dangerous cancer of the bile duct known as cholangiocarcinoma (CCA), which although rare in the West is epidemic in the Far East. Early detection requires high resolution imaging of very small (< 2 mm) tumours, which in turn requires very high signal-to-noise ratio (*SNR*). The use of internal detection coils is likely to provide much better *SNR* than previous non-invasive magnetic resonance imaging methods based on external detection coils. However, the detector is designed for delivery by a non-magnetic duodenoscope, a procedure that is potentially much less invasive than previous surgical approaches to internal imaging.

The detector system consists of a flexible planar RF coil combined with a compatible transmission line. It is fabricated using copper-clad polyimide (PI) or Kapton, which has a high chemical resistance, a high tensile strength, and a high thermal stability. Several different electrical structures such as single-turn LC resonators, multi-turn LC resonators, microstrip lines, coplanar waveguides (CPW), photonic-bandgap (PBG) and magneto-inductive (MI) waveguides are investigated as candidate detectors and transmission lines for the system. All the components are wrapped over the catheter, and held in place with heat shrink tubing. The design task is to ensure that the system has the correct electrical performance, namely the required operating frequency (approximately 63.8 MHz for ^{1}H MRI in a 1.5 T magnetic field), characteristic impedance (50 Ω), but also has the mechanical flexibility to bend through 90 degrees to enter to the biliary ductal system on exit from the duodenoscope. To carry out the design, commercial electromagnetic simulation software (AWR Microwave Office 2009 or MWO) is used to model all the important electrical features. Theoretical models are then developed and experiments are carried out to verify that the system can perform to the required specifications.

The thesis is divided into six sections. Chapter 2 introduces the disease of cholangiocarcinoma and summarises the clinical problem. Existing medical imaging techniques for detecting CCA such as endoscopic retrograde cholangiopancreatography (ERCP) and magnetic resonance cholangiopancreatography (MRCP) are also described, together with the surgical internal imaging procedure known as intrabiliary MRI. Chapter 3 presents a literature review of earlier work on micro coils, and a basic analysis of periodic transmission lines.

Chapter 4 describes a first generation catheter based RF receiver based on a combination of a flexible microcoil (for signal detection) and a periodically structured thin-film cable (for signal transmission). It is shown that the use of periodic structuring allows the cable impedance to be matched to that of the overall MRI system (typically 50 Ω), despite the use of a thin-film structure. The detector coil and cables are then simulated using MWO, and the simulation results are compared to analytic theory and experimental data. However, safety issues associated with heating in a continuous cable are highlighted.

Chapter 5 describes a second generation of safe magneto-inductive cable, intended to minimise RF-induced heating. A brief of history of RF heating is presented, and the potential for magneto-inductive waveguides as MR-safe cables is highlighted. It is shown that a structure consisting of a self-terminating magneto-inductive waveguide can provide both a resonant detector and an output cable, using a simple thin-film layout. The overall system is then also simulated using MWO, and the simulation results are compared to analytic theory and experimental data.

Chapter 6 confirms the predictions of the previous chapter, namely that RF-induced heating is reduced using the new design of MI cable. The experimental results are presented to verify the theoretical data. Chapter 7 summarises the conclusions of the simulation data, and shows the feasibility of using a periodic interconnect in the real medical application. Proposals for future designs are then made.

Furthermore, through out this thesis, numbers in parentheses ( ) refer to equations, numbers in brackets [ ] refer to citations. For the details of each equation, an $Italic$ font is used to represent scalar quantities, a $\boldsymbol{Bold\ Italic}$ font represents matrices, $\overrightarrow{arrow}$ notation represents vectors, and $\widetilde{Tilde}$ represents unit vectors.

2. BACKGROUND, MOTIVATION, AND OBJECTIVE

Although the biliary system and related organs such as the liver, the gall bladder, and the pancreas are not as important as the heart or the brain, they are still essential for life. Consequently, hepatic and biliary disease are serious problems, since the biliary system and related organs are responsible for many important functions such as removing toxins from blood, and creating bile and digestive enzymes. The biliary system or biliary tree is a crucial path connecting all related organs, and carrying these essential fluids to the duodenum. Blockage of the biliary tree by strictures such as tumours or gall stones can cause severe pain or lead to problems such as jaundice that require rapid intervention. In this chapter, the shape, function, and anatomy of the biliary tree are described. This description is needed to clarify the problem domain, the clinical specification, and the limitations of intrabiliary MRI. Life-threatening bile duct tumours (cholangiocarcinoma), present and future feasible diagnostic technologies, as well as the motivation and research objective, are then discussed.

2.1 Anatomy of Liver and Ductal System Biliary

The biliary tree and nearby related organs are shown in Figure 2.1. The largest and the arguably most complicated organ inside the body that can be seen is the liver. It is located on the right upper of the abdomen, and it is responsible for a hundred functions as a chemical factory in the human body. The most interesting function relevant to this research is the creation of a yellowish-brown or greenish coloured fluid known as ‘bile’. Bile is produced in the liver and is transferred from the right and left hepatic duct to the common hepatic duct, and then stored in the gallbladder, a pear-shaped vessel below the liver. Another enzyme factory, the pancreas, produces pancreatic juices which consist of two important enzymes, amylase and lipase. These enzymes are a composition of digestive acid, which are mixed and transferred to the first part of the small intestine called the duodenum. Because of these important functions, hepatic disease is a major cause of death in humans today. Any

blockages in the biliary tree such as bile duct tumours or gallstones can cause serious problems of the process of digestion.

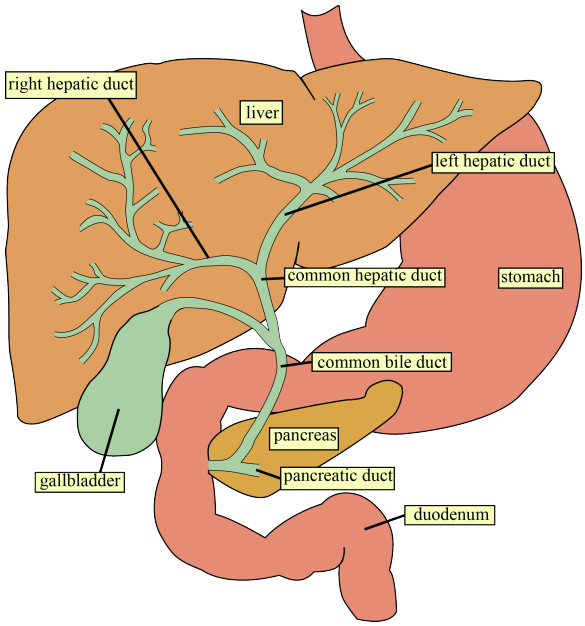


Figure 2.1 The anatomy of the biliary system and related organs

2.2 Cholangiocarcinoma

Cholangiocarcinoma (CCA) is a severe tumour in the bile tract, which is extremely difficult to detect at a curable stage. Its possible locations can be divided into three main areas shown in Figure 2.2 (A): intrahepatic, hilar, and extrahepatic [1]. The intrahepatic position represents the furthest part of the left and right hepatic duct, close to the liver before the joint of the common bile duct. The hilar position is between the common bile duct and the cystic duct. The extrahepatic position is located in the shallowest duct connecting directly to the duodenum.

In addition, according to the Bismuth classification, CCA can be separated into four types, which are identified by the location of the tumours, as shown in Figure 2.2 (B). Type I tumors occur below the joint of the left and the right hepatic duct, before the common bile duct. Type II tumours appear at the beginning of the left and right hepatic duct. Type IIIa and

IIIb tumours are located in deeper parts of the left or right hepatic duct. Type IV tumours are found at bifurcations of the hepatic duct, where the two branches connect together, in the confluence of the hilar or the extrahepatic position. Treatment will depend on knowing the precise location of the tumour [2]. 60-70% of CCA appear at the bifurcation of the hepatic duct. The other types of CCA occur in the common bile duct (20-30%), and inside the liver (5-15%) [3]. Thus, the precise location of the tumours is needed.

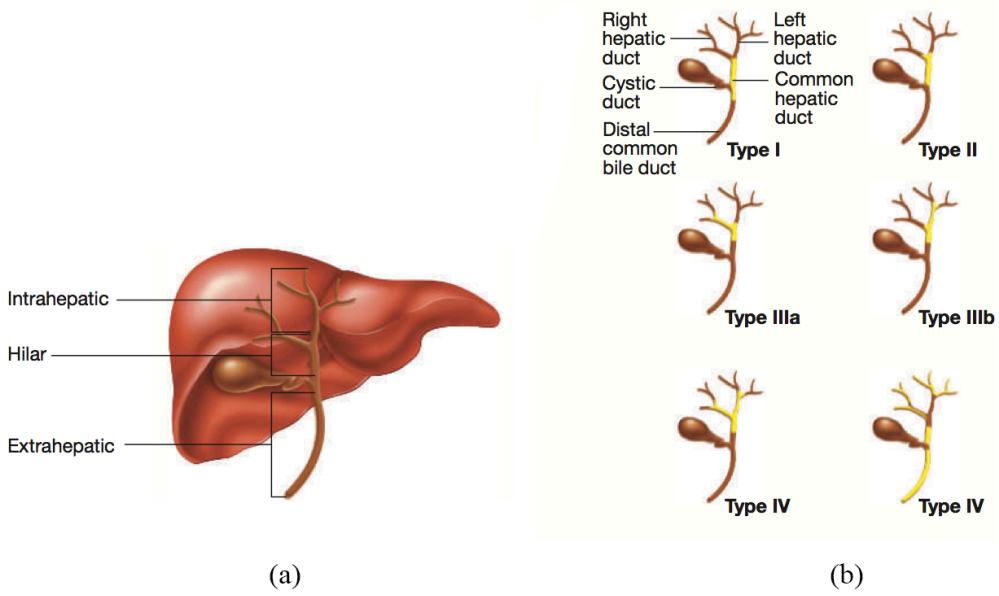


Figure 2.2 (a) Three main regions of the biliary tract; (b) four types of CCA according to the Bismuth classification [1]

CCA is a serious problem in Thailand and the Laos People's Democratic Republic, because of the widespread consumption of traditional, inadequately cooked fish dishes such as Koi Pla. These dishes are typically based on cyprinoid (carp-type) fish, which are infested with liver fluke (*Opisthorchis viverrini*, OV) [2, 4, 5]. The liver fluke migrate into the bile duct, where they cause liver fluke disease, which has CCA as a possible end-stage. At present, there are no reliable blood tests or serum tumour markers for CCA. The symptoms of CCA commonly present after only the disease has reached an untreatable stage, so most of patients are unaware of their condition until jaundice, pale stool or dark urine appear. As a result, many cases are inoperable, and less than 5 percent of diagnosed patients survive to 5 years.

Figure 2.3 shows the incidence rate per 100,000 in Thailand by province, demonstrating the epidemic nature of the disease. The incidence of CCA is much lower in developed countries such as England and Wales, but has almost doubled during 1979-1996, possibly due to increased consumption of alcohol [6], which has been associated with a mutation of alleles of the cystic fibrosis trans-membrane conductance regulator (CFTR) gene due to the presence of chemical toxins in alcohol.

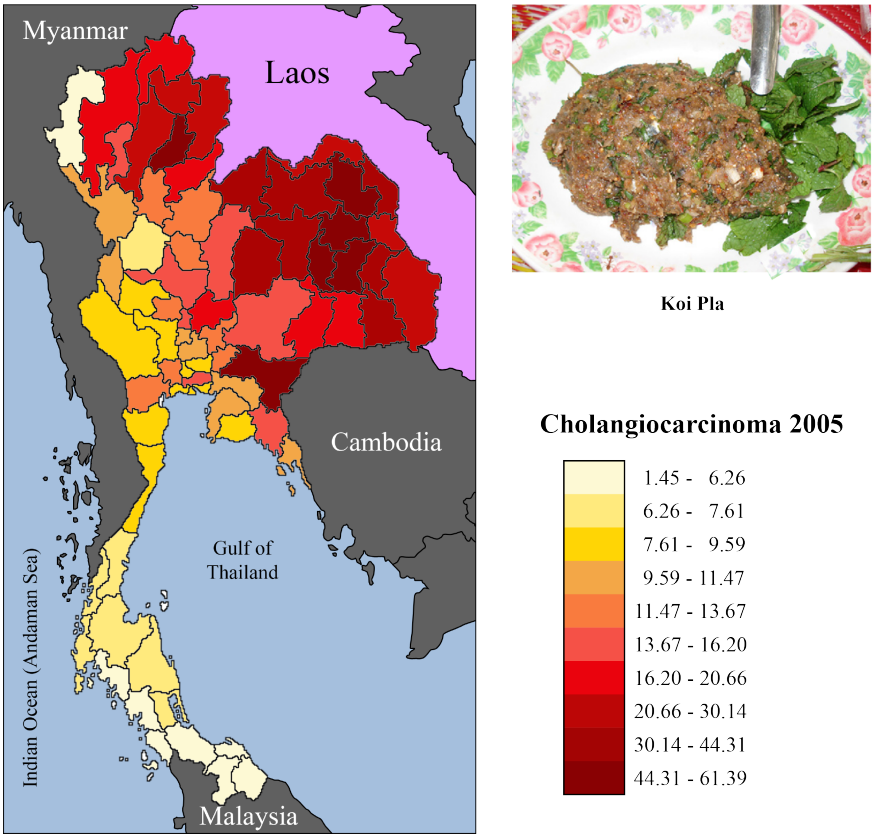


Figure 2.3 The incidence of Cholangiocarcinoma by province in Thailand [5]

Many imaging procedures are used to determine the development of more advanced CCA, a procedure known as staging. These include endoscopic retrograde cholangiopancreatography (ERCP), percutaneous transhepatic cholangiography (PTC), positron emission tomography (PET), computed tomography (CT), ultrasonic imaging (UI), magnetic resonance cholangiopancreatography (MRCP), and intrabiliary MRI. In this report, only ERCP, MRCP, and intrabiliary MRI, will be discussed, because these are the most common imaging modalities.

2.3 Endoscopic Retrograde Cholangiopancreatography (ERCP)

ERCP is a clinical procedure used for detecting strictures or tumours in the biliary system such as gallstones and cholangiocarcinoma, based on a combination of endoscopy and X-ray fluoroscopy, and uses an endoscope as a navigating device as shown in Figure 2.4 and a dye for radiocontrast. To carry out ERCP, patients first have their throat numbed using an anaesthetic spray. They will also usually be given a sedative by injection into a vein. These make them relaxed and drowsy, without falling asleep, so that a flexible, side-viewing duodenoscope (a modified gastroscope with an internal channel known as an accessory or biopsy channel) can be passed down their throat and through the stomach until it reaches the duodenum. During the process, the duodenoscope is controlled by a clinician using manual steering wheels, while observing through an eyepiece or on a TV monitor until the ampulla of Vater (the opening of the bile duct into the duodenum) is located.

A catheter is then passed through the biopsy channel and out of one side of the instrument, and inserted through the ampulla into the bile duct under the control of a steerable deflector. This procedure is known as cannulation. Because cannulation has a high failure rate, a metal guidewire is often used. This allows rapid interchange of catheter tools without having to repeat the same lengthy procedure. The catheter is then used to inject a radioopaque dye into the duct, which swells the duct and delineates its outline. X-ray fluoroscopy images are then taken, and constrictions in the duct are typically indicative of CCA. In this case, small samples of ductal tissue (a biopsy) are taken to check for abnormal cells in the histology laboratory. The sampling is carried out using a special tool inserted through the biopsy channel known as a cytology brush.

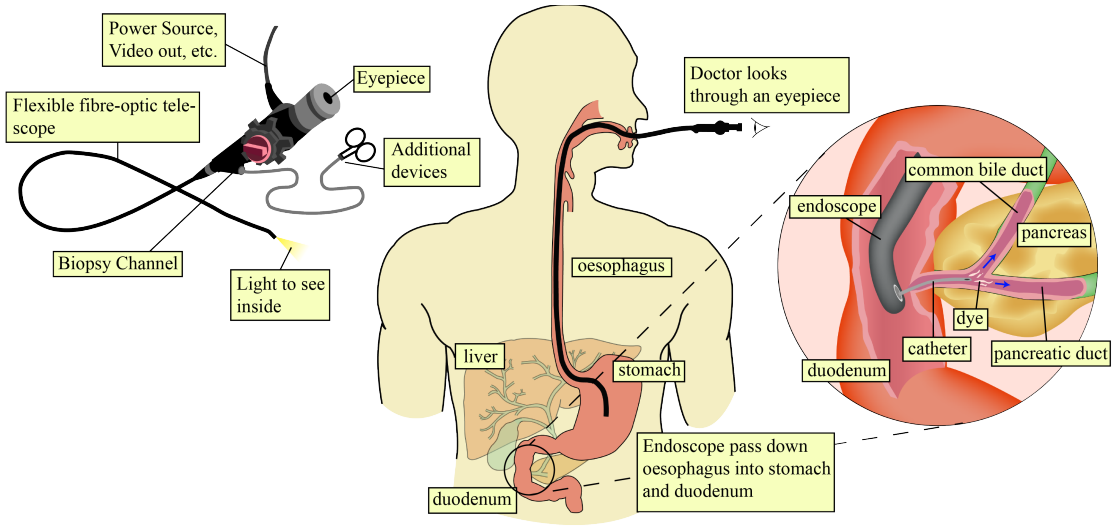


Figure 2.4 Endoscope used in ERCP, and location of the endoscope during the procedure [7]

Although this technique can reveal many details of the ductal boundaries, other soft tissues and details such as CCA are barely visible. Figure 2.5 shows a typical X-ray fluoroscopy image, in which only the duodenoscope, skeletal structure, gallstones and the radioopaque dye may be clearly seen. Moreover, because the procedure relies on ionizing radiation, and the overall X-ray dose must be limited, it is an invasive and generally unsafe technique. In addition, the dye may fail to drain properly, resulting in serious complications. As a result, there is considerable interest in safer methods, such as MRI.

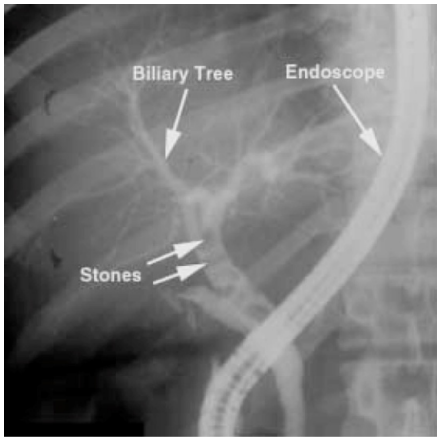


Figure 2.5 X-ray fluoroscopy image obtained during ERCP [8]

2.4 Magnetic Resonance Imaging

MRI is a non-invasive medical imaging method which has an enormous impact on the medical profession, providing a step change in diagnostic ability for many disease types involving soft tissue. It is based on fundamental magnetic properties of nuclei (specifically, nuclei of the hydrogen atom, the proton or ^{1}H). Due to its spin, a proton behaves as a tiny bar magnet or dipole. In a quantum mechanical description, the properties of a single dipole are specified in terms of the relationship between the spin and magnetic moment (or the precession motion of proton) [9, 10] as shown in Equation (2.1).

$$\vec{\mu} = \gamma \vec{J} = \gamma m \hbar \tag{2.1}$$

Here $\vec{\mu}$ is the magnetic moment vector, γ is the gyromagnetic ratio (a scalar constant of proportionality , whose value is close to the charge-to-mass ratio), $\vec{J}$ is the spin angular momentum vector, m is the magnetic quantum number, and ħ is the reduced Planck constant or Dirac constant ($\hbar = \frac{h}{2\pi}$ where h is the Planck constant).

Under normal circumstances, the protons randomly spin without adopting any particular alignment, as shown in Figure 2.6.

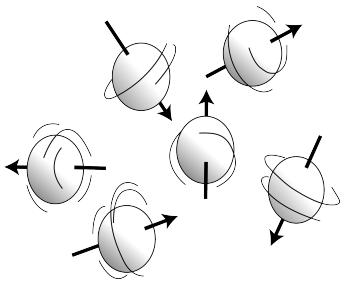


Figure 2.6 Non-aligned protons forming a random distribution of magnetic dipoles [11]

However, during MRI, tissue containing protons is placed in a strong external magnetic field, whose strength is of the order of a Tesla (1 Tesla = 10,000 Gauss). Under these circumstances, the protons will tend to align themselves to the external field. The energy of a magnetic dipole in a magnetic field is:

$$E = \vec{\mu} \cdot \vec{B}_0 \tag{2.2}$$

Here E represents energy, and $\vec{B}_0 = B_0 \cdot \tilde{z}$ is the external magnetic field, which is assumed to lie in the Z-direction. If Equation (2.1) is substituted into Equation (2.2), we obtain:

$$E = \gamma m \hbar B_0 \tag{2.3}$$

Now, the proton has two possible spin states, with $m = {}^{1}/_{2}$ and $= -{}^{1}/_{2}$, respectively, refered to as the spin-up and spin-down states. From Equation (2.3), the energy of these two states are:

$$E_{+1/2} = -\gamma \hbar B_0/2 \tag{2.4}$$

$$E_{-1/2} = \gamma \hbar B_0/2 \tag{2.5}$$

Here $E_{+1/2}$ is the energy of a proton in the parallel state (low energy state or spin-up), and $E_{-1/2}$ is the energy of a proton in the anti-parallel state (high energy state or spin-down), as shown in Figure 2.7.

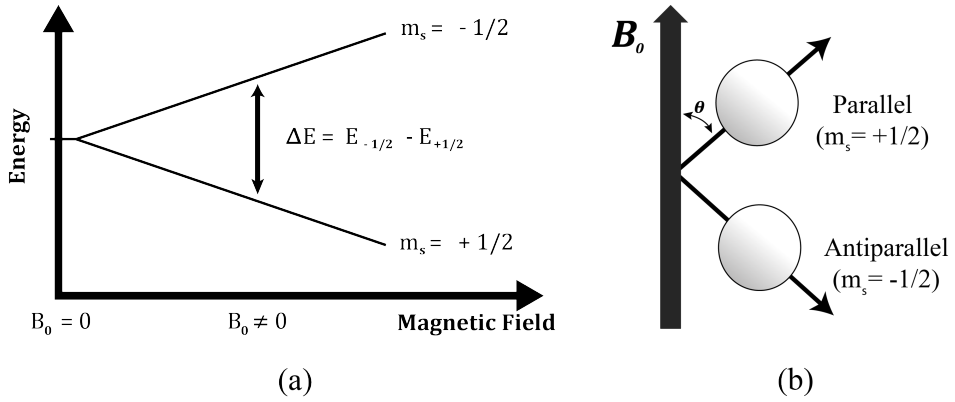


Figure 2.7 (a) The energy levels of a spin ½ system [9, 10] (b) The two orientations of a spinning proton aligned by an external magnetic field B_0 [11]

Clearly, the energy difference between the two proton spin states is given by:

$$\Delta E = \hbar\omega = \gamma\hbar B_0 \tag{2.6}$$

If an equivalent amount of energy is available in the form of an electromagnetic photon of angular frequency $\omega = 2\pi f$, the alignment of the spin may be altered, absorbing the photon in the process. The angular frequency required is clearly:

$$\omega = \gamma B_0 \tag{2.7}$$

The angular frequency is known as the Larmor frequency, and Equation (2.7) is known as the precessional equation, since non-aligned spins will rotate or precess about the B_0 axis at this frequency.

As described before, MRI mainly takes advantages of the natural properties of the hydrogen atom (for which γ = 267.513 MH_zT^{-1}) because water is the main component found in the

body (75-80%). At 1.5 Tesla (the field strength of standard clinical scanners used for human MRI) the frequency may then be found as [12]:

$$Frequency \approx \frac{267.513\ \mathrm{MH_z T^{-1}} \times 1.5\ \mathrm{T}}{2\pi} \approx 63.84\ \mathrm{MH_z} \tag{2.8}$$

Clearly, this frequency lies in the RF band, and a powerful RF transmitter operating at this frequency may therefore be used to alter the spin state.

More generally, tissue will contain an ensemble of spins rather than a single spin. In this case, the system may more conveniently be described in terms of the net magnetization or macroscopic magnetization ($\vec{M}$), defined as the sum of the quantum mechanical expectation of the microscopic magnetization ($\vec{\mu}$) per unit volume (V) of the sample as shown below.

$$\vec{M} = \frac{1}{V}\sum_i \langle \vec{\mu}_i \rangle \tag{2.9}$$

The correspondence principle in Physics states that a large amount of quantum calculations must agree with the classical mechanical calculations, allowing classical mechanics to be used to explain the interaction of thee $\vec{M}$ vector and the static magnetic field (B_0) and the RF pulse (B_1). The $\vec{M}$ vector from Equation (2.**9**) is almost unobservable, but has a small longitudinal component aligned with the B_0 field due to a slight excess of parallel state spins (the low energy state), which can be increased using a larger B_0.

More generally, the net magnetization vector of the spinning protons can be divided into two orthogonal components; a longitudinal component ($\vec{M}_z$) and a transverse component ($\vec{M}_{xy}$) in Cartesian coordinates as shown in Figure 2.8.

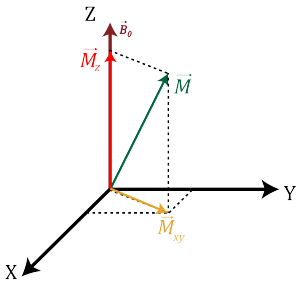


Figure 2.8 Division of magnetic moment into longitudinal ($\vec{M}_z$) and transverse ($\vec{M}_{xy}$) components

In the equilibrium state, the magnetization vector will be aligned with the B_0 field, so that $\vec{M}_z$ has a finite value M_0 and $\vec{M}_{xy}$ is zero as shown in Figure 2.9a below. If a B_1 field is applied in the x-direction, the nuclei will absorb energy. As a result, their net magnetizations will alter as shown in Figure 2.9. The magnetization vector will start to precess about the B_0 axis at the Larmor frequency, and gradually rotate away from this axis through an angle known as the flip angle (α). In the process, the transverse magnetization will increase, so that $\vec{M}_{xy} = M_0 \cdot |sin\, 0|$. This step in MRI is called 'Excitation'.

When a suitable flip angle (often 90^o, the point at which the transverse magnetization is maximum) has been reached, the RF transmitter is turned off. The protons then gradually return themselves to the equilibrium state, with the magnetization vector spiralling back towards the B_0 axis as shown in Figure 2.9c. This step is called 'Relaxation'. In the process, they emit radiation at the Larmor frequency. Therefore, there is an exchange of energy at the specific frequency between the spins and electromagnetic radiation, known as 'magnetic resonance'.

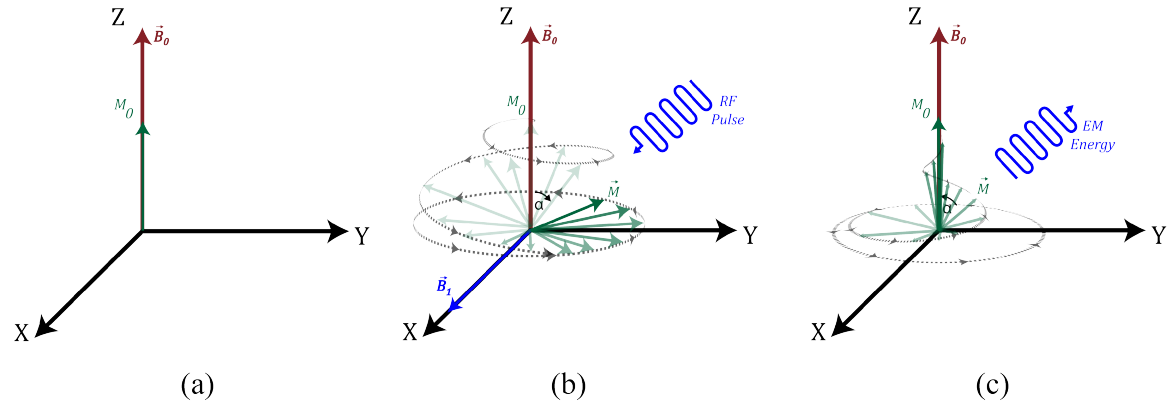
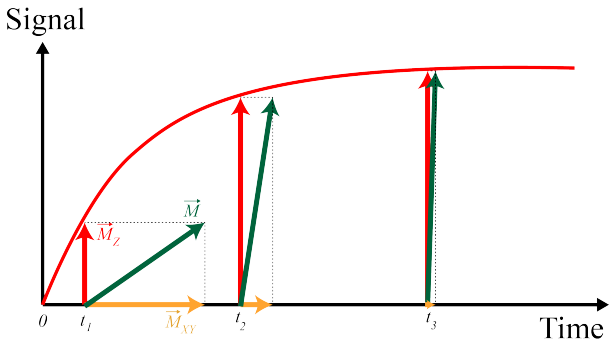


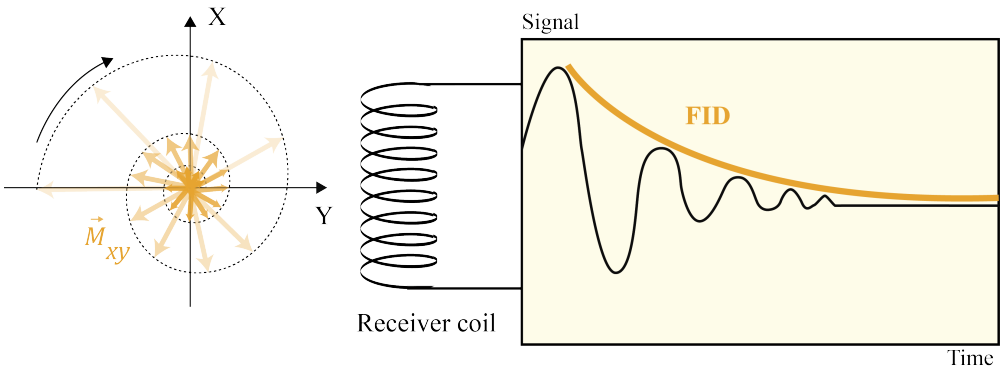
Figure 2.9 The NET magnetization when (a) before RF pulse (b) during the excitation (c) during the relaxation

There are two different relaxation mechanisms. Spin-lattice or longitudinal relaxation (characterized by a time constant T_1) and spin-spin or transverse relaxation (which has a different time constant T_2), account for the recovery of the longitudinal magnetization ($\vec{M}_z$) and the decay of the transverse magnetization ($\vec{M}_{xy}$), respectively.

In T_1 relaxation, when the RF transmitter is turned off, there is a gradual energy exchange between the relaxing spins and nearby molecules (or a lattice), which causes the vector $\vec{M}_z$ to return to its equilibrium value M_0 exponentially as shown in Figure 2.10a. At the same time in T_2 relaxation, the rotating vector $\vec{M}_{xy}$ rapidly decays away after excitation and can induce an electromagnetic force (EMF) in a tuned resonant circuit at the Lamor frequency. The signal detected by a RF receiver coil following Faraday's law of induction from the decreasing movement of vector $\vec{M}_{xy}$ is called Free Induction Decay (FID) as shown in Figure 2.10b.



(a)



(b)

Figure 2.10 Relaxations (a) T_1 (b) T_2 recorded by a RF receiver coil

During free induction decay, the decay of the different components of the magnetization $\vec{M}$ is described by Bloch equations:

$$\frac{dM_z}{dt} = \frac{M_0 - M_z}{T_1} \tag{2.10}$$

$$\frac{dM_x}{dt} = \omega_0 M_y - \frac{M_x}{T_2} \tag{2.11}$$

$$\frac{dM_y}{dt} = -\omega_0 M_x - \frac{M_y}{T_2} \tag{2.12}$$

These equations may be solved in detail for given values of T_1 and T_2. As it turns out, different tissue types have different values of T_1 and T_2. These properties are exploited to create a tissue contrast image by choosing complex RF pulse sequences to create MRI signals that are either T_1 or T_2 weighted, and hence provide a contrast that is optimised for a particular tissue type.

The process above does not localise the received signal to a region of space. A number of sophisticated additional techniques are therefore required to obtain an image. Two main aspects are involved. Firstly, the region of tissue responding to the RF pulse is reduced by locally varying the B_0 field using additional gradient coils; a slice selection gradient (G_{SS}), a phase encoding gradient (G_{PE}), and a frequency encoding gradient (G_{FE}) which have MR sequences as shown in Figure 2.11. A magnetic field gradient, G_{SS} is used to select a certain region of interest, which is applied simultaneously with an RF pulse at the Larmor frequency. G_{PE} is used for vertical spatial encoding, which modifies the spin resonance frequencies inducing dephasing represented in information rows or x-axis. G_{FE} modifies the Larmor frequency horizontally creating spatial information columns or y-direction. Two further parameters, the echo time (TE) and repetition time (TR), are used to vary types of MR images such as T1-, T2- or PD-weighted images. TE is the time between 90 degree RF and MR signal sampling, and TR is the time between the application of one RF excitation and the next.

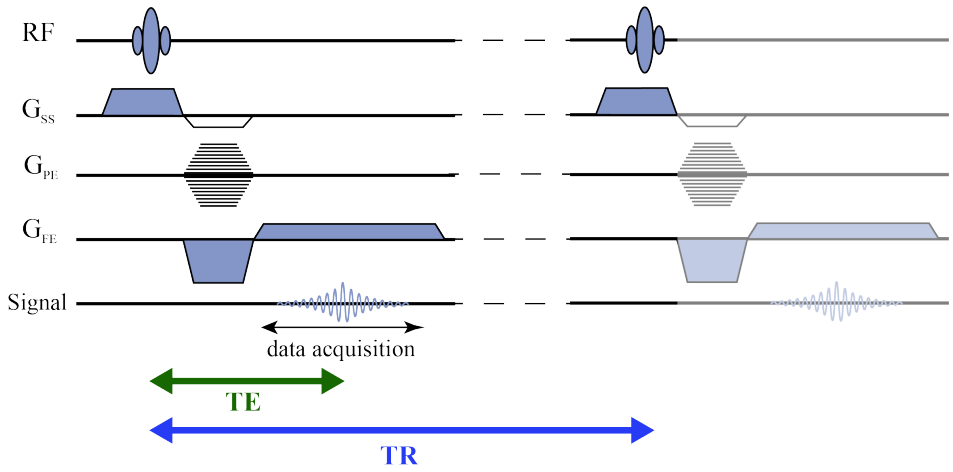


Figure 2.11 Basic gradient echo MR imaging sequences [12]

All readout signals from the selected slice are a mix of RF waves with different amplitudes, frequencies, and phases, containing spatial information recorded in a data matrix called k-space as shown in Figure 2.12. The second aspect is a Fourier transform relation, which is used to convert information obtained k-space into an MR image. The resolution of the image or the field of view (FOV) has a direct relationship with k-space. So, to increase the image resolution, there are three possibilities; increase the gradient strength, increase the size of the matrix, or increase the sampling time.

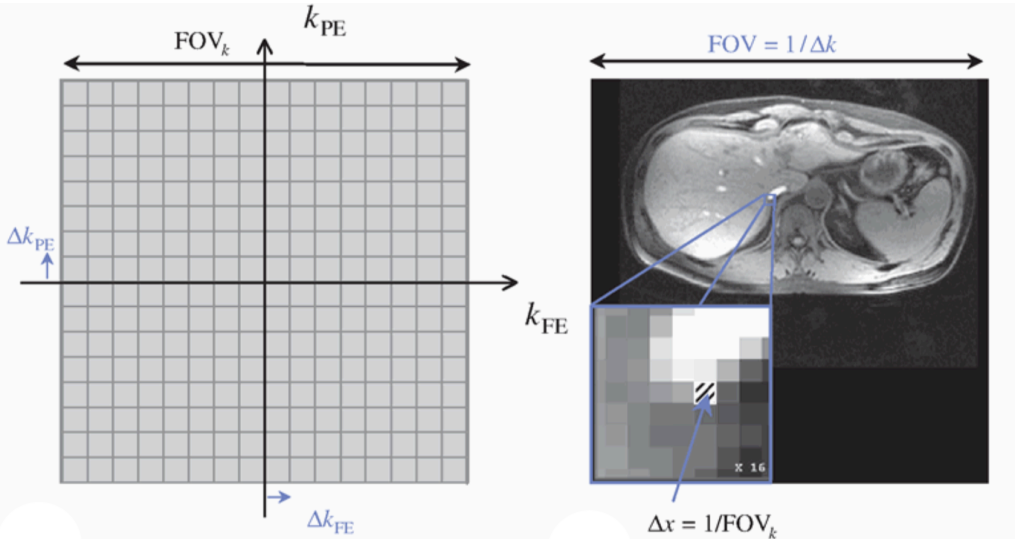


Figure 2.12 K-space used to convert a signal into an MR image [12]

The components of an MRI scanner are shown in Figure 2.13. The main magnet is generally a superconducting electromagnet, which provides a strong and homogenous magnetic field B_0 between 0.2 and 9.0 T. The gradient coils produce a linearly varying magnetic field that defines the slice thickness. There are three well known planes used in MRI imaging; transverse, coronal, and sagittal planes for axial, frontal, and vertical selections. The radio frequency system comprises a transmitter coil designed to produce a B_1 field and a receiver coil to detect the MR signal.

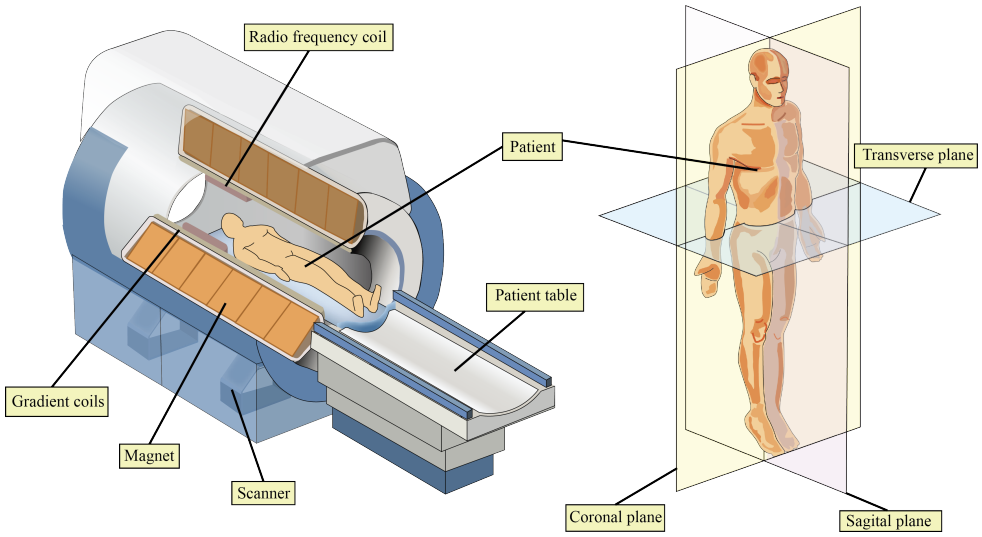


Figure 2.13 Cutaway image of a conventional MRI scanner [13]

The quality of images can be measured by the signal-to-noise ratio (*SNR*). Using elementary theory, the achievable *SNR* $\boldsymbol{Y_{rms}}$ may be estimated [14]. The original theory referred to a solenoid coil; however, by replacing coil-specific quantities such as the number of turns and their arrangement by generic quantities such as the coil volume the analysis may easily be adapted to other types of coil. The result is:

$$\Psi_{rms} = K\eta M_0(\mu_0 Q \omega_0 V_c/4FkT_c\Delta B)^{1/2} \tag{2.13}$$

Where K is a numerical factor depending upon the receiving coil structure, η is the filling factor which is a measure of the fraction of the coil volume occupied by the sample, M_0 is the nuclear magnetization, μ_0 is the permeability of free space, Q is the quality factor of the coil, ω_0 is the Larmor angular frequency, V_c is the volume of the coil, F is the noise figure, k is Boltzmann's constant, T_c is the probe temperature, and ΔB is the bandwidth of the receiver. Examination of Equation (2.13) suggests three possibilities to improve *SNR*: 1) a change of geometry of the coil, 2) an increase of the filling factor by positioning a coil immediately adjacent to the sample, and 3) an improved Q-factor of the coil which can be described by equation below.

$$Q = \frac{\omega L}{R_s} \tag{2.14}$$

Where L is inductance, and R_s is series resistance that presents in the coil.

As can be seen in Equation (2.14), the Q-factor can be improved by increasing the ratio L/R_s. However, this is not simple, because the two parameters are linked. The best approach is to increase the number of turns in the coil by N, which increases R_s by N and L by N^2, and hence nominally increases Q by N. However, the maximum Q-factor of any coil is limited, when the coil is loaded because there is additional loss from the eddy currents induced inside the specimen itself and consequently the main impact comes from the filling factor.

2.5 Magnetic Resonance Cholangiopancreatography (MRCP)

MRCP is a magnetic resonance imaging technique used for viewing tissue in the biliary system, based on an external chest coil array as shown in Figure 2.14.

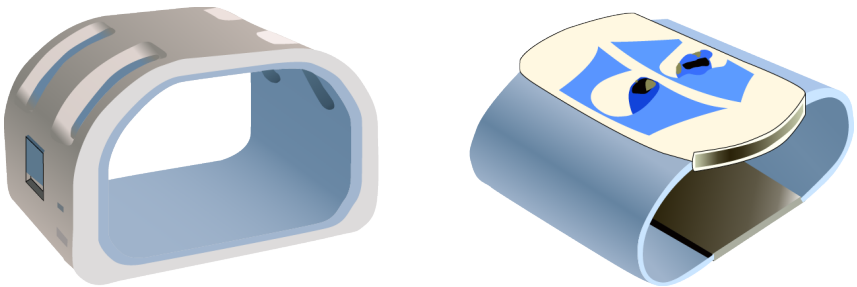


Figure 2.14 Rigid and flexible RF chest coil [15]

A recent study that compared the performance of MRCP with ERCP showed that MRCP has a similar sensitivity to ERCP, while being entirely non-invasive [16]. However, MRCP provides higher specificity than ERCP, and can be used to image soft tissue as shown in

Figure 2.15. Experimentally, Manfredi et al. have shown the potential of using MRCP to diagnose a Klatskin tumor or Hilar cholangiocarcinoma [17].

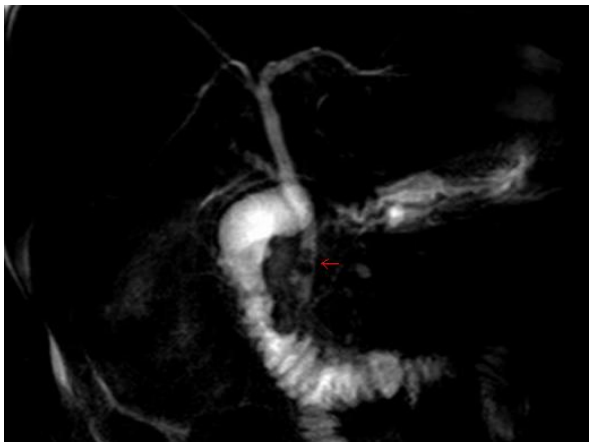


Figure 2.15 X-ray image of the biliary tree, with a red arrow showing two gallstones in the common bile duct [8]

Unfortunately, the image is unfortunately still too poor for accurate diagnosis of CCA at an early stage. This is primarily because the *SNR* is insufficient due to the poor filling factor between body coil and the sample tissue. This cannot be improved by averaging, because of the effect of breathing motion. One possible solution is intrabiliary MRI, which provides an intrinsically better signal.

2.6 Intrabiliary MRI

Intrabiliary MRI is a variant of MRCP that provides a higher *SNR*, better resolution of the soft tissue, and a more precise tumour location. It uses the same principle as MRCP, but the RF signal is now detected using a miniature coil placed adjacent to the target tissue instead of the body coil so that the small coil is completely filled by the tissue that is being examined as shown in Figure 2.16. Because CT and MRCP can offer overall accuracy for staging a

tumour location of only 60%, intrabiliary MRI is a competitive alternative for assessment of resectability.

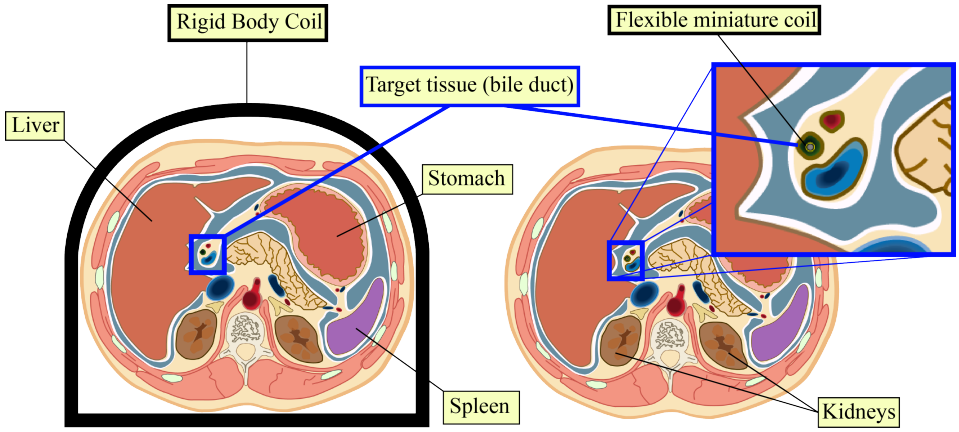


Figure 2.16 Rigid body coil versus miniature coil in a cross-section of the human body

In 2003, there was a study of hilar cholangiocarcinoma by intrabiliary MRI [18]. This study first tried locating the tumours in two patients with resectable tumours. Since there were no specific coils for intrabiliary MRI available, they used an intravascular coil instead. To carry out the procedure, the patients first required decompression (a clinical procedure used to reduce pressure in the biliary tree by draining bile) for 1-2 weeks. Biliary access was achieved using fluoroscopic visualization to guide the positioning of a guidewire. The biliary tree was first made radiopaque by dye injection using a 22-gauge needle. The right posterior duct was then punctured by a 21-gauge trocar needle. Subsequently, a dilator-sheath was then placed in the biliary duct, then a hydrophilic guidewire and finally a 10-French drainage catheter. After a recovery period (1-2 weeks), the receiver coil was inserted through the sheath into the target area, and the patients were transferred to the MRI department for imaging. Figure 2.17 below shows one of the images obtained. Later, Weiss et al. confirmed the performance of intrabiliary MRI compared with CT and cholangiography [19]. They found that intrabiliary MRI could be performed in less than 1 hour, and has higher sensitivity than CT, and higher specificity than other forms of cholangiography.

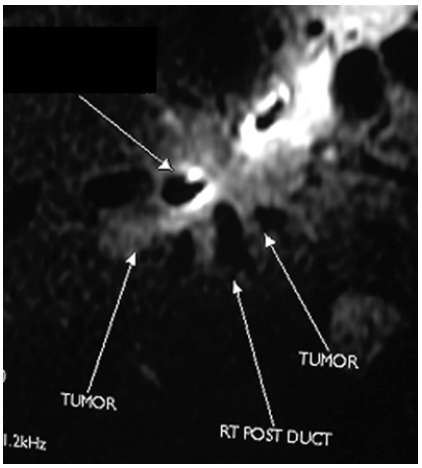


Figure 2.17 The picture of tumour and adjacent tissue by intrabiliary MRI [18]

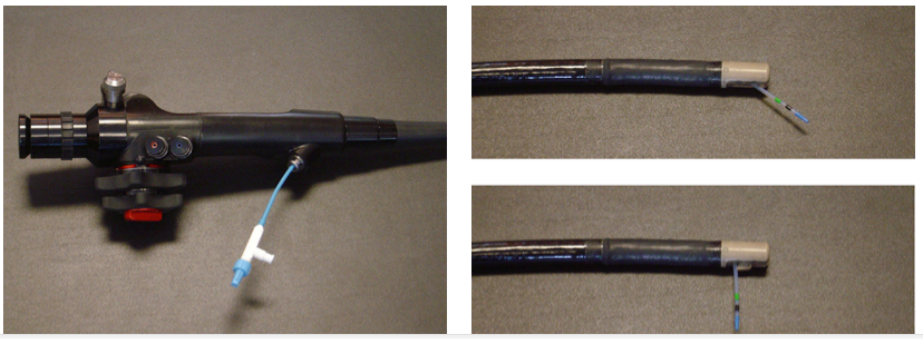
Though the clear picture of tumour was successfully obtained, intrabiliary MRI is much more invasive than either ERCP or MRCP because fluoroscopic visualization and a complex surgical operation are both required. However, this procedure highlights the potential of small internal coils.

2.7 Research Objective

To provide a non-surgical alternative to intrabiliary MRI, a collaborative project between St Mary's Hospital and the EEE Department of Imperial College London has been established. The procedure being developed uses a non-magnetic gastroscope as shown in Figure 2.18a to insert a MR imaging catheter probe directly into the bile duct, where it should again be capable of acquiring images with high *SNR*. The detailed aim of work described in this thesis is the design of a flexible RF receiver coil and transmission line that may be attached to the catheter. The resulting catheter must be capable of being passed through the biopsy channel and bend through 90 degree at the distal end as shown in Figure 2.18b. This new procedure is not only less invasive, but retains high resolution imaging. Furthermore, the components needed are very low cost and easy to manufacture. As a result, these elements can be disposed of after use, making the procedure hygienic and safe.



(a)



(b)

Figure 2.18 Nonferrous components used in this work (a) non-magnetic gastroscope (b) catheter passed through the biopsy channel and bent 90 degree at the distal end

From previous studies [18, 19], a rigid MR receiver coil and a coaxial cable were known to prevent the use of a guidewire. Hence, this work mainly focuses on design of a flexible RF coil and transmission line which can be wrapped over a catheter to leave the internal lumen free. The first part of the study, presented in Chapter 4, proposes a planar microcoil and a microstrip with periodically patterned ground cable fabricated on a polyimide (PI) substrate. The potential for tuning to the operating frequency (63.8 MHz) required by ^{1}H MRI at 1.5 T and matching to the impedance of the overall system (50 Ω) are investigated by simulating a microcoil and a patterned microstrip using electromagnetic analysis software: AWR Microwave Office (MWO). The characteristic impedance, inductance and capacitance were subsequently extracted and compared to the theoretical and experimental data. However, such a system was also known to be electrically unsafe.

The second part of the study, presented in Chapter 5, is concerned with an intrinsically safe cable based on a magneto-inductive (MI) waveguide. It again consists of a thin-film circuit, but is now based on segmented cable that is subdivided into elements to short for resonant electrical heating and twisted into figure-of-eight shapes to prevent resonant magnetic heating. Impedance matching between the cable and the scanner input is carried out using magnetically coupled transducers. AWR Microwave Office (MWO) is again used to perform a computational analysis. The safety of the cable is demonstrated via further simulations in Chapter 6, using magnetic and electrical excitation to mimic the known external fields.

3. LITERATURE REVIEW

This chapter provides background understanding of flexible coils and transmission lines, and briefly reviews related works of interventional MRI. This review is divided into two main sections. In the first section, the concept of RF coils and the development of miniature receiver coils for intravascular and intrabiliary MRI are outlined. In the second, the basic theory of periodic transmission lines for internal MRI, which will be used for analysis in later chapter, is presented.

3.1 RF Receiver Coil

As described in Chapter 2, magnetic resonance imaging involves an initial excitation phase followed by a detection phase. In the former, a radiofrequency pulse is used excite the dipole distribution present in tissue. In the latter, the imbalanced protons return to equilibrium. In the process, they emit RF energy, which can be detected by a receiver coil. An LC resonant circuit is the basis of both transmitter and receiver coils, and a receiver coil can be constructed as shown in Figure 3.1. The inductor (L) is responsible for detecting the MR signal, which induces a voltage in the coil following Faraday's law. The first capacitor (C_T) is responsible for tuning the resonant frequency of the receiver coil to the particular Larmor frequency. The second capacitor (C_M) is responsible for matching the impedance of the circuit to optimize coupling to the pre-amplifier of the MRI. R is a resistance that represents the sum of the coil resistance and the load due to the signal source (the tissue).

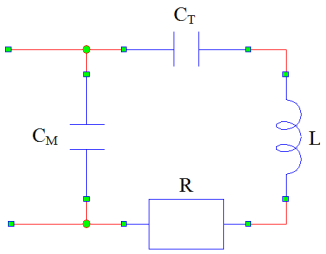


Figure 3.1 The receiver coil equivalent circuit

From Figure 3.1, the first electrical feature that we interest is the impedance for the whole circuit, which can be found as:

$$Z_{in} = \frac{\frac{1}{j\omega C_M}\left(\frac{1}{j\omega C_T} + R + j\omega L\right)}{\left\{\left(\frac{1}{j\omega C_T} + j\omega L\right) + \frac{1}{j\omega C_M}\right\} + R} \tag{3.1}$$

As can be seen from Equation (3.**1**), resonance is obtained when the reactances in the denominator cancel, so that the denominator becomes very small and large currents can flow. The resonance condition of the coil is therefore found from:

$$\frac{1}{j\omega C_T} + \frac{1}{j\omega C_M} + j\omega L = 0 \tag{3.2}$$

From Equation (3.2), it is clear a receiver coil of given inductance can be tuned by adjusting the value of the two capacitors C_T and C_M. Since the latter is typically much larger, the main effect is obtained by altering C_T. In this case, resonance is obtained when $C_T = \frac{1}{\omega^2 L}$.

Matching to the scanner input impedance is then mainly achieved by altering the value of C_M. If the circuit is resonant, Equation (3.**1**) can be written as $Z_{in} = (1/j\omega C_M)\{R - 1/j\omega C_M\}/R$. If in addition, $R \ll \frac{1}{\omega C_M}$ (which is often the case for a low loss coil) we may approximate this result as:

$$Z_{in} = \frac{1}{\omega^2 C_M^2 R} \tag{3.3}$$

Under these circumstances, Z_{in} is real and can be matched to a given load R_L by choosing $C_M = 1/\{\omega(RR_L)^{1/2}\}$.

For example, a thin-film RF receiver coil described in a later chapter has the electrical parameters L = 421 nH and R = 0.1 Ω. To achieve a resonance frequency of 63.85 MHz. we require $C_T = 1/\{(2\pi\times 63.85\times 10^6)^2\times 421\times 10^{-9}\} = 14.75$ pF. Similarly, for matching to a system impedance of 50 Ω, we require $C_M = 1/\left\{2\times\pi\times 63.85\times 10^6\times(0.1\times 50)^{\frac{1}{2}}\right\} = 1114$ pF. A more accurate calculation, omitting some of the approximations above, gives C_T = 15.50 pF, C_M = 316.09 pF. Using these data, the real and imaginary part of impedance can be plotted using Matlab following Equation (3.**1**) as shown in Figure 3.2. As can be seen, resonance is obtained at 63.83 MHz, and the impedance is 50 Ω at this point.

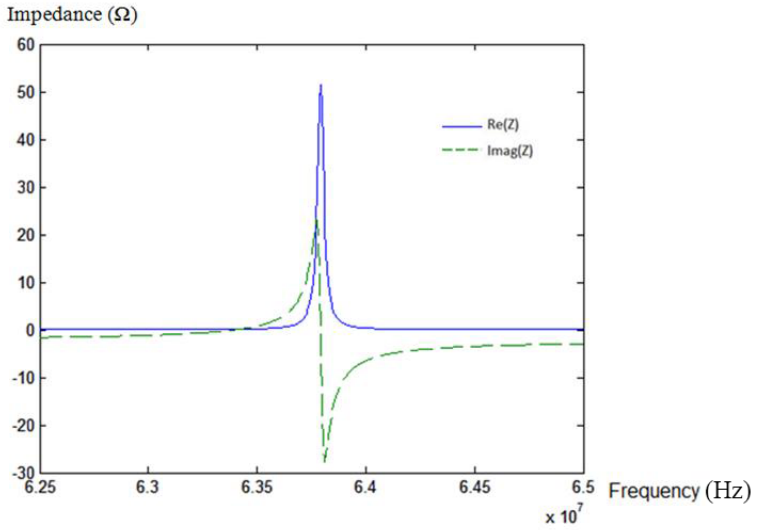


Figure 3.2 Frequency variation of impedance found from Equation (3.1), for the parameters of a typical experimental microcoil

In practice, the tuned and matched receiver coil may couple directly to the transmitter coil during RF excitation. The large induced currents might lead to serious local heating, or the creation of an image artefact. To avoid this problem, a decoupling mechanism is used. There are several alternative methods for decoupling, for example, inserting either capacitors or inductors between the two coils to cancel the mutual inductance between them [20]. The most common solution uses a PIN diode with an additional inductor (L_D) as shown in Figure 3.3 below. If a DC bias current is applied across the PIN diode during RF excitation, then the PIN diode acts as short circuit. In this case, a tank filter is can be inserted into the tuned circuit, to block large signals at the excitation frequency.

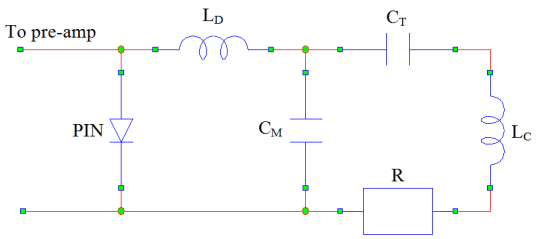


Figure 3.3 L-C resonator used for signal reception with additional PIN diode-switched tank filter to decouple the resonator from the transmitter

3.2 Development of RF Coils for Internal MRI

Prior to intrabiliary MRI (an internal MRI procedure used for imaging the hepatic duct, which requires surgery), RF receiver coils were mainly used for investigation of atherosclerotic diseases in the aorta, the coronary arteries, and the renal arteries. In this section, the history of the development of intravascular coils is presented. Detecting and generating an image of blood vessels was not the only important purpose in the development, but also reducing the coils' size to suit vascular walls. In 1992, Hurst et al. showed the feasibility of using a NMR receiver probe for imaging canine arterial walls [21]. They used an opposed solenoid coil, formed by a winding copper wire on cylindrical polyethylene tubing as shown in Figure 3.4 because it offers more homogeneity than the other designs. However, a size problem was found, and they could not miniaturize the coil to suit even large blood vessels such as the aorta. Coil size can be reduced only by decreasing the inductance, which requires a larger capacitance to operate at the same frequency.

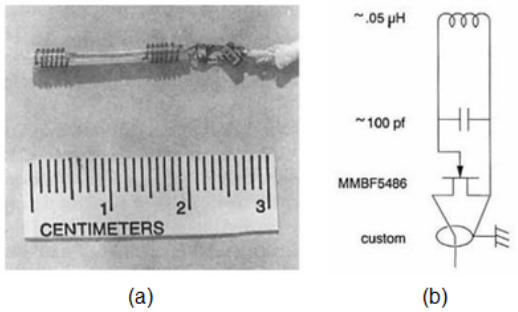


Figure 3.4 (a) Opposed solenoid coil, (b) and equivalent circuit [21]

Atalar et al. then developed another coil design, which is longer, narrower, and more flexible than the solenoid coil above [22]. The coil used two parallel conductors with short-circuited ends as an inductor, with a plastic insulator (vinyl) as a dielectric between as shown in Figure 3.5. Several models were created, with lengths between 6-8 centimetres, and with 1.5 mm diameter. High signal-to-ratio (*SNR*) was successfully obtained during imaging of a rabbit aorta. However, because of the large length of the coil, the design is not well-suited to small vessels with many internal bends.

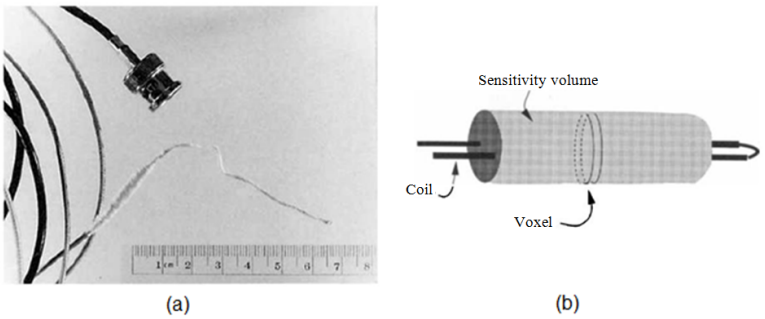


Figure 3.5 (a) Photograph of parallel conductor coil (b) 3D model of coil construction [22]

A related design by Ocali and Atalar is the so-called 'loopless' catheter antenna [23]. The catheter antenna is composed of a dipole antenna at the distal end of a coaxial cable as shown in Figure 3.6. This design can solve the limitations in physical dimension; however, the resistance is noticeably large when compared to other catheter coils. This problem can be solved using a tuning-matching-decoupling circuit far from the antenna. Using this coil, an in vivo image of a rabbit aorta was obtained, with improved *SNR* compared to the parallel-conductor coil. Although this coil was designed for intravascular use, it was also used in intrabiliary MRI application as previously shown in section 2.7 [17, 18].

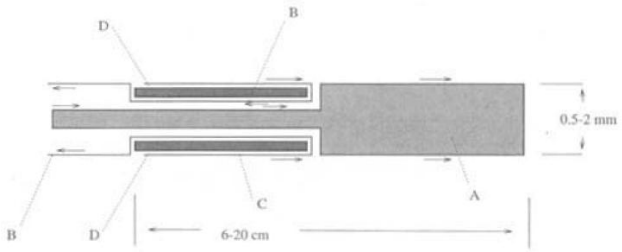


Figure 3.6 Loopless catheter antenna (A) inner conductor (B) primary shield (C) secondary shield (D) insulator [23]

Recently, a single loop receiver coil called an IV MRI probe, as shown in Figure 3.7, has been developed [24]. The IV coil is 1.3 mm in diameter and 57 mm long. Prior to this work, an occlusive balloon, which is commonly used for dragging gallstones out of the bile tract, was used to stabilize the coil mechanically, but IV coils have been successfully used without

balloon stabilization. In the experiment, a rabbit aorta was imaged using the IV MR coil and, for comparison, using a phased-array coil. A resolution of 156 x 156 μm^2 was obtained using the IV MR coil, compared with 352 x 352 μm^2 for the phased-array coil, demonstrating the intrinsic *SNR* advantage of internal coils.

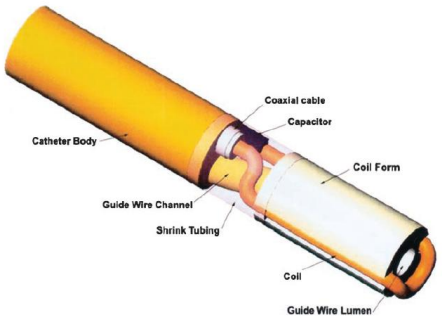


Figure 3.7 a 3D model of a nonobstructive IV MR coil from [24]

Internal RF coils have not only been used for MR imaging, but also for tracking and visualization of catheters. In 2004, catheter tracking and imaging using internal MR coil was demonstrated by Zuehlsdorff et al [25]. The overall receiver configuration involved two coils; a tip tracking coil and a twisted-pair imaging coil. Another example of a combination of MR imaging and tracking was described by Hillenbrand et al. [26]. They used coils formed from two simple solenoids, which were wound around the same main core but in the opposite direction. This design could provide high-resolution image with sufficient *SNR* to resolve the vessel wall. However, the stiffness of the coils was relatively large. Hence, while this design was just suitable for renal arteries (which are relatively large vessels), it could not be used with small branching abdominal vessels. RF coils may also be used to generate therapeutic heating (hyperthermia) in the range 55-90 °C. This procedure is used for cancer treatment [27-30]. Since it can effectively kill tissue in a highly localized manner, but does not cause internal bleeding, it provides a useful alternative to surgery, radiotherapy and chemotherapy.

3.3 Flexible RF Detector for Intrabiliary MRI

All the coils above were made by hand, and consequently have some limitations for intrabiliary MRI. Particularly, they contain many small protrusions likely to snag inside a duodenoscope, and cannot reliably bend through the ninety-degree angle needed to enter the biliary ductal system. As a result, complete integration of both the coil and cable into a fully flexible receiver system are essential.

Considerable attention has been paid to coil miniaturization. First generations of microcoil were designed for NMR microspectroscopy at the cellular level. Peck et al. demonstrated a planar RF coil fabricated on a gallium arsenide (GaAs) substrate as shown in Figure 3.8 [31]. Because the samples are very small, the RF microcoil can be placed close to the object to increase the filling factor. Although the filling factor was increased, the *SNR* was still low due to high resistive losses in the coil. Later, Stocker et al. tried to overcome the high resistive losses using 60-μm planar coil, together with a nonconductive liquid fluorocarbon (FC-43) to reduce susceptibility mismatch [32]. A planar microcoil has also been used in a telemetric system and in vivo microspectroscopy in [33] and [34], respectively. Both planar structures were fabricated on silicon covered with silicon dioxide, and an improved Q-factor was obtained by increasing the height of the conductors or the thickness of the insulator instead of increasing the number of turns of the coil.

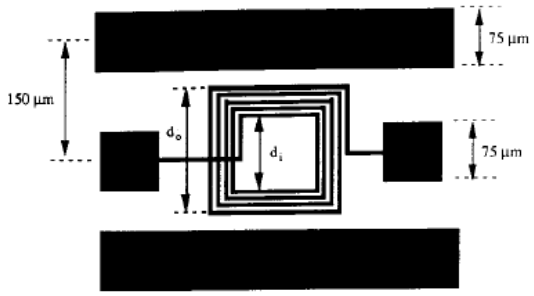


Figure 3.8 Top view of planar microcoil [31]

For standard biochemical experiments, circular planar structures on glass substrates rather than semiconductor substrates are needed [35, 36] as shown in Figure 3.9. To obtain a high Q-factor from this structure, Massin el at. proposed fabrication using SU-8 epoxy photoresist and electroplating [36]. Because of the properties of SU-8, this process can be used to minimize the series resistance to obtain high Q-factor, and also to provide the pads for standard wire bonding to printed circuit board (PCB).

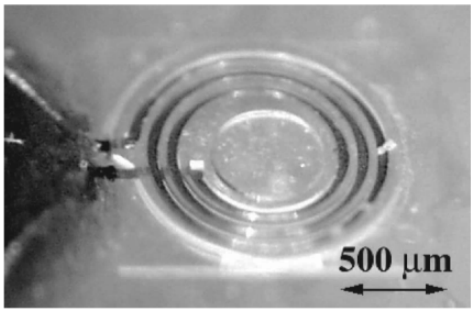
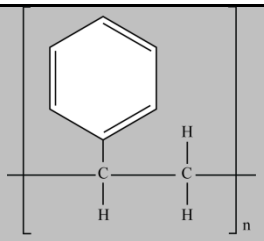
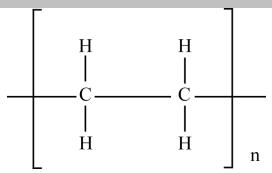
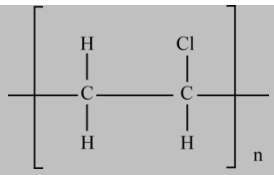
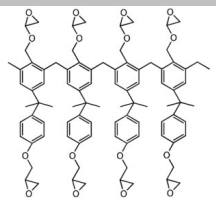
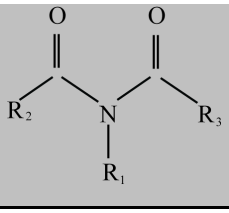


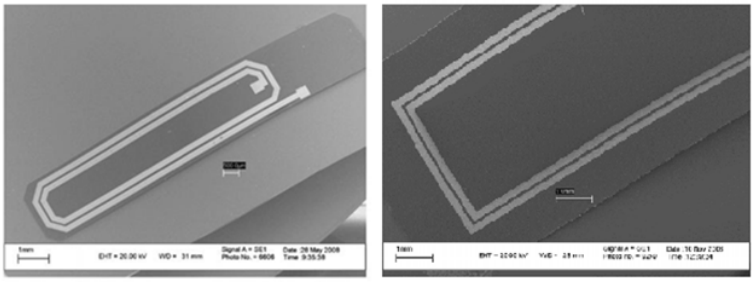
Figure 3.9 A circular planar microcoil on glass substrate [36]

Since then, microcoils studies that use rigid materials as substrate have been challenged by a flexible plastic material known as Kapton or polyimide (PI). This material is a thermal and electrical insulator, that has a excellent mechanical properties and a high chemical resistance. Coutrot el at. first showed a comparison of using glass and polyimide as substrate for microcoil [37]. Although Kapton is not as good as glass, a sufficient Q-factor (~60) can be obtained. Thus, when flexibility is needed, for example, in a tracking system for localization of a catheter [38] or local MRI imaging [39], Kapton is an excellent option. In Table 3.1, we summarise the properties of various plastics use for RF coil applications. As can be seen, PI has repeating polymer units held by amide links and can combine excellent electrical and mechanical properties. However, its chemical structure still contains the ^{1}H element that can cause image artefact [40].

Table 3.1 Properties of various plastic materials

Names	Chemical Structure	Molecular Formula	Density	Melting Point	Dielectric Constant
Polystyrene (PS) or Thermocole		$(C_8H_8)_n$	1.06-1.12 g/cm^3	240°C	2.60
Polyethene (PE) or Poly(methylene)		$(C_2H_4)_nH_2$	0.91-0.97 g/cm^3	195-230°C	3.50
Polyvinyl Choloride (PVC) or Polychloroethylene		$(C_2H_3CL)_n$	1.1-1.45 g/cm^3	100-260°C	3.19
SU-8 2000		-	1.219 - 1.236 g/ml	279-311°C	4.10
Polyimide (PI)		$(R(=O)NR(=O)R)_n$	1490 kg/m^3	none	3.50

For a number of years, the development of microcoils for intrabiliary MRI has been carried out in the Electrical and Electronic Department, Imperial College London. Initial work involved the development of two designs of flexible coil [41]. The first, Type I design was fabricated on semi-rigid SU-8 substrate as shown in Figure 3.10a. and consequently has limitations for practical use. This design must be mounted on a flat surface formed on a catheter. The second, Type II design was fabricated on polyimide, which is intrinsically more flexible and can be wrapped around a catheter as shown in Figure 3.10b.



(a) (b)

Figure 3.10 Two coil designs developed by Imperial College London (a) Type I catheter-based flexible micro coil [41] (b) Type II coil [41]

Experimentally, high-resolution images were successfully obtained from a phantom and from a duct in a resected porcine liver. This result implies that both these designs have the potential to detect very small malignant tissue such as early-stage CCA. However, Type II microcoils are intrinsically more promising and were consequently chosen for future development.

3.4 Periodically Loaded Transmission Lines

In intrabiliary MRI, the cable is no less important than the receiver coil because the signal must be transferred out of the body along the catheter. Previous studies used a coaxial cable in an internal catheter lumen as an output cable, blocking the lumen and preventing the use of a guidewire. One solution is to wrap a thin-film transmission line around the outside of the catheter, using periodic structuring to realise the correct characteristic impedance. In this Chapter, we present the basic concept of periodic transmission lines; more detailed analysis will be presented in a later chapter.

Figure 3.11 shows the equivalent circuit of the unit cell of a periodically structured lumped-element transmission line, which has resistance R and inductance L in the series branch and conductance G and capacitance C in the shunt branch of a section of length 'a'.

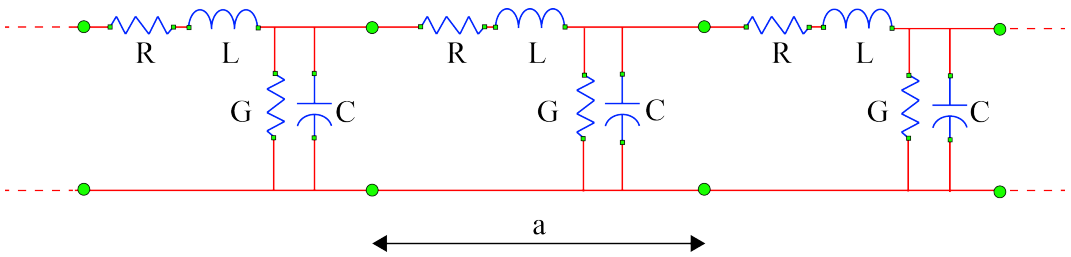


Figure 3.11 Equivalent circuit of a transmission line

Using standard analysis[42, 43], the characteristic impedance (Z_0) can be found as:

$$Z_0 = \sqrt{\frac{R + j\omega L}{G + j\omega C}} \tag{3.4}$$

In a lossless transmission line, the resistance (R) and conductance (G) are very small and can be neglected. In this case we obtain:

$$Z_0 = \sqrt{\frac{L}{C}} \tag{3.5}$$

The dispersion relation in the lossless structure can be also calculated using standard analysis [43]. In the lossless case, we obtain:

$$\frac{\omega}{\omega_0} = 2\sin(\frac{ka}{2}) \tag{3.6}$$

Where $\omega_0$is resonant frequency ($\omega_0 = \frac{1}{\sqrt{LC}}$), k is the propagation constant, a is the length of section in equivalent circuit, and ka is phase shift per section. From Equation (3.6), we can plot the dispersion relation as shown in Figure 3.12. At low frequencies, the variation is a

straight line, but the overall variation is clearly sinusoidal. Propagation can therefore be obtained only up to a maximum frequency $\omega_m = 2\omega_0$. The combination of the characteristic impedance and the cutoff frequency provide useful expressions for determining the inductance and capacitance of experimental transmission lines, as will be described in a later chapter. Clearly the dispersion relation is periodic, with other allowed values of ka including negative ones.

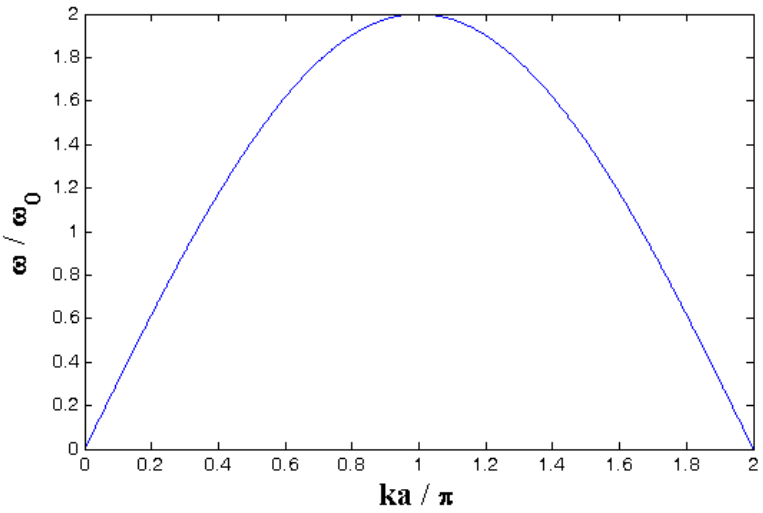


Figure 3.12 Dispersion diagram for a periodic line calculated using Matlab following Equation (3.6)

Other useful expressions can be obtained from the reflection coefficient (S_{11}, or R_V) and the transmission coefficient (S_{21}, or T_V). S_{11} describes the amplitude of the reflected wave (V_R) relative to the incident wave (V_I), while S_{21} represents the amplitude of the transmitted wave (V_T) relative to the incident wave (V_I). These two electrical measurements are usually used for checking a range of frequency, reflection and transmission of the wave between defined ports in transmission lines.

To calculate S_{11} and S_{21}, we consider a discontinuity as shown in Figure 3.13 below.

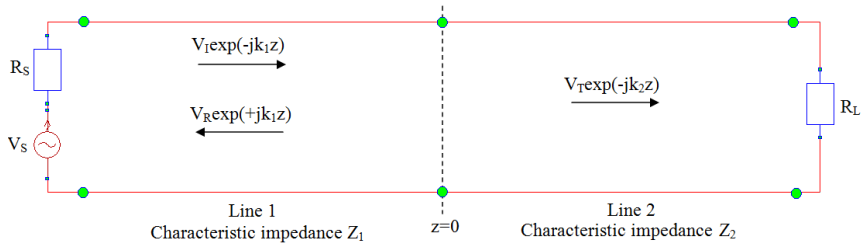


Figure 3.13 Discontinuity in transmission line impedance at z = 0 [44]

Assuming the two lines have characteristic impedance Z_1, and Z_2, standard theory can be used to obtain R_V and T_V as:

$$R_V = \frac{V_R}{V_I} = \frac{Z_2 - Z_1}{Z_2 + Z_1} \tag{3.7}$$

$$T_V = \frac{V_T}{V_I} = 1 + R_V = \frac{2Z_2}{Z_2 + Z_1} \tag{3.8}$$

If we consider a finite line with length d terminated by a known load impedance Z_L as shown in Figure 3.14, we can find another useful parameter; the input impedance (Z_{in}). This impedance describes the impedance seen at the input to the line when a finite length of line is connected to an external circuit.

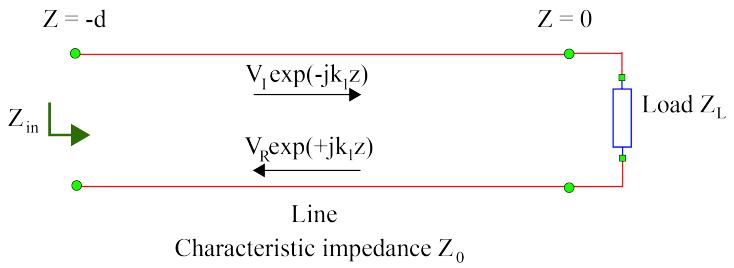


Figure 3.14 Input impedance for a finite line [44]

The input impedance can be found at Z = -d as:

$$Z_{in} = \frac{V_{(-d)}}{I_{(-d)}} = \frac{V_I e^{+jkd} + V_R e^{-jkd}}{\left(\frac{V_I}{Z_0}\right)e^{+jkd} - \left(\frac{V_R}{Z_0}\right)e^{-jkd}} \tag{3.9}$$

Substituting the reflection coefficient V_R/V_I from Equation (3.7) and re-arranging we get:

$$Z_{in} = \frac{Z_1\{Z_2 + jZ_1\tan(k_1 d)\}}{\{Z_1 + jZ_2\tan(k_1 d)\}} \tag{3.10}$$

These expressions will again be very useful for analyzing the properties of experimental transmission lines.

4. PERIODICALLY STRUCTURED THIN-FILM CABLES

This chapter considers the design of a first generation catheter based RF receiver based on a combination of a multi-turn RF coil (for signal detection) and a thin-film cable based on a periodically loaded (photonic bandgap) transmission line (for signal transmission) [45]. These components were modelled and simulated using AWR Microwave Office (MWO). The design of the receiver coil itself is adjusted to meet the specification of ^{1}H MRI, and its performance is compared to simple theory and to experimental data obtained from prototypes fabricated using copper clad Kapton. A complete system with a receiver coil connected to an optimum transmission line is then simulated.

4.1 System Overview

The first generation thin-film detector system consists of a flexible receiver coil [41] and a flexible patterned microstrip cable as shown in Figure 4.1. The basic design was developed by Prof. Richard Syms, and a more detailed design is now described. The electrical components (L, C_M, and C_T, previously shown in Figure 3.1) needed in the resonant detector are physically realized as shown below. The combined system can be wrapped over a hollow catheter scaffold and held in place with heat-shrink tubing as shown in Figure 4.2, leaving the internal lumen of the catheter free for use with a guidewire to assist with cannulation.

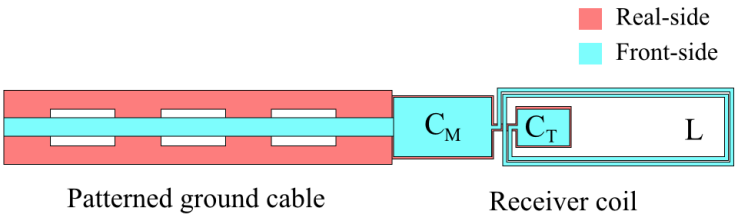


Figure 4.1 Thin-film RF detection system

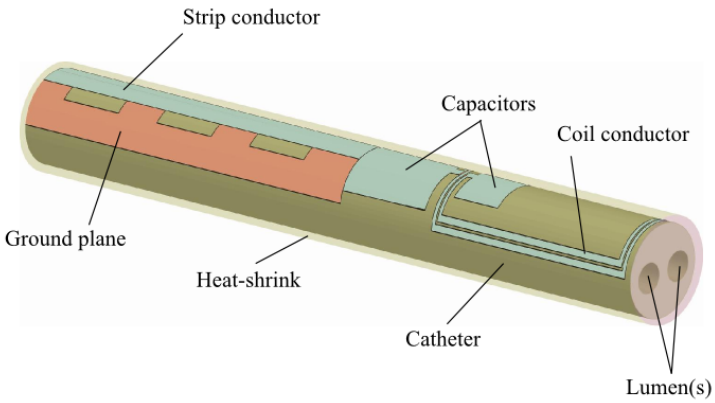


Figure 4.2 Integration of the RF receiver on a catheter scaffold

4.2 RF Microcoil Design

The first component of the thin-film detector system is a flexible receiver coil (coil type II [41]). shown in Figure 4.3. The upper conducting layer is a planar copper structure that contains a two-turn rectangular spiral inductor (measuring A_C x B_C) together with plates for integrated tuning and matching capacitors (measuring A_{CT} x B_{CT} and A_{CM} x B_{CM}, respectively). The lower conducting layer also carries plates for the tuning capacitor and matching capacitor, with matching dimensions. A polyimide layer between the upper and lower layers provides a mechanical substrate and a dielectric interlayer.

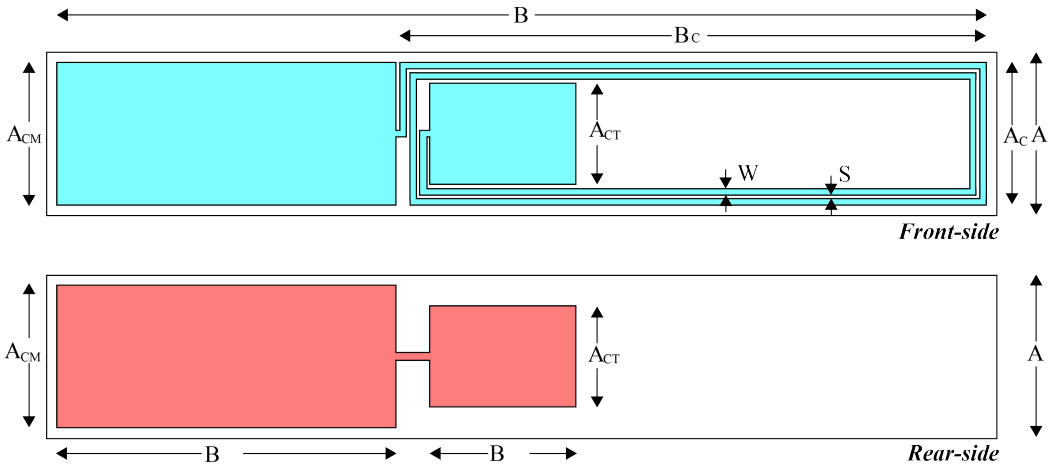


Figure 4.3 Layout of flexible microcoil

4.3 RF Microcoil Modeling and Simulation Set Up

To begin modelling any electromagnetic structure in Microwave Office, its different layers must first be declared. In this case, the layers shown in Figure 4.4 are used. Here, the structure is defined using 5 levels. Layers I and V are air, with thicknesses of t_{A1} and t_{A2} = 30 mm between the model and the perfect conductor of the surrounding enclosure. Layer II is contains the spiral inductor and one pair of capacitor plates, and has a thickness t_C of 35 μm. Its material is copper, with a conductivity of 5.96 x 10^7 S/m. Layer III defines a polyimide dielectric substrate, with a relative permittivity of 3.4 and a thickness of 25 μm. Layer IV is again copper; it contains the second pair of capacitor plates and again has a thickness of 35 μm (t_G). In the first simulation, dielectric loss was omitted.

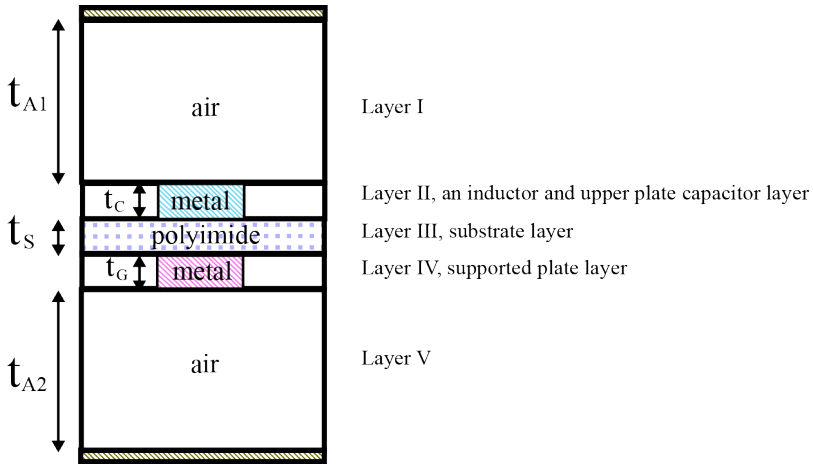


Figure 4.4 Initial definition of layer structure, used for resonant coil

The following geometric parameters were used: A_C = 4.2 mm, B_C = 60.3 mm, W = 200 μm, S = 100 μm, A_{CT} = 3 mm, B_{CT} = 4.3 mm, A_{CM} = 5 mm, B_{CM} = 50 mm. These parameters are represent small variations of the experimental dimensions used in a Type II catheter-based flexible microcoil RF detector [41], in order to tune correctly to 63.4 MHz frequency and match to 50 Ω. To simulate the self resonance of the detector, port 1 is declared at the end of the matching capacitor in Layer II, and port -1 is defined below at Layer IV.

4.4 RF Microcoil Simulation Result

The flexible RF microcoil was first modelled as shown in Figure 4.5a and simulated to observe a self-resonance using the reflection coefficient (S_{11}) as shown in Figure 4.5b below. As can be seen, resonance can be obtained at 63.55 MHz. Matching is good, since the signal reflected by the coil is -20 dB at this frequency. This value is limited mainly by the granularity of the simulation. This model will be used to examine the whole system when a detector is connected to a flexible patterned microstrip cable.

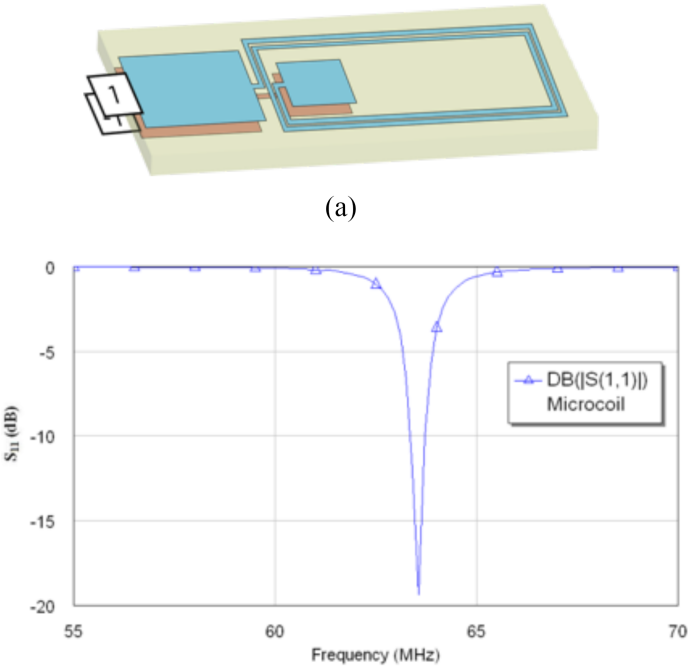
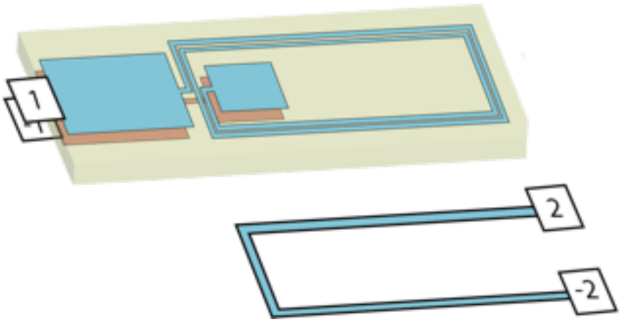


Figure 4.5 RF microcoil numerical testing: (a) arrangement in AWR, and (b) frequency variation of the reflection coefficient S_{11} of the detector

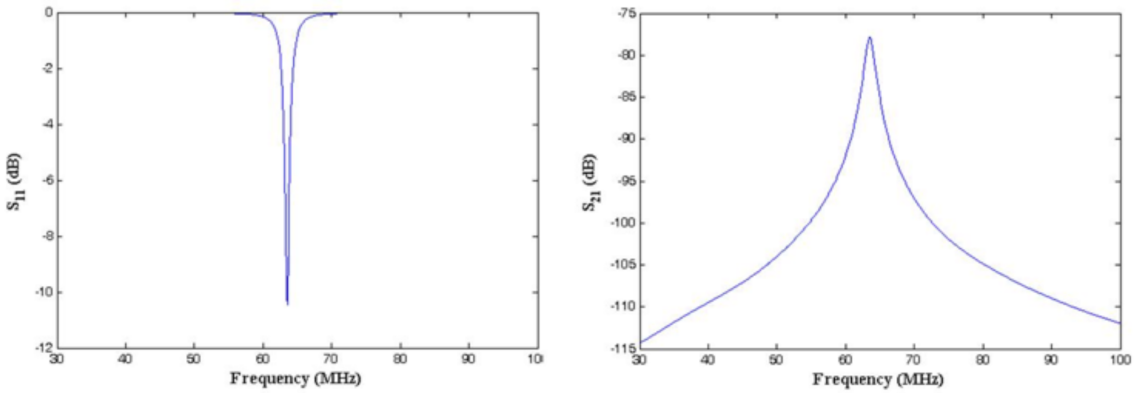
4.5 RF Microcoil Experimental Performance

An experimental thin-film RF detector coil was fabricated by the UK company Clarydon (Willenhall, West Midlands) using double-sided patterning and etching of copper-clad

Kapton (DuPont, Circlevill, OH, USA). To assess its electrical performance, the microcoil was connected to port 1 of an Agilent Network Analyser, and a simple one-turn loop coil was connected to port 2 to act as a weakly coupled probe as shown in Figure 4.6a. The frequency dependence of S_{11} and S_{21} were then measured as shown in Figure 4.6b and Figure 4.6c below. The resonant frequency was tuned by carefully trimming the size of the tuning capacitor using a pair of scissors. The best frequency that can be obtained in this experiment is 63.53 MHz. The amplitude of S_{11} was then matched to 50 W impedance by mechanically trimming the matching capacitor. This adjustment also affects the resonant frequency, but only slightly.



(a)



(b) (c)

Figure 4.6 Experimental frequency variation of the scattering parameters of a thin-film RF detector; (a) arrangement of the RF detector with an additional transducer; (b) frequency variation of the reflection coefficient S_{11}; (c) frequency variation of the transmission coefficient S_{21}

4.6 Thin-film Cable Design

For the second part of the thin-film detector system, a flexible microstrip cable was developed, by combining features from the well-known microstrip and coplanar waveguide (CPW) structures. Figure 4.7 shows a microstrip waveguide, which consists of a conducting track separated from a ground plane by the dielectric substrate. The characteristic impedance of such a line has been widely studied over the years, and is given by Equations (4.**1**)-(4.**2**) [46, 47]. These equations show the impedance of the line mainly depending on the width (W) of the track and the thickness (d) of the substrate.

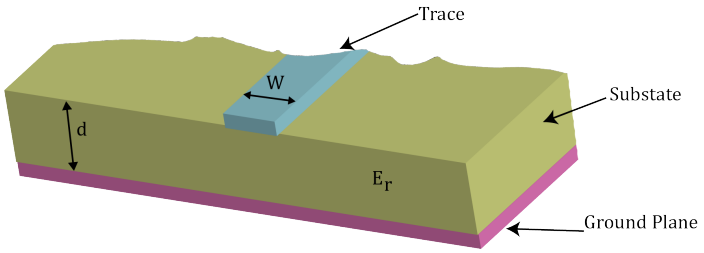


Figure 4.7 The microstrip with the physical variable used for calculating impedance [48]

$$\varepsilon_e = \frac{\varepsilon_r + 1}{2} + \frac{\varepsilon_r - 1}{2} \cdot \frac{1}{\sqrt{1 + 12d/W}} \tag{4.1}$$

$$Z_0 = \begin{cases} \dfrac{60}{\sqrt{\varepsilon_e}} \cdot \ln\left(\dfrac{8d}{W} + \dfrac{W}{4d}\right), & \dfrac{W}{d} \le 1 \\ \dfrac{120\pi}{\sqrt{\varepsilon_e} \cdot \left(\dfrac{W}{d} + 1.393 + 0.667 \cdot \ln\left(\dfrac{W}{d} + 1.444\right)\right)}, & \dfrac{W}{d} \ge 1 \end{cases} \tag{4.2}$$

Here ε_e is the effective permittivity, and ε_r is the relative permittivity of the substrate.

Figure 4.8 shows a coplanar waveguide, which also has a thin conducting line, but has two ground planes running adjacent and parallel to the strip separated by small gaps. Its characteristic impedance is given by Equations (4.**3**)-(4.**5**) [49]. As can be seen, the

impedance depends on the small gaps between the middle strip and the ground planes (*b-a*), and the width of the middle strip (*2a*).

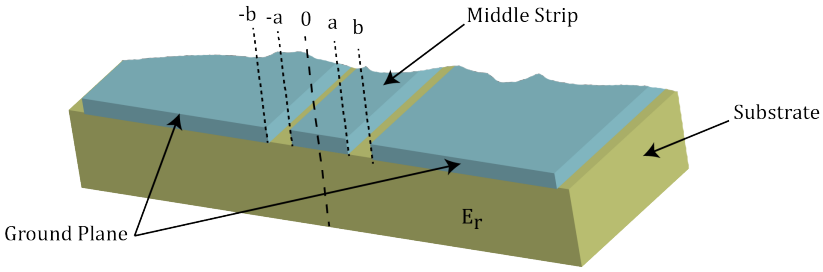


Figure 4.8 The coplanar waveguide with physical parameters for calculating impedance [49]

$$C = (\varepsilon_r + 1)\varepsilon_0 \frac{2a}{b} \tag{4.3}$$

$$V_{ph} = \left(\frac{2}{\varepsilon_r + 1}\right)^{1/2} \cdot c \tag{4.4}$$

$$Z_0 = \frac{1}{CV_{ph}} \tag{4.5}$$

Here C represents capacitance per unit length, ε_0 is the vacuum permittivity, V_{ph} is the phase velocity, c is the velocity of light in free space.

Using these formulae, the behaviour of the two different waveguide structures structures were investigated. For the microstrip, the width of the conductor and was varied, while the thickness of the dielectric was fixed at 25 μm (the maximum value likely to provide a suitably flexible circuit). Similarly, for the CPW structure, the width of the centre conductor was varied, while the electrode gap was fixed at 1 mm (the minimum value likely to be printed reliably over long lengths). Figure 4.9 shows the dependence of the characteristic impedance with conductor width. As can be seen, neither structure can provide 50 Ω

impedance on its own; microstrip impedances are typically too low, while CPW impedances are too high.

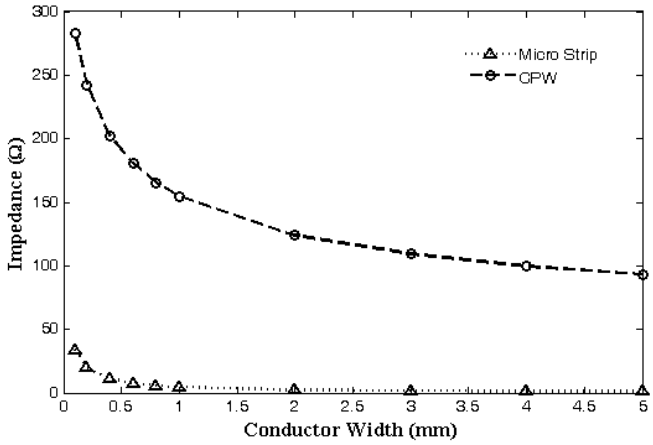


Figure 4.9 Variation of characteristic impedance with conductor width for microstrip and CPW on 25 μm polyimide

For CPW, 50 Ω impedance cannot be obtained even when the electrode gaps (*b* - *a*) are varied, after fixing the width of the center strip at 1 mm as shown in Figure 4.10.

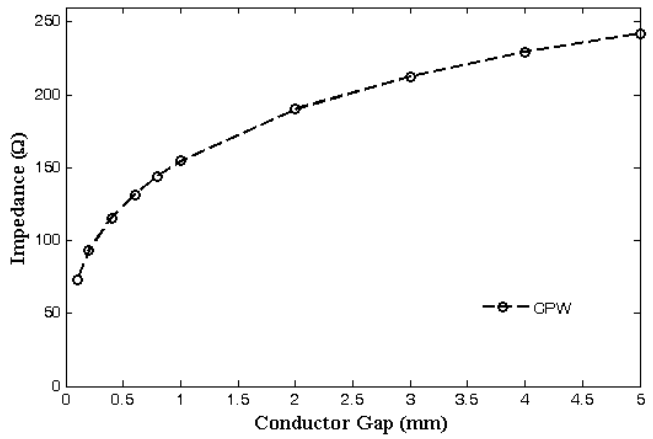


Figure 4.10 Variation of characteristic impedance with electrode gap for CPW

To obtain a more appropriate and controllable impedance in a flexible format, an alternative photonic band-gap (PBG) waveguide was developed, that combines elements of microstrip and CPW as shown in Figure 4.11 below. The structures are similar to Photonic band gap (PBG) microstrip lines [50, 51], which share some of the characteristics of periodic crystals such as forbidden propagation bands. These PBG waveguides are well-known artificially engineered periodic structures, which have been studied for centuries. They have been widely used for applications in the microwave and millimetre-wave region, such as filters [52-54], particle accelerators [55], amplifiers [51], resonators [56], and transmission lines [57]. The design in Figure 4.11 is a PBG waveguide based on a microstrip with a periodically perforated ground plane, whose characteristic impedance and cutoff frequency may be adjusted by varying a small number of key dimensions.

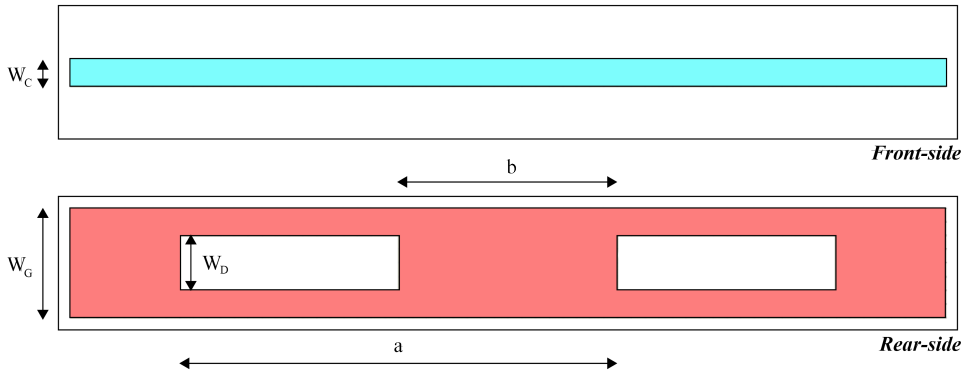


Figure 4.11 Photonic-bandgap transmission line

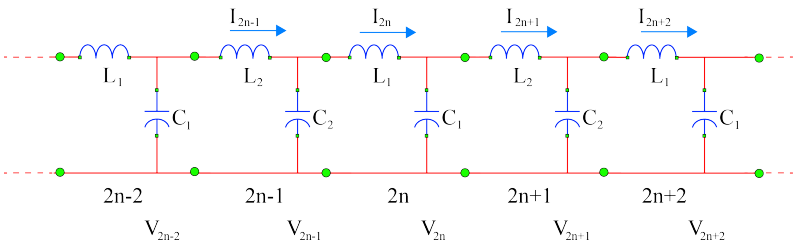
As Figure 4.11 shows, the upper layer of the transmission line is a uniform conductor strip of width (W_C). The second layer is a uniform dielectric layer, and the lower layer is a perforated ground of overall width (W_G) and defect width (W_D). The period is '*a*', and the length '*b*' represents the non-defect or capacitor area. From these parameters, several designs were created by varying a ratio (b/a) as shown in **Table 4.1**.

Table 4.1 Parameters of simulated PBG cable designs

b (*mm*)	*a* (*mm*)	Ratio *b*/*a* (*β*)
15	16	0.9375
14	16	0.875
12	16	0.75
8	16	0.5
4	16	0.25
2	16	0.125
1	16	0.0625
0.5	16	0.03125
0.25	16	0.015625

4.7 Thin-film Cable Analytical Model and Theoretical Equation

For a thorough understanding of the cables, an analytic theory of photonic bandgap cables is first presented. Analysis of such structures may be traced back to Brillouin, who developed a model for one-dimensional diatomic crystals [58], that can also be applied to a microstrip with a periodically perforated ground plane. Figure 4.12a shows a lumped element transmission line model of a diatomic electrical circuit, which is a good representation of the photonic bandgap transmission line shown in Figure 4.12b. Here L_1 and C_1 are the inductance and the capacitance in the defect region, and L_2 and C_2 are the values between.



(a)



(b)

Figure 4.12 (a) Equivalent circuit for a diatomic electrical lattice [58] (b) physical structure of a microstrip with a periodically patterned ground plan

For Figure 4.12 (a), Brillouin derived the dispersion relation exactly, as:

$$\omega^2 = \frac{1}{2}\left(\frac{1}{L_1}+\frac{1}{L_2}\right)\left(\frac{1}{C_1}+\frac{1}{C_2}\right) + \sqrt{\frac{1}{4}\left(\frac{1}{L_1}+\frac{1}{L_2}\right)^2\left(\frac{1}{C_1}+\frac{1}{C_2}\right)^2 - 4\frac{\sin^2 k}{L_1 L_2 C_1 C_2}} \tag{4.6}$$

Prof. Richard Syms has developed another aspect of the dispersion relation, as follows. If $L_1 >> L_2$ and $C_2 >> C_1$, as is often the case, the structure can be approximated by a monatomic lattice. With this simplification, the characteristic impedance depends on the unit cell that is assumed. The exact choice of cell depends in turn on how the cable is terminated. 'T', 'Π' and 'L' shaped unit cells are all possible. For example, the equivalent circuit a cable with a Π cell (i.e. a cable that is terminated in the middle of the capacitor region) is as shown in Figure 4.13.

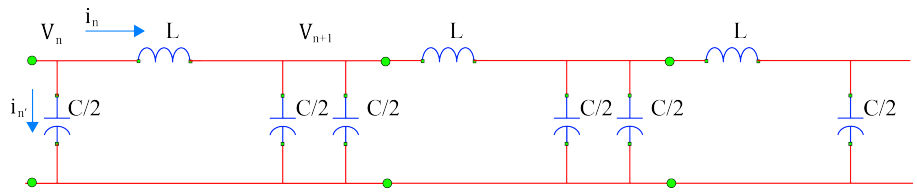


Figure 4.13 Equivalent circuit for a cable model based on a Π unit cell

In this case, the impedance Z_0 can be defined as shown below:

$$Z_0 = \frac{V_n}{i_n + \frac{i_{n'}}{2}} \tag{4.7}$$

If we now assume that $V_n = V_0 e^{(-jkna)}$ and $i_n = i_0 e^{(-jkna)}$ and $V_{n+1} = V_n - j\omega L i_n$, Equation (4.7) becomes:

$$Z_0 = \frac{\frac{-j\omega L i_0}{e^{(-jka)} - 1}}{i_0 + \frac{j\omega C}{2}\left(\frac{-j\omega L i_0}{e^{(-jka)} - 1}\right)} \tag{4.8}$$

Rearranging Equation (4.8) using the dispersion equation (Equation (3.6)), we finally obtain:

$$Z_0 = \sqrt{\frac{L}{C}} \frac{1}{\cos\left(\frac{ka}{2}\right)} \tag{4.9}$$

In general, Z_0 depends on $\cos\left(\frac{ka}{2}\right)$. When $ka \ll 1$, which occurs at low frequency, this term approximates to unity. The characteristic impedance, which we define as the DC impedance, is therefore $Z_0 \sim \sqrt{\frac{L}{C}}$, a real quantity that may easily be matched to 50 Ω.

4.8 Thin-film Cable Modelling and Simulation Set Up

Thin film cables were modelled using AWR MWO. For the cable, layers were defined as previously shown in Figure 4.4, and the assumed cable layout was as shown in Figure 4.11. Four main model variants were simulated as shown in Table below. The variable '*b*' was also varied, following the ratio *b/a* as previously shown in Table 4.1. Port 1 was set as the excitation port and port 2 as a termination.

Table 4.2 Parameters used for modelling

Design	W_C (mm)	t_s (µm)	W_G (mm)	W_D (mm)	t_c (µm)	a (mm)	b (mm)
1	1.0	25	4.0	2.0	35	16	variable
2	1.0	50	4.0	2.0	35	16	variable
3	0.5	25	4.0	1.5	35	16	variable
4	0.5	50	4.0	1.5	35	16	variable

To simulate the models more accurately, the default option of meshing a conductor with zero thickness was removed. Real 3-dimensional models require a finite conductor thickness, because the skin effect implies that the current tends to flow at the surface of metal layers rather than their core. Moreover, the current density changes more rapidly at the edge of the metal. High mesh density is therefore needed for accurate results. Figure 4.14 shows the difference between low and high meshing options in cable models.

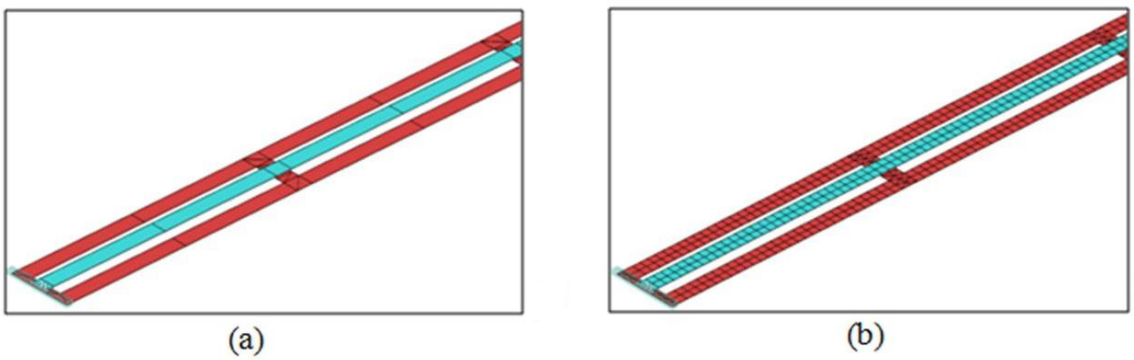


Figure 4.14 Meshed structure with (a) low and (b) high mesh density

4.9 Thin-film Cable Simulation Results

To investigate the behaviour of a PBG microstrip cable, 9 sections were simulated as shown in Figure 4.15a. The parameter '*d*' represents the length of the line. The impedance of the line Z_{line} is the term of interest. However, Z_{in} and Z_{port} (which was set 50 Ω) were also used to extract Z_{line} from simulated data.

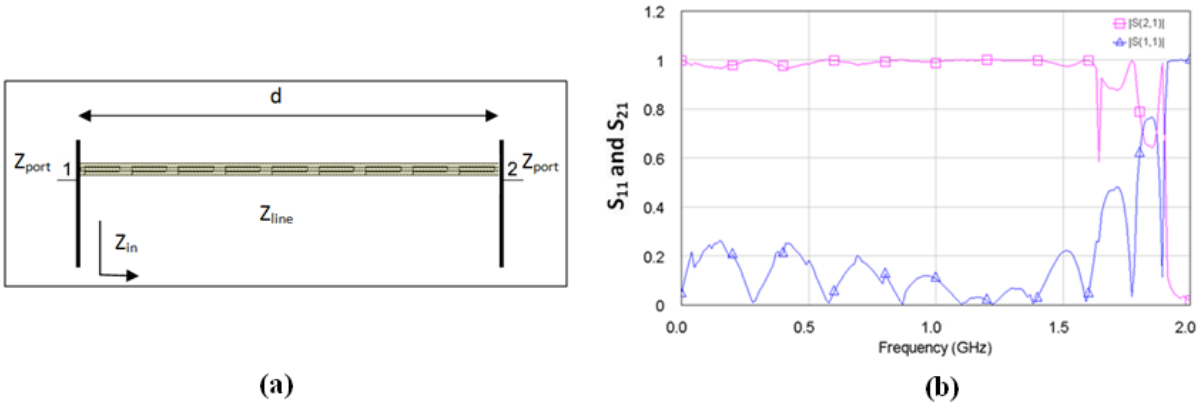


Figure 4.15 (a) 9 sections of PBG microstrip with periodically patterned ground plane (b) Frequency dependence of S_{11} and S_{21} with $b/a = 0.5$

The frequency dependence of the reflection coefficient (S_{11}) and transmission coefficient (S_{21}) were first computed for the lossless case, as shown in Figure 4.15. As can be seen, there are 9 resonant peaks. These correspond to the excitation of standing waves in the line, due to an impedance mismatch between the source (or load) and the line. The frequency range shown here greatly exceeds that needed for MRI, but allows the cutoff of the acoustic band to be seen at 1.85 GHz in the frequency variation of S_{21}.

The variation of S_{11} was then used to extract Z_{line}, using the equation for the reflection coefficient given previously (3.7). This result can be applied to the data shown in Figure 4.15a by re-arrangement, to get:

$$Z_{in} = \frac{Z_{port}(1 + R_v)}{(1 - R_v)} \tag{4.10}$$

Again, Z_{in} is the input impedance, $Z_{port} = Z_0$ *is the characteristic impedance*, R_v is the reflection coefficient or S_{11}, and the previous input impedance in Equation (3.10) may be applied to find the line impedance as:

$$Z_{in} = \frac{Z_{line}\{Z_{port} + jZ_{line}\tan(kd)\}}{\{Z_{line} + jZ_{port}\tan(kd)\}} \tag{4.11}$$

Z_{line} may be extracted from the special case of the input impedance when $\tan(kd) = \pm\infty$ (which corresponds to a resonance). This condition may easily be identified from the frequency response plots, since it corresponds to a peak in reflection. In this case we get:

$$Z_{in} = \frac{{Z_{line}}^2}{Z_{port}} \tag{4.12}$$

Combining Equations (4.10) and (4.12) we then obtain:

$$Z_{line} = Z_{port}\sqrt{\frac{(1 + R_{vmax})}{(1 - R_{vmax})}} \tag{4.13}$$

From Equation (4.13), Z_{line} can be extracted from **Figure 4.15**b to give the results shown in **Table 4.3** below. The results show a steady rise in impedance with frequency, from an initial value of around 30 Ω.

Table 4.3 The extracted impedance variation for *b/a* = 0.25

Peak	Freq (GHz)	*Rv*	Z_{line} (Ω)
1	0.165	0.259	29.42
2	0.417	0.254	29.73
3	0.690	0.191	33.94
4	0.990	0.138	37.82
5	1.169	0.032	46.82
6	1.330	0.064	56.94
7	1.510	0.214	77.26
8	1.690	0.460	133.59
9	1.850	0.749	343.80

This data may be compared with the analytic prediction as previously shown in Equation (4.**9**), which may be re-arranged in terms of frequency as:

$$Z_0 = \sqrt{\frac{L}{C}} \frac{1}{\sqrt{1 - (\frac{\omega}{2\omega_0})^2}} \tag{4.14}$$

Here $\omega_0 = \frac{1}{\sqrt{LC}}$. At DC, this reduces to $Z_{0D} = \sqrt{\frac{L}{C}}$. From this value, and that of ω_0, the inductance and capacitance can be extracted as:

$$C = \frac{1}{Z_0 \omega_0} \tag{4.15}$$

$$L = \frac{Z_0}{\omega_0} \tag{4.16}$$

From the simulation in Figure 4.15b, the cutoff frequency can be read as 1.86 GHz and the impedance at DC can be measured as 29.42 Ω. Using this values, we can calculate the capacitance as C = 5.83 pF, and the inductance as L = 5.04 nH. We can also use Equation (4.9) to calculate theoretical impedance data to compare with the data extracted from simulations as shown in Table 4.4.

Table 4.4 Theoretical data predicted from Equation (4.9), for comparison with **Table 4.3**

Peak	Freq(GHz)	$\omega = 2\pi f$ (GHz)	Z_0 from equation
1	0.165	1.04	29.53
2	0.417	2.62	30.19
3	0.690	4.34	31.68
4	0.990	6.22	34.77
5	1.169	7.35	37.86
6	1.330	8.36	42.15
7	1.510	9.49	50.54
8	1.690	10.60	70.98
9	1.850	11.60	339.10

Data in **Table 4.3** and **Table 4.4** can be compared graphically as shown in Figure 4.16 below. As can be seen, the extracted data and the theoretical data are quite similar up to at least 1 GHz. A DC impedance of ~29.50 Ω is obtained in both cases, then the impedance rises rapidly to infinity at the cut off frequency.

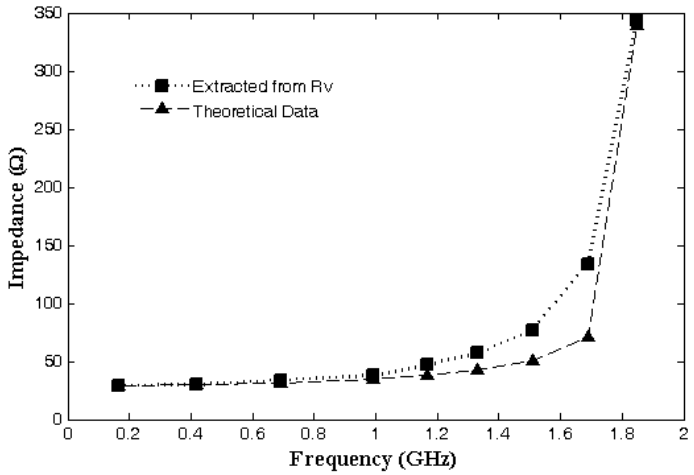


Figure 4.16 Comparison of the variations of impedance predicted by the numerical and analytic models (Equation (4.9))

However, the initial model with β = 0.25 clearly cannot provide the required 50 Ω impedance. The ratio β was therefore varied, to find the likely effects. It was found that the DC impedance can be raised by reducing the value of β, as shown in Figure 4.17. In the process, the cutoff frequency is also increased.

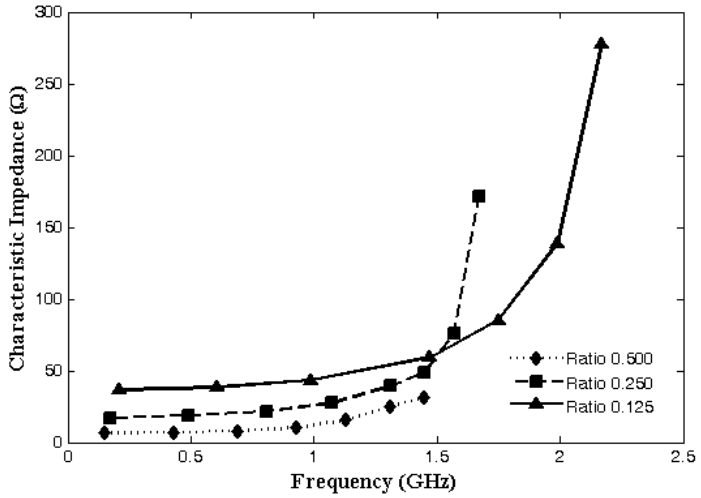


Figure 4.17 Frequency variation of impedance, for several values of β

Figure 4.18 shows the results of simulations for a number of different PBG transmission line models with different substrate thickness and conductor widths. Each variation shows impedance decreasing with β, and in each case 50 Ω impedance can be achieved for a suitable value of β.

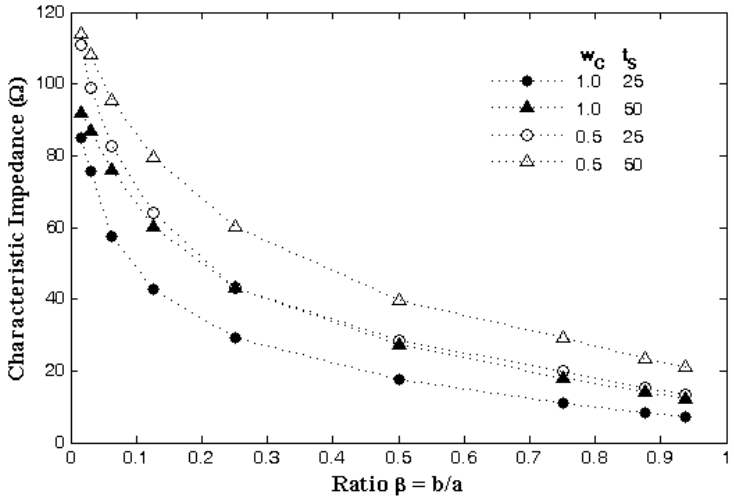


Figure 4.18 Variation of DC impedance with β, for different PBG waveguide models

Figure 4.19 shows the corresponding variation of the cutoff frequency $f_m = \frac{\omega_m}{2\pi}$ with β. As can be seen, f_m lies in the GHz range in each case. However, the variations are approximately parabolic, with a minimum at intermediate values of β (the most likely case).

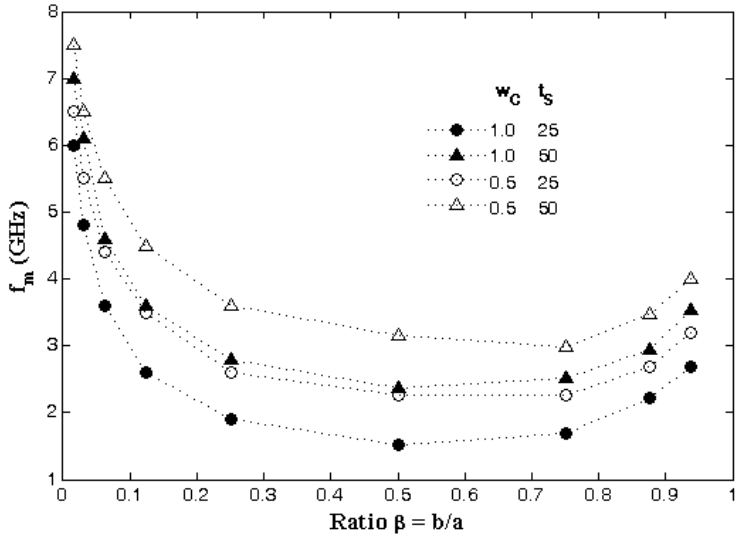
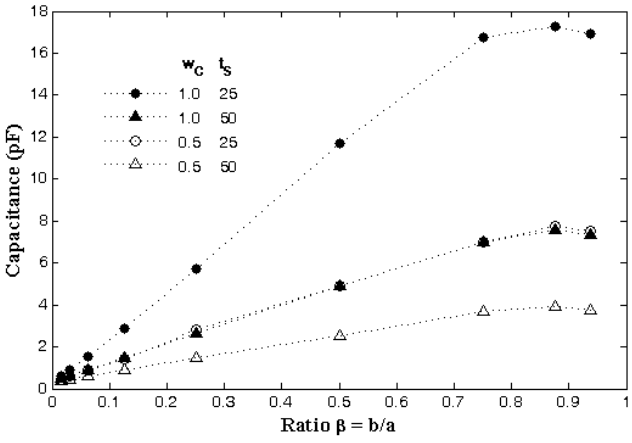


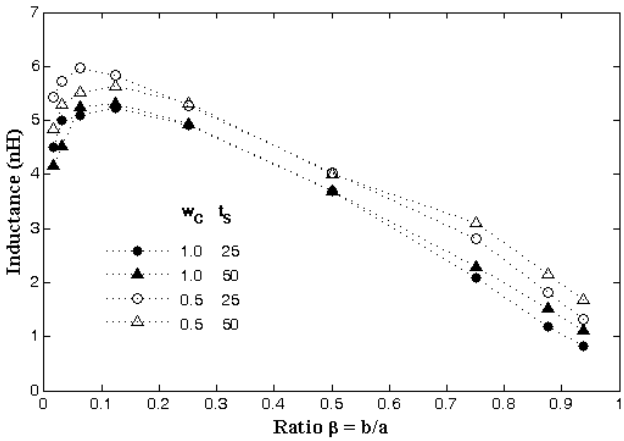
Figure 4.19 Extracted variation of the cutoff frequency f_m with β

4.10 Thin-film Cable Capacitance and Inductance Extraction

Capacitance and inductance are also features of interest. Their variations with β may also be extracted following Equations (4.15) and (4.16) as shown in Figure 4.20a. These data show linear variations of capacitance with β up to ~ 0.8; at this point, the variations all flatten off, most probably due to the effect of fringing fields. As expected, the capacitance is proportional to the conductor width and inversely proportional to the dielectric thickness. The variation of inductance is also quasi-linear as shown in Figure 4.20b. However, this time the dielectric thickness has almost no effect, since the conductors are almost coplanar.



(a)



(b)

Figure 4.20 Variation of extracted values of (a) capacitance and (b) inductance with $\beta = b/a$

4.11 Thin-film Cable Loss Estimation

In previous simulations, loss was neglected. For the analytical model, loss may be included, by inserting a series resistance into the inductor and a shunt conductance into the capacitor as shown in Figure 4.21.

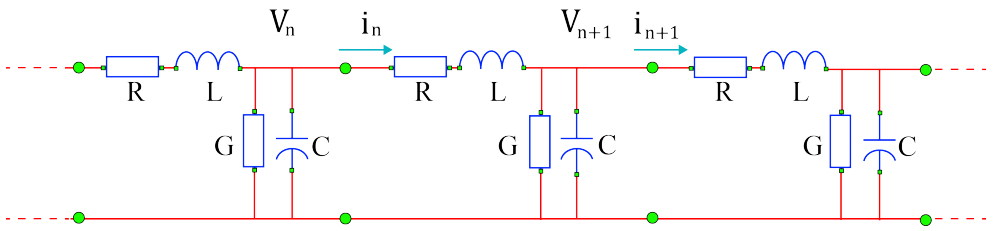


Figure 4.21 Equivalent circuit of lossy transmission line

Kirchoffs law may then be used to obtain the modified nodal equations:

$$V_{n+1} = V_n - (R + j\omega L)I_n \tag{4.17}$$

$$I_{n+1} = I_n - (G + j\omega C)V_{n+1} \tag{4.18}$$

Making the standard travelling wave assumptions, the dispersion equation may now be obtained as:

$$4sin^2\left(\frac{ka}{2}\right) + (R + j\omega L)(G + j\omega C) = 0 \tag{4.19}$$

Assuming that the propagation constant is complex, so that $k = k' - jk''$, and that loses are small, we get:

$$\frac{\omega}{\omega_0} = 2\sin\left(\frac{k'a}{2}\right) \tag{4.20}$$

And :

$$k''a = \frac{\omega_m\{RC + GL\}}{4\cos\left(\frac{k'a}{2}\right)} \tag{4.21}$$

Equation (4.21) represents the attenuation of the signal in the lossy transmission line. At RF frequencies, the skin depth given by $\delta_s = 1/\sqrt{\omega\mu_0\sigma/2}$ determines the series resistance of a conductor which can be expressed as $R = a/(2\sigma W_c\delta_s)$. As a result, R rises only slowly with ω (as $\sqrt{\omega}$) and can typically be neglected. Equation (4.21) can then be approximated as:

$$k''a \approx \frac{\omega_m GL}{4} \tag{4.22}$$

Similarly, the loss tangent determines the conductance G, which can be expressed as $G = \omega Ctan(\delta)$. This conductance will increase linearly with ω. For very low frequency, Equation (4.22) approximates to;

$$k''a \approx \frac{\omega}{\omega_m}\tan(\delta) \tag{4.23}$$

Using this result, propagation loss can be written as $L = (20\omega/a\omega_m)\tan(\delta)/log_e(10)$ dB/m or as:

$$Loss = \frac{10\omega\sqrt{L_pC_p}\sqrt{\{(1-\beta)\beta\}}\tan(\delta)}{\log_e(10)}\,dB/m \tag{4.24}$$

Where L_p is inductance per unit length, C_p is capacitance per unit length, and β is b/a.

Using Equation (4.24), the variation of loss with β can be plotted as shown in Figure 4.22, for the same design variations as before. The variations are again parabolic, with a maximum when b/a = 0.5. Losses are higher with thinner (25 μm) dielectric than with thicker (50 μm) dielectric. Moreover, the graph shows that the loss can be decreased, by reducing the conductor width for a given dielectric thickness, so that losses are lower for the 0.5 mm conductor width than for 1.0 mm.

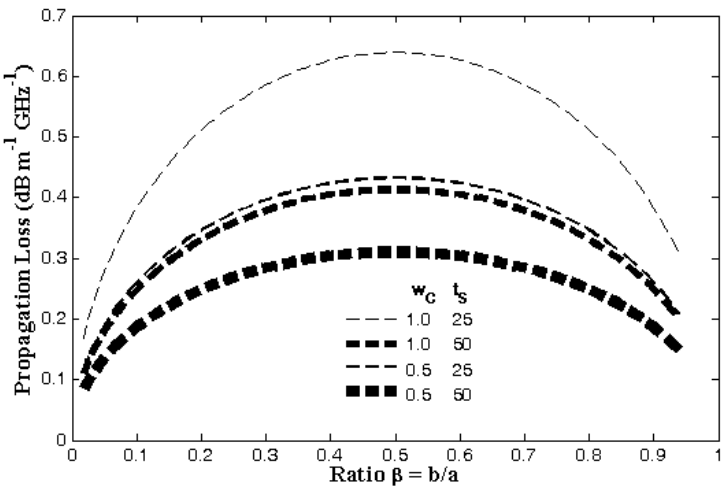


Figure 4.22 Analytic variation of PBG waveguide propagation loss with $\beta = b/a$

To verify these analytic predictions, numerical simulations were also carried out using Microwave Office, using the loss tangent of δ = 0.0018 for kapton [59]. The loss can be extracted from the slope of a variation of S_{21} at low frequency. To obtain an accurate result, the model length was increased to 40 sections. However, this led to very lengthy calculation times. Figure 4.23 shows the variation of loss with β for different line parameters. As can be seen, loss increases with b/a. However, the agreement with the analytic model is only moderate, most probably due to the neglect of other loss mechanisms.

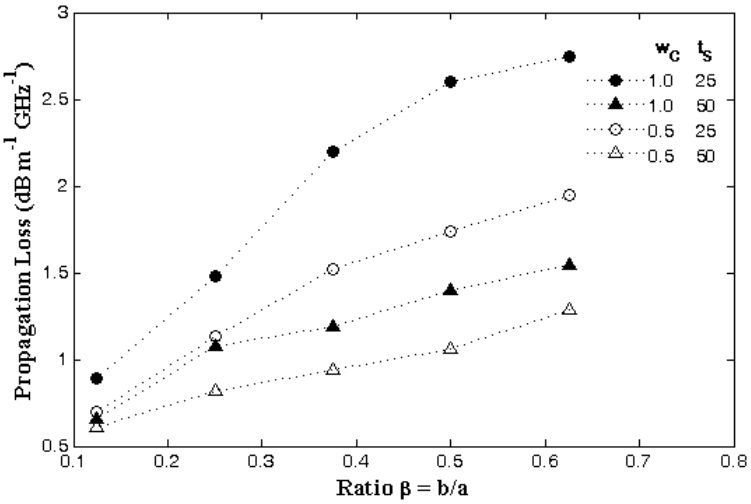


Figure 4.23 Numerical variation of PBG waveguide propagation loss with $\beta = b/a$

4.12 Thin-film Cable Experimental Verification

Experimental cables were again fabricated using copper-clad Kapton, again by the UK company Clarydon. However, because cable fabrication was considerably more complicated, the process is described in more detail. Seven values of the ratio *b/a* (1, 1/2, 1/4, 1/8, 1/16, 1/32, 1/64) were considered, together with a uniform microstrip, and the general parameters presented in Table 4.2 were used. However, the real cables were longer (2 m). The cable design layouts were printed using a pair of photomasks, which were formed from Mylar-coated silver halide on a polyester backing.

The fabrication process is shown in Figure 4.24. The starting material was copper-clad polyimide (1). Each side was then coated with a 175 micron thickness of laminated photoresist (2). The sensitised PCB was then sandwiched between the two photomasks. To obtain correct alignment between the photomasks and the PCB, a set of pins was passed through mating holes in each component. The space between the layers was then evacuated. Subsequently, an UV lamp was used to expose each side of the PCB, transferring, the design patterns from the photomasks into the photoresist (3, 4). Next, resist development (5) and metal etching (6) were carried out with the PCB horizontal, using a leader board to allow

dragging through a spray developer and a spray etcher. The resist was then stripped, leading finally to the completed cable (7).

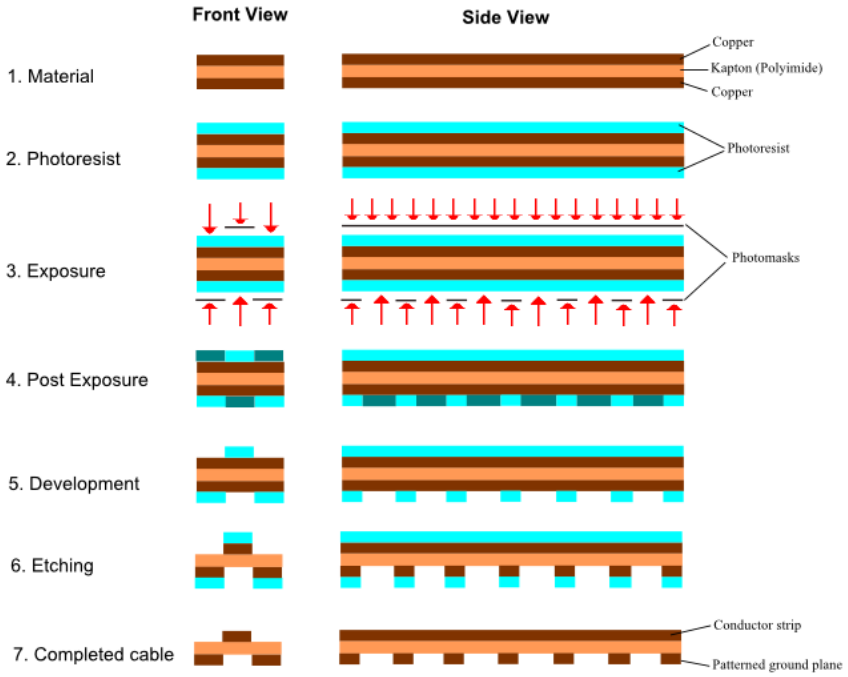


Figure 4.24 Process for thin-film PBG cable fabrication

The electrical performance of the completed cable was measured using an Agilent electronic network analyser by Prof. Richard Syms. Frequency variations of the reflection coefficient (S_{21}) and transmission coefficient (S_{11}) were obtained as shown in Figure 4.25a and Figure 4.25b. As can be seen, the phonic bandgap or patterned microstrip cable has much lower transmission loss than the uniform microstrip, and losses are reduced as the ratio *b/a* is reduced. Also, the reflection coefficient (S_{11}) graph in Figure 4.25b is quite similar to the S_{21} graph from simulation. These results are in agreement with Figure 4.20 when additional loss is associated with capacitance of the cable due to the significant tan(d) of the interlayer dielectric. The uniform microstrip has a larger average value of capacitance, which results in higher propagation loss.

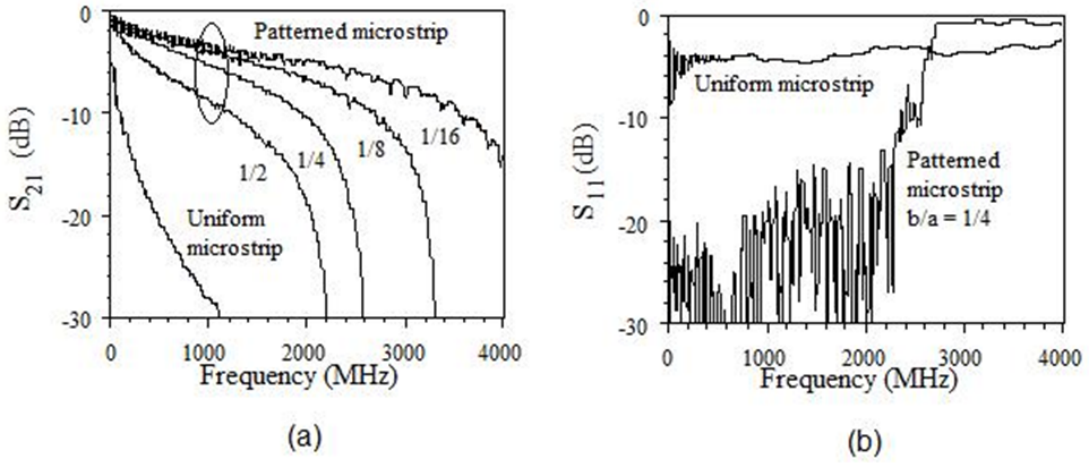


Figure 4.25 Experimental frequency variation of the scattering parameters of thin film PBG cable (a) S_{21} and (b) S_{11}

The propagation loss and characteristic impedance may be extracted from data of this type, as was done for the simulation data. The experimental variations of characteristic impedance are shown in Figure 4.26. The overall variations are very similar to the simulation data previously shown in Figure 4.18.

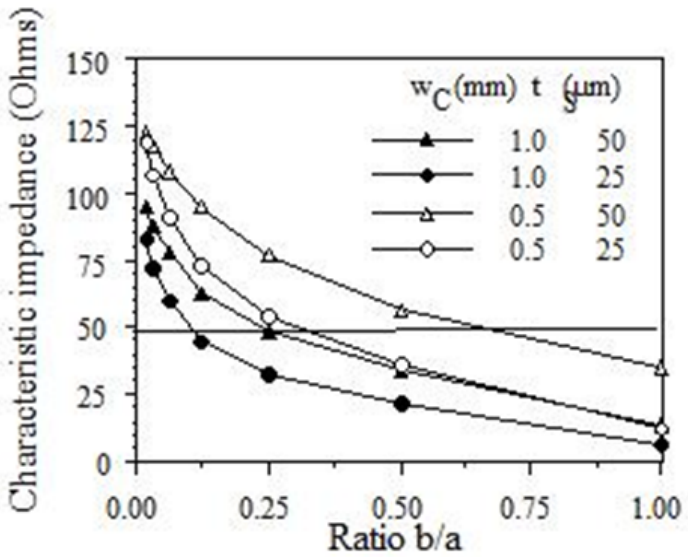
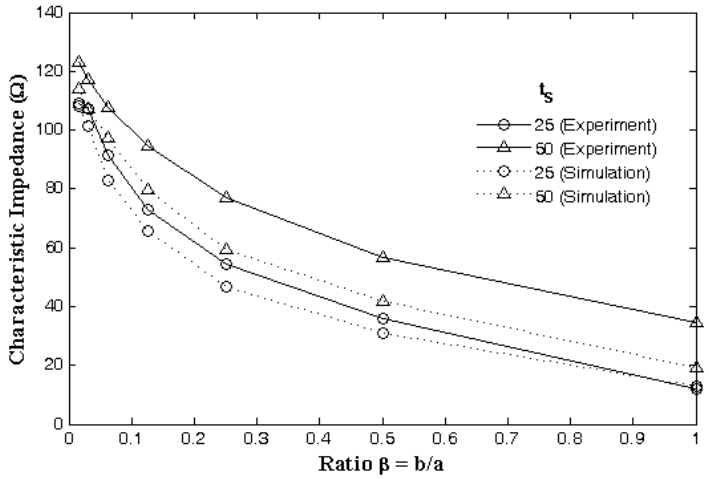
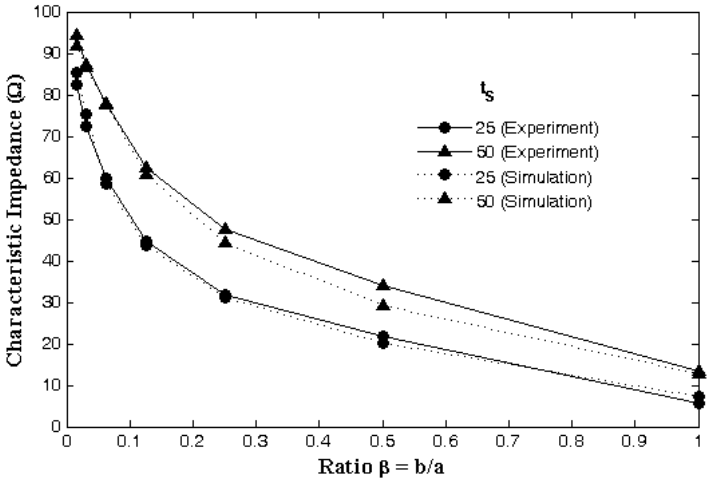


Figure 4.26 Experimental variation of DC characteristic impedance with the layout parameter *b/a*

For a detailed comparison, experimental and theoretical data are plotted together as shown in Figure 4.27a and Figure 4.27b, which compares results for lines with 0.5 mm and 1.0 mm wide conductors. In each case, the impedance is very low for $\beta > 0.5$, but rises steadily as *b/a* is reduced to zero. Although the experimental and the simulated data have the same trend, there are still noticeable differences between them. However, the agreement improves for wide conductors. These data confirm that periodically patterned lines can provide impedance matching to a designed value by careful choice of parameters.



(a)



(b)

Figure 4.27 Comparison between experimental and theoretical variations of impedance for conductor widths of (a) 0.5 mm and (b) 1.0 mm

Figure 4.28 shows the experimental variation of loss. While these data have a similar variation to the earlier theoretical predictions, there are still major unexplained differences. For instance, losses are high with thicker (50 μm) than with thinner (25 μm) while the analytic and theoretical results are opposite. One possible explanation is uncertainty in the dielectric properties of the Kapton layer, which are very poorly described in the manufacturer's data sheet.

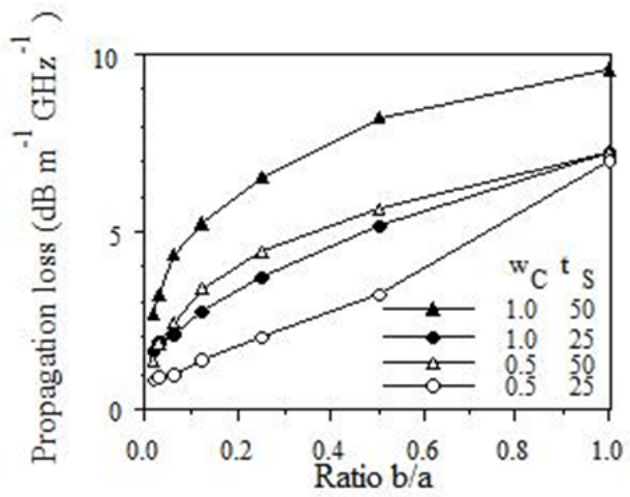


Figure 4.28 Experimental variation of low-frequency propagation loss with ratio *b/a*

4.13 Thin-film Cable Miniaturization

Although the cables described so far have good electrical performance, they are insufficiently flexible. To improve mechanical performance, the amount of copper on the cable must be reduced. Design 3 in **Table 4.5** is chosen as the starting point for improving flexibility as shown below (Design 3.0). Using this, several variants were considered. In the first design (3.1) the thickness of the material of the conductor and patterned ground plane is reduced (from 35.0 to 17.5 μm). In the second (3.2), the width of the ground plane is decreased (from 4.0 to 2.5 mm). In the third (3.3), the periodic ground plane is removed on either side, so that the ground follows a meander path as shown in **Figure 4.29**.

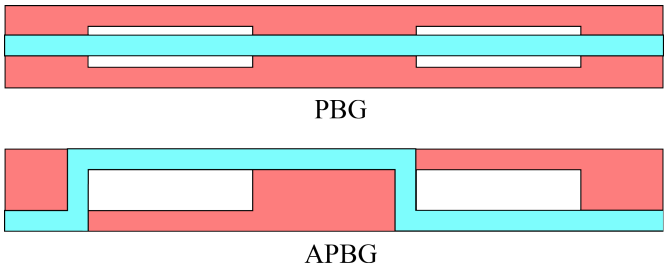


Figure 4.29 Photonic band gap waveguide (PBG) and alternative PBG waveguide (APBG)

Table 4.5 Design variants investigated to improve mechanical performance

Design	Type	W_C (mm)	t_s (µm)	W_G (mm)	W_D (mm)	t_c (µm)	a (mm)	b (mm)
3.0	PBG	0.5	25	4.0	1.5	35.0	16	variable
3.1	PBG	0.5	25	4.0	1.5	17.5	16	variable
3.2	PBG	0.5	25	2.5	1.5	17.5	16	variable
3.3	APBG	0.5	25	2.5	1.5	17.5	16	variable

All the designs in **Table 4.5** were modelled and simulated using AWR Microwave Office. The characteristic impedances at DC were also extracted from S_{11} as shown in Figure 4.30. As can be seen, the characteristic impedances after reducing the thickness and the width of the ground plane are changed very little, while the model with a meandered ground plane has a slightly larger change. This result shows at least some possibility of increasing cable flexibility while retaining impedance matching.

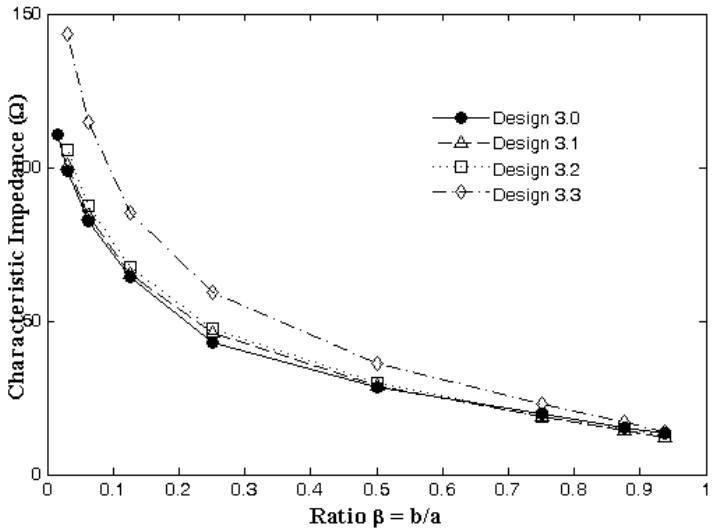


Figure 4.30 Variation of DC impedance with β for designs aimed at improving flexibility

4.14 Whole System Simulation Result

Having studied the electrical characteristics of a wide variety of periodically patterned microstrip, the optimum cable (with β = 1/8, a conductor width = 1 mm and substrate thickness = 25 μm) was connected to the flexible microcoil previously shown in Figure 4.3 for a full system simulation as shown in Figure 4.31a. A simple one-turn inductor loop was also modelled to simulate signal detection via port 2. The resulting frequency variations in S_{11} and S_{21} are shown in Figure 4.31b and Figure 4.31c. The system is correctly resonant and impedance matched at 63.55 MHz, implying that the combined system of a flexible microcoil and a PBG output cable can indeed operate successfully as a receiver for MRI signals.

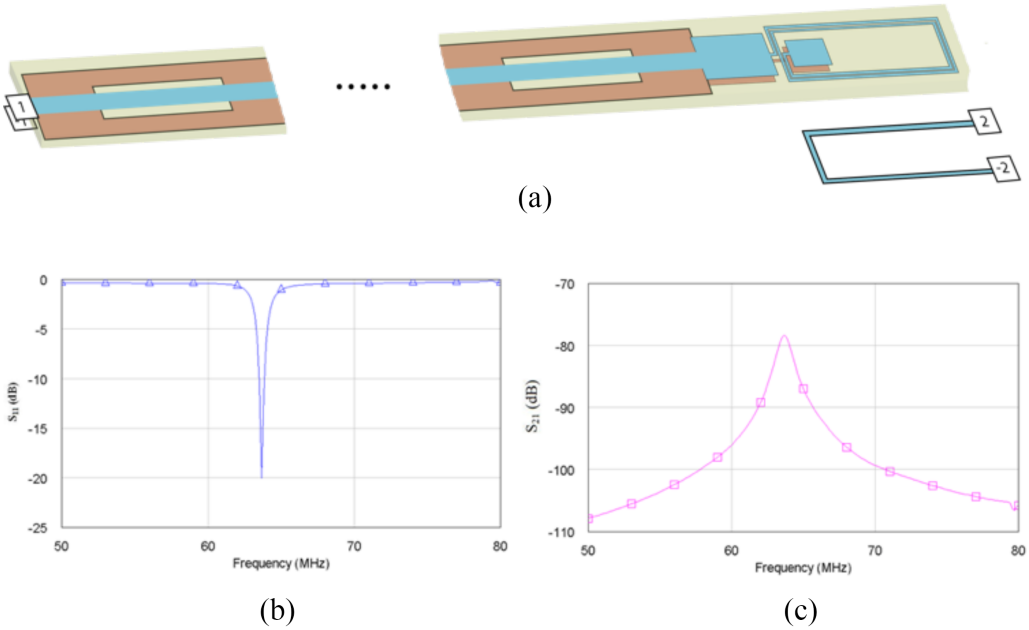


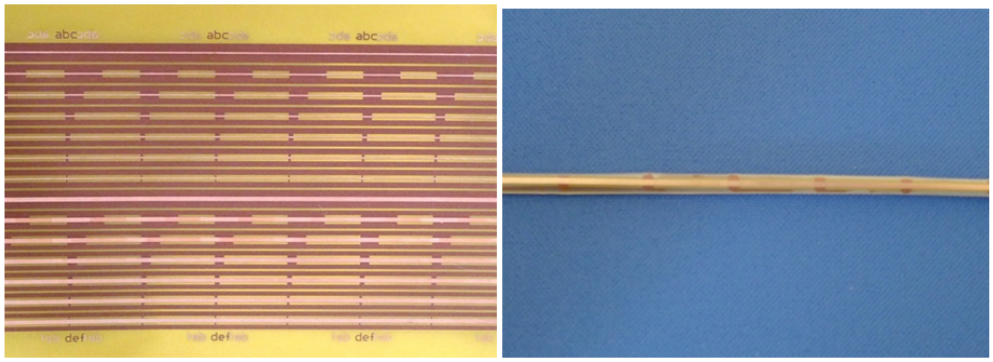
Figure 4.31 Simulated frequency variation of (a) whole system when the cable connected to RF coil (b) S_{11} and (c) S_{21} for a complete thin film receiver

4.15 Discussion

Resonant microcoils and several designs of patterned periodically microstrip cable have been modelled using analytic theory and numerical simulation. The correct resonant frequency can be obtained, and the impedance can be correctly set. There is almost complete agreement between the theoretical data and the simulation data. These results imply that Microwave Office is an appropriate tool for detailed simulations of this type. Prototype cables have also been fabricated and tested. The experimental, theoretical and simulation data are all very similar and agree well with each other. However, the disagreement of propagation losses resulting from the unrealistic loss tangent value was observed. Further experiments to obtain a more realistic value of dielectric loss are therefore required; these will be described later.

4.16 Magnetic Resonance Imaging

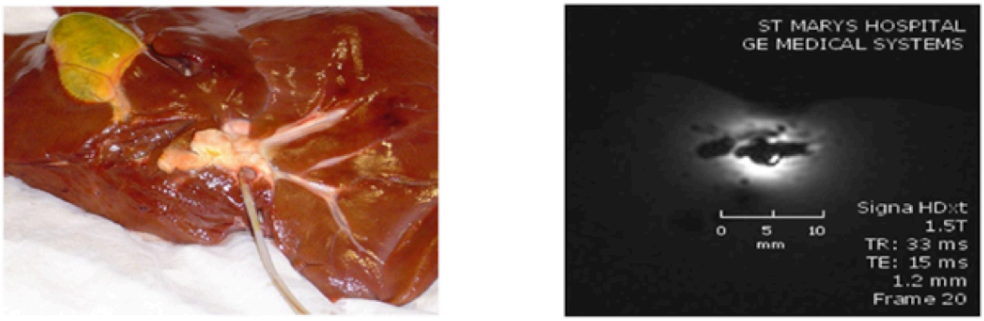
Experimental components were used for ^{1}H MRI, as follows. Completed cable arrays with a stepped variation in periodic loading (Figure 4.32a) were first separated into single lines, then connected to tuned and matched resonant detectors, and finally mounted on catheters using heat shrink tubing by Dr. Munir Ahmad (Figure 4.32b) [45].



(a) (b)

Figure 4.32 (a) Cable array with different periodic loadings, and (b) cable mounted on catheter [45]

A catheter-mounted detector system was then used to image a resected porcine liver as shown in Figure 4.33a, passing the catheter receiver directly into the biliary tree. Magnetic resonance imaging was performed by Prof. Richard Syms and Dr. Marc Rea using a 3D FRFSE (fast recovery, fast spin echo) from a standard 1.5 T GE HD Signa Excite clinical scanner at St. Mary's Hospital, Paddinton, London, with an excitation time (TE) of 15 msec, a repetition time (TR) of 33 msec, and a flip angle of 10°. Figure 4.33b shows an axial image, which is clearly brightest in the immediate vicinity of the microcoil. However, several immediately adjacent ducts may be seen, with a resolution that is clearly sub-mm. This resolution is considerably better than the corresponding performance of the scanner's body own coil and is likely to prove useful in diagnosing cholangiocarcinoma. These results confirm the potential for thin-film receiver systems, a major goal of this work. However, the safety of an output cable based on a long, continuous conductor requires further investigation, as described in the following Chapters.



(a) (b)

Figure 4.33 (a) Resected porcine liver, with the catheter receiver inserted into a duct; (b) ^{1}H MR image of biliary tissue [45]

4.17 Publication

The numerical work from Section 4.4 – 4.10 presented here has resulted in this publication:

"Periodically Structured Thin-film Cables" by R.R.A. Syms, K. Segkhoonthod, I.R. Young, Microwaves, Antennas & Propagation, IET, 2011. **5**(9): p. 1123-1129.

5. MR-Safe Thin-Film Cables

In the previous Chapter, periodically structured thin-film cables were designed to allow impedance matching within the constraints of a thin-film geometry, and low-loss transmission was achieved using a photonic band gap structure. In this chapter, we present an improved flexible cable with the additional feature of inherent MR safety. The design is based on a magneto-inductive waveguide, and uses magnetic coupling between resonant elements based on figure-of-eight shaped loops to reject external B_1 and E fields during the excitation phase of MRI. Once again, analytical and numerical simulation models have been developed, and compared with experimental data.

5.1 RF Heating

The high power of the RF transmitter used in MRI has the potential to cause unwanted RF heating effects in intrabiliary receiver components, which made these potentially unsafe for internal use. There are three main causes of RF heating: eddy currents and induction loops (caused by B_1 fields), and resonating surface waves along metal conductors (caused by E fields). In internal MRI applications, the main problem is heating from surface waves because the other two sources of heating (eddy currents and induction loops) are more easily controlled and typically raise the temperature by only a few degrees Celsius [60, 61]. Resonating surface waves are generated when a long conductive structure couples with the linear electric field produced by an RF transmit coil in the MR scanner. The coupling excites the incident RF wave in and over a wire-like structure resulting in RF standing waves, causing heat production in the wire itself and in the external tissue. Rejection of B_1 and E fields is clearly important for patient safety.

Surface wave heating can occur in linear conductors that are at least half a wavelength in length ($\lambda/2$, where the wavelength is that of the surface wave). The effect has been reported in many linear metallic conductive devices such as guidewires [62-65], pacemakers [66-69], and spinal fusion simulators [70]. When the conductor length is equivalent to half a wavelength, standing RF waves are formed, and the current amplitude can rapidly become large. Although the current is zero at the conductor ends, the electric field is not. Consequently, power can be dissipated in the surrounding tissue, causing rapid heating. The relationship between frequency and wavelength is simply given in the following equation.

$$\lambda = \frac{v_{ph}}{f} \tag{5.1}$$

Where f is the frequency, λ is the wavelength, v_{ph} is the phase velocity of the surface wave. Clearly, the exact value of v_{ph} depends on the surrounding medium, and can generally be expressed as:

$$v_{ph} = \frac{c}{\sqrt{\varepsilon_r \mu_r}} \tag{5.2}$$

Where c is the speed of light in air ($c = \frac{1}{\sqrt{\varepsilon_0 \mu_0}} = 3\text{x}10^8$ m/sec), ε_r is the relative permittivity of the surround, and μ_r is the relative permeability. In fact, the relative permeability of biological tissue is approximately that of vacuum; $\mu_r = 0.999991 \approx 1$, so tissue does not have any noticeable effect on magnetic fields. However, the relative permittivity is significantly different from unity at RF frequency.

RF resonance occurs if the length of the wire approaches $l_d = n\frac{\lambda}{2}, when\ n = 1,2,3,\ldots$ So, we can substitute Equation (5.1) and (5.2) to estimate the first resonant frequency as:

$$f_{1st} \approx \frac{c}{2l_d\sqrt{\varepsilon_r}} \tag{5.3}$$

If we used a linear conductor or wire-like structure such as coaxial cable in vacuum or an open-air environment ($\varepsilon_r \approx 1$), we would find that there is no problematic heating effect at the MR operating frequency (63.8 MHz for ^{1}H MRI imaging) following Equation (5.3) because the critical length defining the onset of heating is quite long (≈ 2.35 m) compared with the human body. In internal MRI applications, because the cable is inserted into tissue, the surrounding environment changes. The dielectric constant (ε_r) increases considerably, so that the length that causes the heating is shortened (≈ 0.268 m, assuming the typical relative dielectric constant of human tissue at RF frequency of 77). This effect has been observed in several experimental studies [63, 71], and a critical resonance length (l_d) of 45 cm and 85 cm has been obtained for a saline solution (9 g NaCl per litre H_2O) used to simulate biological surrounding tissue, and a fluid doped with $CuSO_4$ used to simulate the specific conductivity of a vessel wall respectively.

In 2000, Konings et al demonstrated heating around intravascular guidewires by resonating RF waves experimentally [64]. A nitinol (Nickel-Titanium) endovascular guidewire was partly immersed in a rectangular saline bath in order to simulate the presence of biological tissue in an MRI environment as shown in Figure 5.1a, and the temperature was then measured as shown in Figure 5.1b. Two different methods, liquid crystal paint and a Luxtron 790 fluoroscopic fiberoptic temperature sensor, were used for temperature measurement. The experimental results [64] below showed that the temperature in the guidewire was increased by RF heating at the point of contact to 74 degrees Celsius in 30 seconds with an immersed length of 85 cm during MRI imaging. The result also showed that the same dangerous increase in temperature can occur using wire-shaped medical instruments containing nitinol. Coaxial cable, which contains nitinol and has a linear conductive structure, is therefore determined to be unsafe for internal MRI procedures. Furthermore, it is not only nitinol-containing material that causes the heating [64, 72], but also other metals such as stainless steel, titanium (Ti), and aluminium (Al) are all potentially dangerous [73].

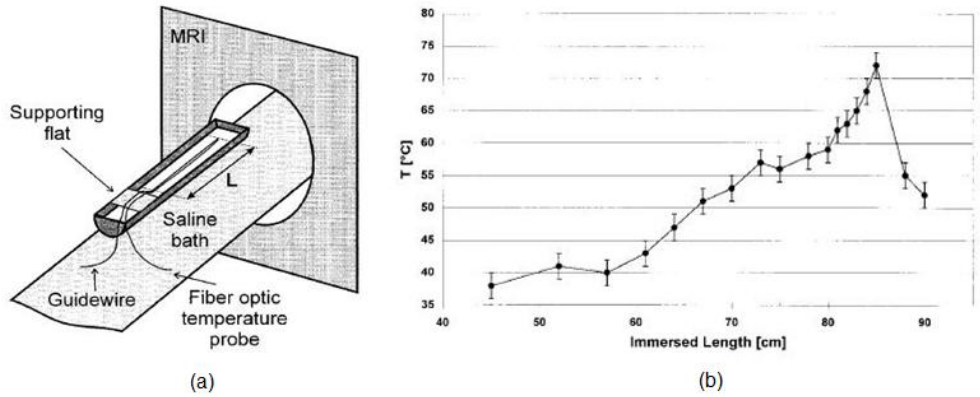


Figure 5.1 (a) experimental set-up for measuring RF heating during MRI showing an oblong bath filled with saline (b) variation of temperature with the immersed length of guidewire [64]

In fact, estimation of the dielectric properties of any tissue surround is difficult because the organs in the human body vary significantly. For example, the relative dielectric constants at 63.8 MHz frequency are 108.08, 112.20, 123.89, and 134.84 for muscle, spleen, liver, and kidney respectively [74, 75]. For the purpose of this study, we decided to use the average of dielectric properties of ordinary human tissue (ε_{r_tissue}) of 77, which yields the small resonant length (l_d) of 27 cm [76-78]. From the literature, it was ascertained that the safe cable can be designed by having a continual linear metallic conductor shorter than the resonant length above to prevent heating effect.

5.2 Safe Transmission Lines

A number of attempts have been made to solve the RF heating problem for the interconnections needed to transfer signals detected using internal imaging probes. One possibility is to use a non-metallic transmission line such as an optical fibre instead of a coaxial cable [79, 80]. Unfortunately, some non-MR compatible components (such as an optical isolator) are required. These cannot be operated under a strong external magnetic field, leading to image degradation. Another solution is to use wireless transmission, such as a wireless implanted MR probe [81] or an RF transponder for wireless reception [82], which

may be inductively coupled to the external receiver. However, the SNR of a wireless transponder is quite poor when used for MRI, due to a lack of phase synchronism with the scanner. As a result, there is a need for MR cables that can combine high SNR with a structure that prevents RF heating. Possible approaches include the insertion of chokes and transformers into coaxial cables, and we now give brief details of each method.

5.2.1 Coaxial Cable with Chokes

In 2000, Ladd and Quick proposed inserting chokes into coaxial cable to reduce RF heating in intravascular catheters [83, 84]. Their approach involved placing chokes at regular intervals of $\lambda/4$, so that there is no continuous length $\lambda/2$ capable of supporting a RF standing wave. Each choke was constructed by soldering a short circuit between the primary and secondary shield of a triaxial cable, and removing the secondary shield every $\lambda/4$, as shown in Figure 5.2. Experimentally, the RF heating was significantly reduced. However, the design introduced another problem. An increase in the external E-field was observed near the opening of the choke, which generated a high voltage that may itself be dangerous during imaging.

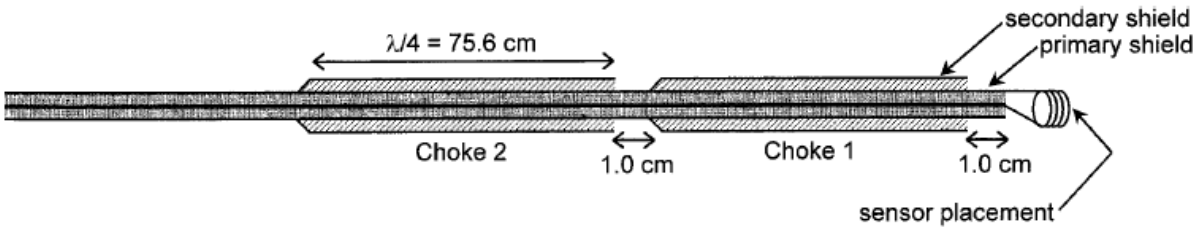


Figure 5.2 A safe transmission line based on periodically inserted chokes [83]

5.2.2 Coaxial Cable with Transformers

Weiss et al. proposed alternative solution to the problem of RF heating, using a set of transformers to subdivide the cable into short sections [85, 86]. The transformer was made on a thin PCB board to meet the space and flexibility requirements of a catheter (1 mm^2 cross section) used for intravascular imaging as shown in Figure 5.3. A significant reduction in RF heating effects was again observed. However, this design also suffered from several limitations. Firstly, the transformers themselves were susceptible to direct coupling to the external transmit (B_1) magnetic field of the scanner. Secondly, coupling between the sections via the stray capacitance of each transformer minimised the effectiveness of the subdivision. Finally, the overall design was relatively bulky, limiting the available space in catheters for other medical electronic components.

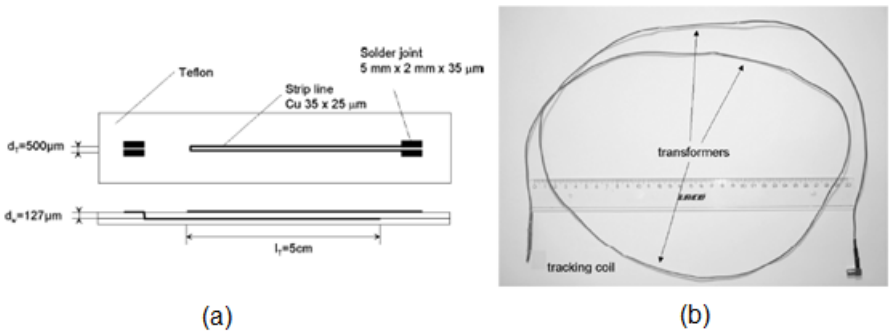
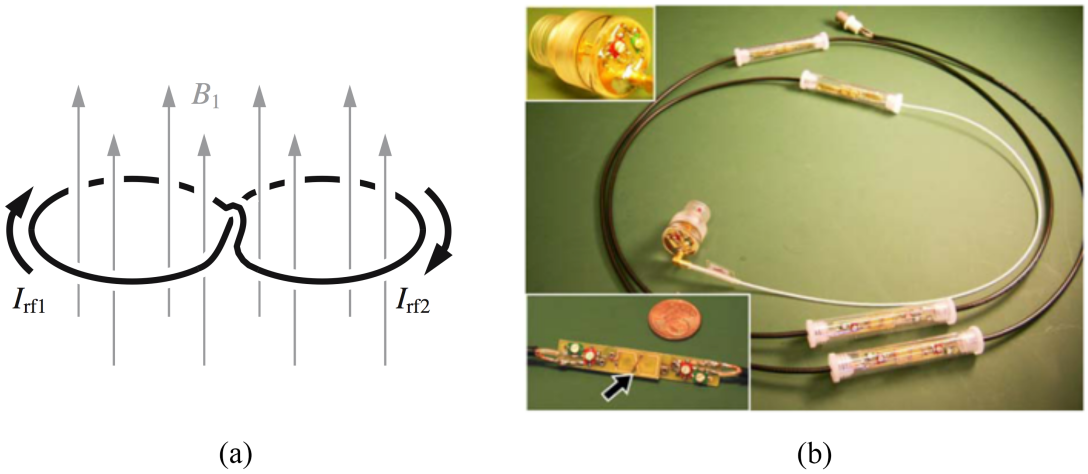


Figure 5.3 (a) layout and (b) realisation of a coaxial cable with transformer subdivision [86]

5.2.3 Coaxial Cable with Figure-of-Eight-Shaped Transformers

As an extension of the previous design, Krafft et al. proposed a transformer with figure-of-eight windings, to avoid direct coupling to the B_1 [87]. The unwanted currents coupled with the B_1 field are called the common-mode currents, and the signals that must be transmitted through the transmission line during an MRI procedure are called the differential-mode

currents. Using this figure of eight-shape transformer, the induced common-mode currents are cancelled as shown in Figure 5.4a, and allow the differential-mode signals to pass through the transmission line. Krafft et al. obtained excellent results showing significantly reduced RF-induced resonant heating. However, because the physical size of the transformer prototype, which was constructed on a standard circuit board measuring 12 mm x 6 mm, the system was extremely bulky when compared to transformers constructed on thin-film PCB as shown in Figure 5.4b. As a result, the concept has proven difficult to integrate into probes for intravascular or intrabiliary MRI.



(a) (b)

Figure 5.4 Figure-eight-shaped transformer (a) B_1 field decoupling in a figure-of-eight shaped coil (b) figure-of-eight shaped coils in a MR-safe transmission line [87]

5.2.4 Magneto-Inductive Cable

We now give background details of magneto-inductive (MI) cables, used as the basis of the alternative safe cable design discussed in this thesis. A MI cable is a waveguide operating by magnetic coupling between periodic resonant elements patterned on a thin-film substrate. This waveguide allows slow wave propagation, and was discovered during theoretical investigation of metamaterials.

The concept of metamaterials was first introduced by Veselago in 1968 [88]. Metamaterials are artificial media, whose properties can be very different from their constituents. For example, they may have negative permittivity ($\varepsilon < 0$) and/or negative permeability ($\mu < 0$), and if both parameters are negative, the material has a negative refractive index ($n = -\sqrt{\varepsilon_r \mu_r}$) [89]. Veselago also introduced a new definition of so-called "Left-Handed" (LH) materials that has been widely used. LH or Double-Negative (DNG) material can be explained using the Poynting vector ($\vec{S} = \vec{E}x\vec{H}$), which is antiparallel to the wave vector ($\vec{k}$) satisfying the left-handed rule. Alternatively, LH medium can be described in terms of the phase velocity (v_p) and the group velocity (v_g); when v_p = -v_g, so the structure supports backward wave propagation.

Metamaterials were first implemented using split ring resonators (SRRs) (which can have negative permeability), or SRRs with additional wires (which can have negative permittivity) [90, 91]. As expected, the latter type demonstrated the key property of negative refractive index. Subsequently, metamaterials have been used in many fields, for example, for imaging devices [92, 93], interconnects [94-96], invisibility cloaks [97-100], or even new applications at higher frequencies (THz) [101]. Of particular relevance here, Wiltshire et al. showed that so-called 'Swiss-roll' metamaterials can be used to guide RF flux from the signal source to a receiver coil during MR imaging [102]. This result demonstrated the application of metamaterials to MRI, and has paved the way for considerable further research.

The magneto-inductive waveguide was first proposed by Shamonina et al. [103]. Further theory, and the possibility of forming magneto-inductive waveguides in 2D and 3D, were then presented in [104]. She also gave a new definition of magneto-inductive waveguides as "*magnetic metamaterials*" [105]. The MI waveguide was experimentally confirmed by Wiltshire et al., who showed that the MI can exist as forward and backward waves depending on the arrangement of a set of capacitively loaded loops [106]: an axial arrangement supports forward waves while a planar arrangement supports backward wave. Other aspects of magneto-inductive waves were also investigated: for example, the dispersion characteristic of MI waves [106], refraction index of MI waves [107], and an interaction between EM and MI

waves based on periodic transmission lines [108]. The equivalent circuit consists of a set of L-C resonators (with additional series resistances *R*) linked together by mutual inductance *M* as shown in Figure 5.5. Depending on the arrangement, *M* may be positive or negative.

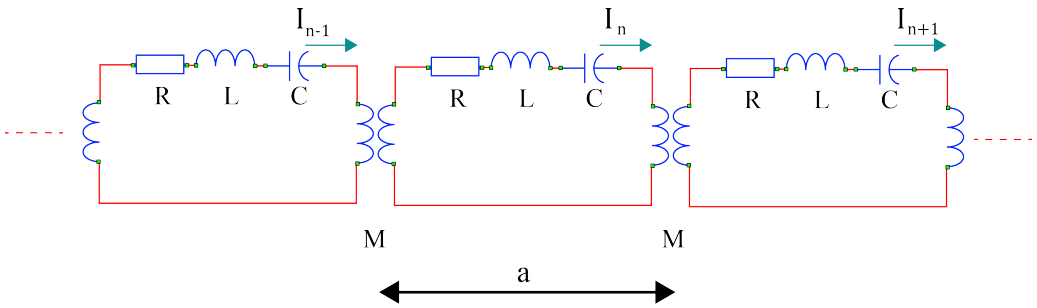


Figure 5.5 Equivalent circuit of a magneto-inductive waveguide

Kirchhoff's laws can be used to analyse the equivalent circuit in Figure 5.5. Assuming nearest-neighbour coupling only, a recurrence relation can be obtained between the currents I_{n-1}, I_n and I_{n+1} in the n-1th, n^{th} and n+1th section, in the form:

$$\left\{j\omega L + \frac{1}{j\omega C} + R\right\} I_n + j\omega M\{I_{n-1} + I_{n+1}\} = 0 \qquad (5.4)$$

For an infinite waveguide, we can assume a travelling wave solution $I_n = I_0 exp(-jnka)$ for the current, where *ka* is the phase shift per element, *k* is the propagation constant and *a* is the element length. Substitution and cancellation of exponential terms allows the dispersion relation equation to be obtained as:

$$\left\{1 - \frac{\omega_0^2}{\omega^2} - \frac{j}{Q}\right\} + \kappa \cos(ka) = 0 \qquad (5.5)$$

Where $\omega_0 = 2\pi f_0 = \frac{1}{\sqrt{LC}}$ is the angular resonant frequency, $Q = \frac{\omega L}{R}$ is the Q-factor, and $\kappa = \frac{2M}{L}$ is the coupling coefficient. Generally the propagation constant is complex and hence can be written in the form $k = k' - jk''$. The dispersion equation can then be separated into real and imaginary parts. If losses are very small (i.e. if Q is high enough), separate relations can be obtained for the real and imaginary parts, as

$$\left\{1 - \frac{\omega_0^2}{\omega^2}\right\} + \kappa\cos(k'a) = 0 \tag{5.6}$$

$$k''a = 1/\{\kappa Q sin(k'a)\} \tag{5.7}$$

The dispersion relation for the phase change per element waves in Equation (5.**6**) is relatively unaffected by loss, and as a result can generally be used to estimate the frequency band which magneto-inductive waves may propagate, as:

$$\frac{1}{1+|\kappa|} \leq \frac{\omega^2}{\omega_0^2} \leq \frac{1}{1-|\kappa|} \tag{5.8}$$

Using Equations (5.6), we can plot the dispersion relation for capacitively loaded ring in the axial (Figure 5.6a) and planar (Figure 5.6b) arrangements, as shown in Figure 5.7a and Figure 5.7b, respectively. Here we have assumed a coupling coefficient of 0.1. In the axial arrangement, *M* is positive. This leads to a dispersion diagram with positive group velocity d*w*/d*k*, so forward waves are supported. In the planar arrangement, *M* is negative due to the different coupling between the elements, so the dispersion diagram has negative group velocity and backward waves are supported. For infinite waveguides, the dispersion characteristic is continuous, and is represented as a dashed line (--). However, for a finite line containing *N* elements, periodic boundary conditions must be satisfied, and the possible values of *ka* are then restricted to the discrete values *ka* = *np*/(*N*+1), where *n* is an integer. *N* is usually odd number to achieve a resonance at the mid band). In Figure 5.7, results are also presented for a typical finite case of *N* = 9 as a set of stars (*).

Many applications have been developed for MI waves. These include delay lines [109], filter [109], near-field imaging devices [110], phase shifters [111], and waveguides [103, 112, 113]. Although MI waveguides only allow narrow band operation, this restriction is unimportant in MRI applications, which only require narrow band of frequencies around the Larmor frequency to transfer a complete stack of slice images.

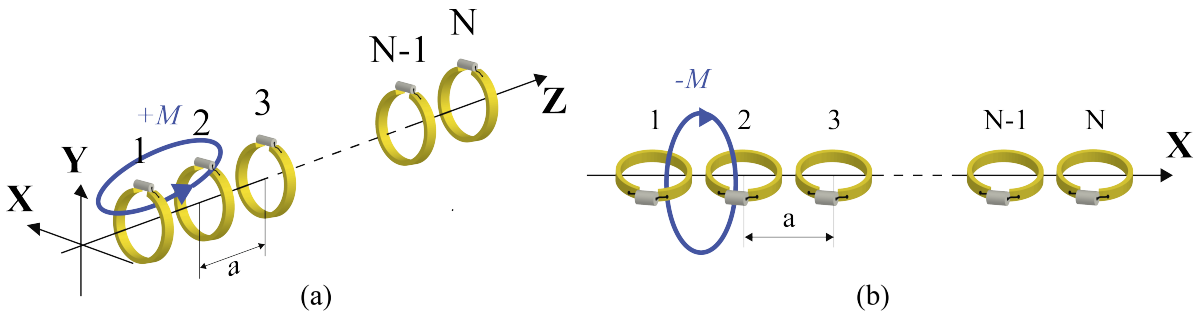


Figure 5.6 MI waveguides in (a) axial and (b) planar configurations [112]

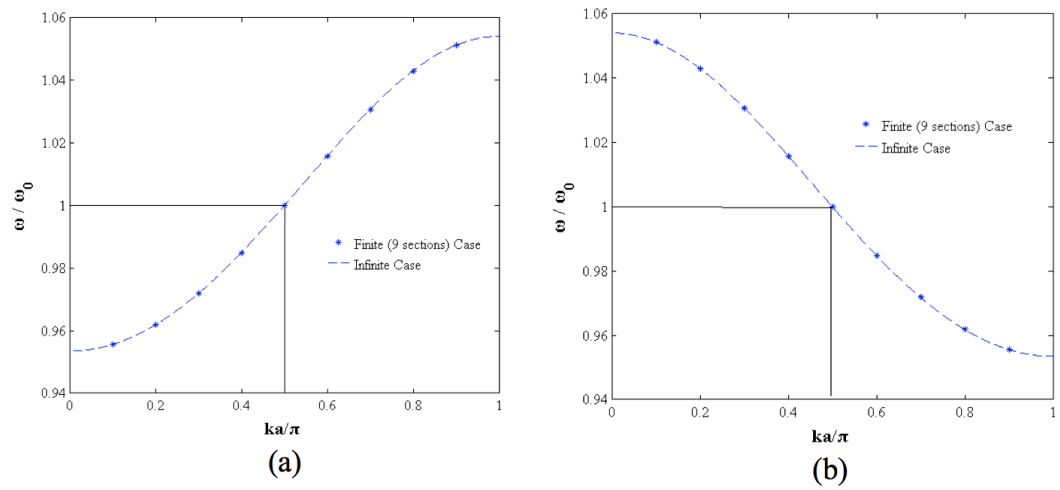


Figure 5.7 Dispersion relations of (a) axial arrangement supporting forward wave propagation, and (b) planar configuration supporting backward waves

Studies carried out in the Optical and Semiconductor Devices Group of the EEE Dept. at Imperial College have already shown that flexible MI cables can provide low loss propagation with high Q-factor [114], strong couple without non-nearest neighbour effects

[115], and an ability to bend without changing a mutual inductance [116]. Significant effort has therefore been invested in development of magneto-inductive cables for MRI signal detection [117, 118]. Particularly, the inherent segmentation of a MI waveguide has been exploited to create a new type of safe cable for internal magnetic resonance imaging [119]. In this unique design, single turn inductors with integrated capacitors were fabricated on a polyimide thin film as a periodic array, using the two-layer design shown in Figure 5.8 below.

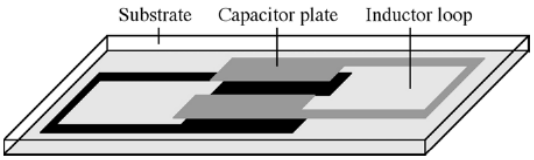


Figure 5.8 3D model of a single resonant element of magneto-inductive cable developed at Imperial College [119]

Using this design, heating by the electric field in an MRI scanner can be avoided. However, some difficulties remain. Firstly, the resonators consist of simple loops that can couple directly to the magnetic field. Secondly, development has proceeded by a combination of simple lumped element analysis and experimental trial and error. As a result, properties such as operating frequency and characteristic impedance have so far been difficult to control. These aspects highlight the need for a more thorough design analysis, a main topic of this thesis.

5.3 Second Generation MR-Safe Thin-Film Cable

Following this previous research, three main problems can be summarised for second-generation cable, as follows:

1. The resonant elements must be decoupled from the B_1 field of the transmitter,
2. The overall system must meet all electrical constraints (operation at the MR frequency, e.g. 63.8 MHz for ^{1}H imaging at 1.5 T, low transmission loss, and matching to 50 Ω impedance),
3. The overall system must meet all mechanical constraints (sufficient flexibility to wrap around a catheter, stability against bending, and a suitable form factor to pass the biopsy channel of a side-opening gastroscope as used in ERCP).

Particularly, the cable must satisfy the dimensional constraints of the supporting catheter (obtained from Wilson-Cook Medical Inc), which has 0.715 mm inner radius and 1.125 mm outer radius. Since the cable is wrapped over the catheter, the available circuit width can be estimated as $2\pi r_{\text{outer}}$ = 7.07 mm. A suitable circuit layout can then be developed by combining the earlier magneto-inductive cable [119] and the figure-of-eight-shaped transformer in [87] as shown in Figure 5.9. The inductors are single-turn loops, twisted into a figure-of-eight shape, and the strip capacitors are long and narrow and placed outside the inductors to allow mechanical trimming to tune the operating frequency. This layout will still support a travelling magneto-inductive wave, while minimising coupling to the B_1 field. There is little freedom to choose most of the parameters in the cable. For example, the overall width (W) of the cable must clearly be less than the value given above, and was chosen as 6.75 mm. The lengths of inductor (D_L) and capacitor (D_C) must not exceed the estimated critical length (~ 27 mm) found previously, and was chosen as D_L = 196.5 mm. Other physical parameters are W = 6.75 mm (chosen not exceed the circumferential space in the chosen catheter, 7.07 mm), W_L = 4.00 mm, T_L = 0.50 mm, T_C = 0.75 mm, G_L = 0.50 mm, G_{C1} = 0.875 mm, G_{C2} = 0.375 mm. The capacitor length (D_C) of the cable given in Table 5.1 was then varied from 49.25 mm to 99.25 mm to allow the correct operating frequency to be achieved.

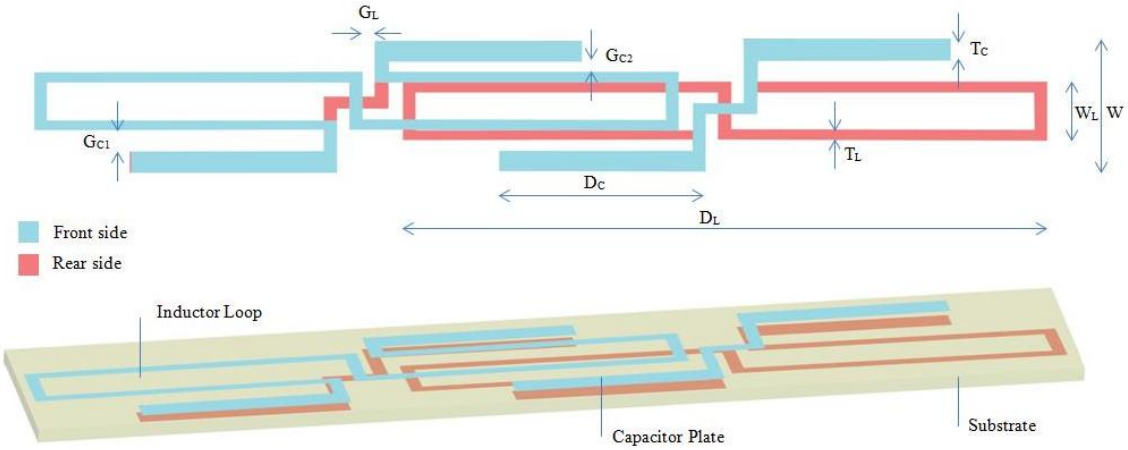


Figure 5.9 Layout parameters and 3D structure of second-generation MR-safe cable

Table 5.1 Capacitor length of second-generation MI cable variants

Type	D_C (mm)
A	99.25
B	89.25
C	79.25
D	69.25
E	59.25
F	49.25

5.4 MR-Safe Thin-Film Cable Simulation Results

Designs of the type presented above were simulated as follows. A single resonant element of each type with the dimensional parameters in Table 5.1 was first modelled using AWR MWO, with the defined layers shown in section 4.3. The dielectric constant of polyimide was taken as 3.4, and the conductivity of the conducting material as that of bulk copper (5.69×10^7 S/m). However, following the poor loss estimation of photonic thin-film cable in in section 4.11 caused by the inaccurate value of *tan δ* for Kapton given in the manufacturer's data sheet [120], a more accurate value is clearly required. A suitable value

was obtained by experiment. An L-C resonator was first constructed using a Kapton-based capacitor and an inductor made of large diameter wire (so that the dielectric losses were dominant). The resonator was then tuned to 63.8 MHz. The Q-factor was then measured, as described in Appendix A, and this value was used to extract the dielectric loss at RF frequency. In this way, the loss tangent of Kapton was estimated as 0.006, considerably higher than the manufacturer's value. This value was used in an AWR simulation, as we now describe.

Simple transducers based on a rectangular wire loop were placed on either side of the resonant element for input and output coupling as shown in Figure 5.10. The transducers were connected to ports with 50 Ohm impedance, with Port 1 acting as a signal source and Port 2 as a load. The frequency variation of the scattering parameters including the reflection coefficient (S_{11}) and transmission coefficient (S_{21}) were then obtained as shown in Figure 5.11. Here, results labelled A, B … F are presented for the different cable variants in Table 5.1. In each case, there is a large peak in S_{21} and a trough in S_{11}, corresponding to the L-C resonance. However, the reflection is very high because the arrangement of this simulation is simply to determine the operating frequency of each element of MR thin-film cable. As can be seen, the required operating frequency of 63.8 MHz can be achieved with a capacitor length between that of variants E and F.

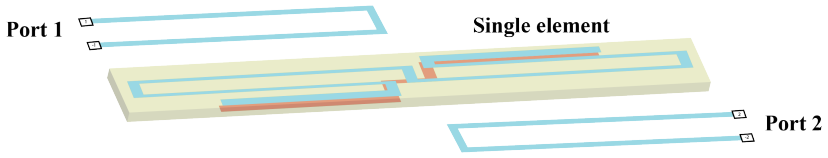
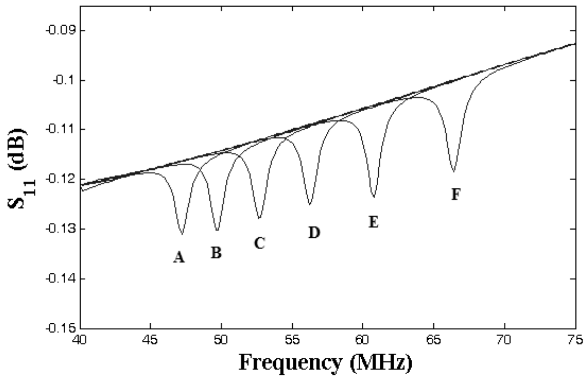
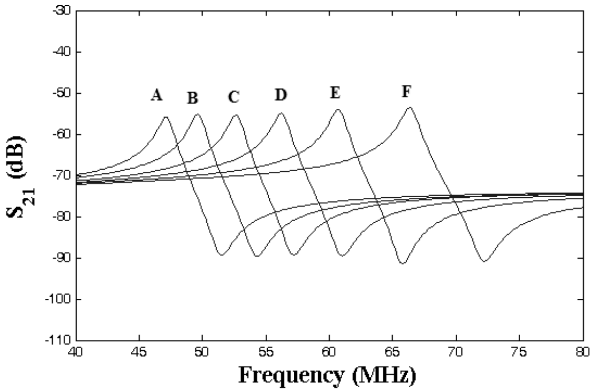


Figure 5.10 Single element of MI thin-film cable modelled by AWR MWO



(a)



(b)

Figure 5.11 Numerical frequency variation of scattering parameters of a single element obtains using MWO; (a) reflection coefficient – S_{11} and (b) transmission coefficient – S_{21}

To investigate the other electrical parameters, a pair of coupled resonant elements was modelled as shown in Figure 5.12, again using simple inductive loops for input and output coupling. This coupled resonator system has two resonant frequencies (f_1 and f_2), which can be seen in the frequency variations of S_{11} and S_{21} shown in Figure 5.13a and Figure 5.13b. The transmission is so low due to the arrangement of the model, which is being used simply to determine the coupling coefficient between two resonant elements in the cable. Once again, results are presented for all the different cable variants in Table 5.1.

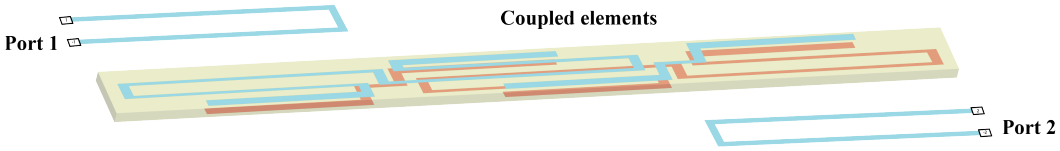
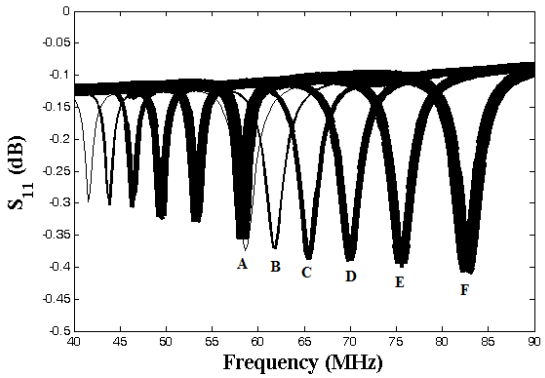
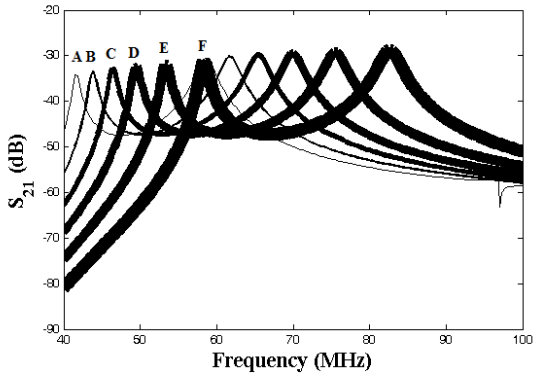


Figure 5.12 Coupled resonant elements modelled by AWR MWO



(a)



(b)

Figure 5.13 Numerical frequency variation of scattering parameters of coupled resonant elements obtained using MWO; (a) reflection coefficient – S_{11} and (b) transmission coefficient – S_{21}

Using the three observed resonant frequencies f_0, f_1 and f_2, the electrical parameters of the magneto-inductive cable can be extracted as follows. Capacitance (C) is the first and easiest parameter to be found. The long, thin capacitors of each model can to good approximation be

considered as parallel plate structures. Their capacitance can therefore be estimated from the standard formula:

$$C = \varepsilon_r \varepsilon_0 \frac{A}{d} \tag{5.9}$$

Here ε_r is the relative permittivity of the polyimide interlayer, ε_0 is the dielectric constant of free space ($\approx 8.854 \times 10^{-12}\ F\ m^{-1}$), A is the area of overlap of the two plates, and d is the polyimide thickness.

Using the estimated value of C and the resonant frequency f_0 obtained from the numerical simulation of single resonant elements, the inductances (L) of each variant can be extracted from the standard equation $\omega_0 = 2\pi f_0 = \frac{1}{\sqrt{LC}}$. The coupling coefficient (κ) can then be calculated from the paired resonances $f_1 = \frac{1}{2\pi\sqrt{(L+M)C}}$ and $f_2 = \frac{1}{2\pi\sqrt{(L-M)C}}$ observed in the simulation of coupled-element models using the standard equation [114]:

$$\kappa = \frac{2\left(\frac{f_2^2}{f_1^2} - 1\right)}{\left(\frac{f_2^2}{f_1^2} + 1\right)} \tag{5.10}$$

Subsequently, the mutual inductance (M) can be calculated using from the relation $\kappa = \frac{2M}{L}$, [119], and the mid band impedance (Z_{0M}) of the line can be estimated as:

$$Z_{0M} = \omega_0 M \tag{5.11}$$

The electrical parameters extracted using the equations above are shown in Table 5.2 below. As can be seen, none of these cables achieves the required impedance of 50 Ω (so that $Z_{0M} \neq$

Z_0). To improve impedance matching, the inductance of the cable should ideally be increased. Unfortunately, an increase in L requires either an increase in the length or number of turns of the inductor. The first approach is in conflict with the need for electrically short elements, while the second introduces considerable layout complexity. An alternative solution based on a narrow-band matching transformer was therefore developed. The transformer design will be described in later section.

Table 5.2 Extracted data for the different types of resonant element

Type	f_0 (MHz)	f_1 (MHz)	f_2 (MHz)	C (pF)	L (nH)	κ	M (nH)	Z_{0M} (Ω)
A	47.20	41.55	58.70	44.82	253.69	0.6648	84.33	25.01
B	49.60	43.90	61.90	40.30	255.48	0.6614	84.48	26.33
C	52.60	46.30	65.60	35.79	255.83	0.6700	85.70	28.32
D	56.20	49.30	70.00	31.27	256.47	0.6738	86.40	30.51
E	60.60	53.50	75.70	22.24	310.15	0.6676	103.53	39.24
F	66.40	58.30	82.60	17.72	324.15	0.6699	108.58	45.30

5.5 MR-Safe Cable Experimental Verification

The different variants (A-F) of MR-safe cable were fabricated in copper-clad Kapton by Clarydon as shown in Figure 5.14. Each cable has 15 figure-of-eight elements (giving a total length of 1.6 metres). The experimental PCB contained an array of cables, which were separated into individual cables using a scalpel. Initial electrical assessment was carried out with the cables flat, and further tests were carried out with the cables mounted on appropriate catheter supports.

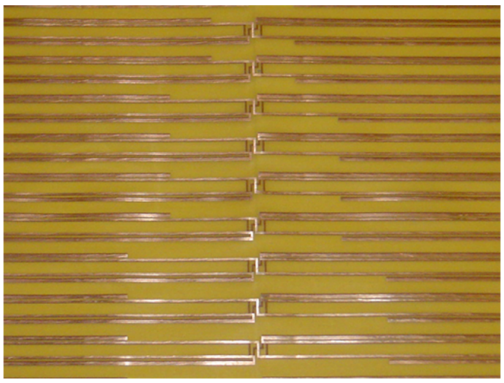


Figure 5.14 Array of MR-safe cables fabricated by the UK Company Clarydon

The frequency variation of the scattering parameters was first measured for each design with an Agilent electronic network analyser, using a weak inductive tap for signal injection and detection. The results are as shown in Figure 5.15. In each case, propagation is clearly obtained over a limited frequency band. Due to the relatively poor matching, the peak transmission is only -20 dB. More importantly, there is some discrepancy between the experimental results and the previous simulation using AWR MWO. Particularly the extracted numerical value of κ (~0.67) from the simulations is lower than the measured experimental value (~ 0.75), while the predicted numerical value of Q (>50) is higher than the experimental value (~ 40).

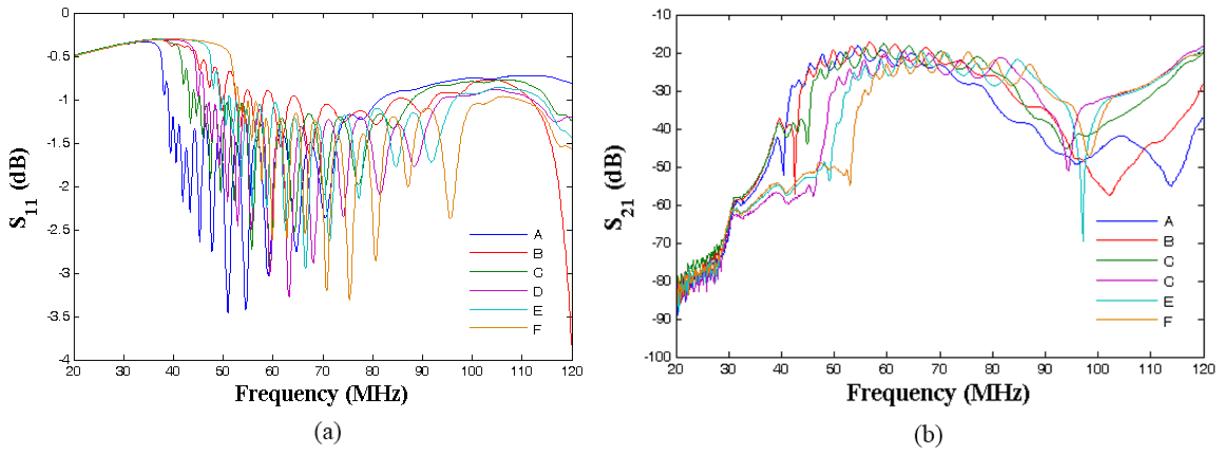


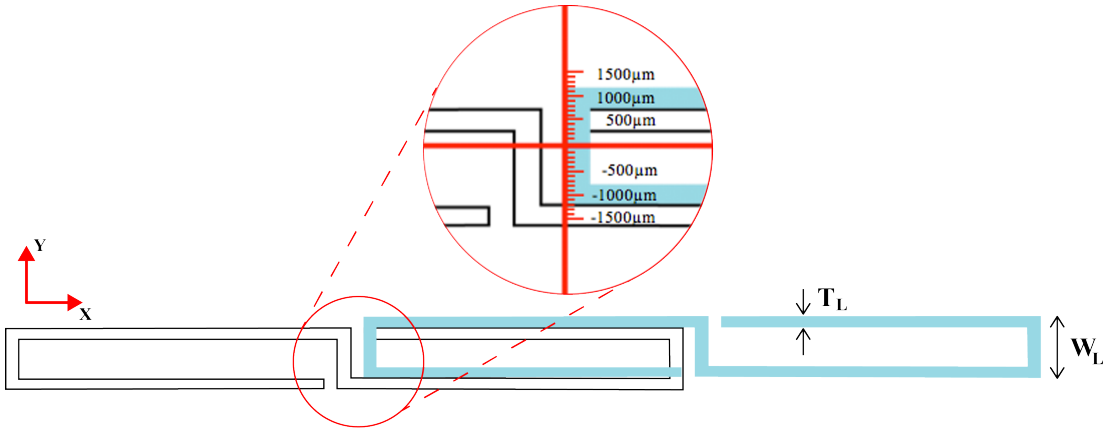
Figure 5.15 Experimental frequency variation of scattering parameters of different thin-film cables; (a) reflection coefficient – S_{11} (b) transmission coefficient – S_{21}

5.6 MR-Safe Thin-Film Cable Simulation Correction

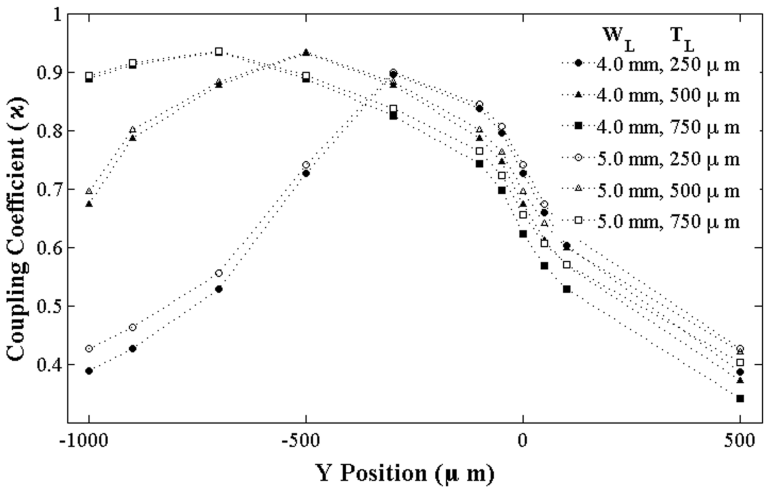
Due to the disagreements in electrical properties described above, further work was carried out to improve the realism of the numerical model by minor changes to the geometry of the resonant elements. There are several methods to increase κ. One possibility is to increase the width of inductor (W_L), another is to overlap the conductors of adjacent sections, and a final possibility is to alter the width of the conductor track (T_L).

The effect of changing W_L and T_L was modelled using the freeware FastHenry, developed by Massachusetts Institute of Technology (MIT), which can find the inductance matrix of a general coupled multi-element inductor system. Figure 5.16a shows a typical FastHenry model of a pair of figure-of-eight shaped inductors in the X-Y plane. The overall width W_L and track width T_L can clearly both be altered to simulate changes in layout parameters. Furthermore, the Y-position of the right-hand side inductor can be altered to simulate variations in conductor overlap. In each case, the values of L and M can be extracted, and the corresponding value of κ can then be found.

Figure 5.16b shows the results, plotted as a function of the Y-position of the right-hand side inductor, for different values W_L of and T_L. As can be seen, the coupling coefficient κ increases when T_L reduces and when W_L increases. The coupling coefficient also increases extremely rapidly when the Y-offset is negative, i.e. when the conductors of the two adjacent elements start to overlap. The coupling coefficients are maximum when the positions of the right hand side inductor are at -300, -500, and -700 μm for the models with T_L = 250, 500, and 700 μm, respectively.



(a)



(b)

Figure 5.16 FastHenry simulation of coupled element system (a) two-inductor model (b) variation of κ with W_L, T_L, and the offset of the right hand side inductor

Increasing κ by overlapping conductors may lead to an increase in the parasitic capacitance between elements, an additional effect that will be described later. To avoid such effects, a second experiment was designed. The layout in Figure 5.12 was simulated using AWR Microwave Office once again, fixing the conductor track width (T_L) at 500 µm and varying the overall width of the inductor (W_L) between 4 and 6.5 mm. In this case, the variation κ of with W_L shown in Figure 5.17 was obtained. These results show that a coupling coefficient of 0.684 can be achieved when W_L = 5.0 mm. Although this value is still somewhat less than the experimental result, it is now achieved using a realistic design.

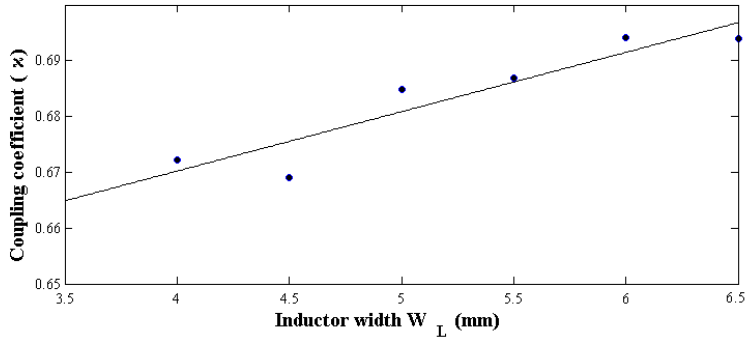


Figure 5.17 Variation of coupling coefficient κ with inductor width W_L obtained using AWR MWO

The alteration of the inductor width (W_L) results in a change in the inductance (L) and the corresponding resonant frequency (f_0). Therefore, the new models (A-F) were simulated once again using the new value of W_L = 5.0 mm, and tuned to the operating frequency of 63.8 MHz by changing the capacitor length (D_C). Figure 5.18 shows the variation of f_0 with capacitor lengths for the two different inductor widths. As can be seen, the resonant frequencies of the new models are all lower than those of the old models because of the increased inductance associated with a larger value of W_L.

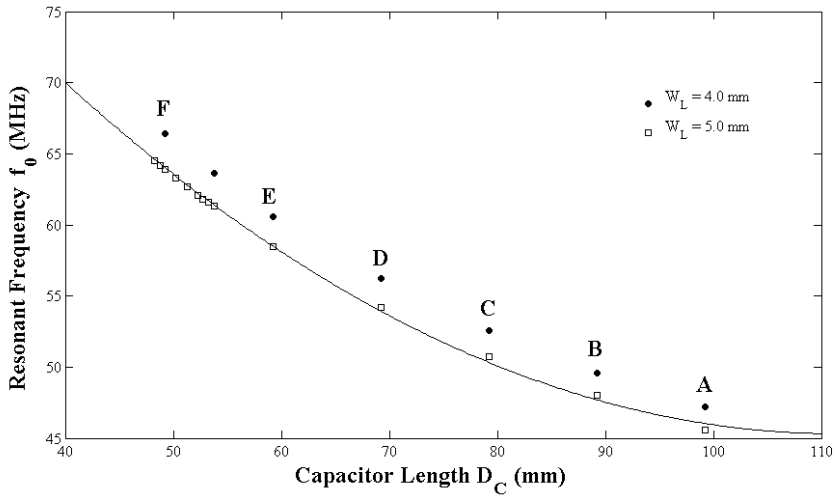


Figure 5.18 Variation of resonant frequency f_0 with capacitor length D_C

Another electrical parameter that required attention is the quality factor (Q_0). Previous simulations found that Q_0 is over 50 while the corresponding experimental value is approximately 40. This implies that the dielectric loss of the dielectric substrate is too low, or the conductivity of the metal tracks is too high. Previously, we have shown the need to correct the *tan δ* of polyimide. We now consider the additional correction of conductivity. In previous simulations, the conductivity of a bulk copper (~5.96e+007 S/m) was used, but literature studies [121, 122] show that the conductivity of a thin-film conductor is typically reduced by additional grain boundaries. This issue was again clarified by simulation, using a single resonant element whose Q factor was found as a function of the copper conductivity. Figure 5.19 below shows the extracted variation. It was found that the conductivity giving the most realistic Q-factor is 2.96 e+007 S/m.

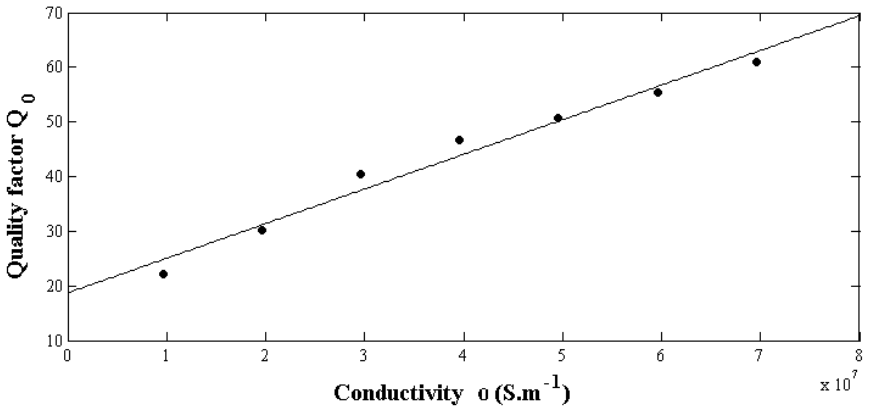


Figure 5.19 Variation of Q-factor Q_0 with conductivity $\boldsymbol{\sigma}$

The dimensional and electrical parameters obtained using the old and new models are summarised in Table 5.3 and Table 5.4. Although there is still not 100% correspondence with the experimental data, the modified design does provide reasonable agreement from a realistic layout.

Table 5.3 Dimensional parameters of the old and new models used in the simulations

Parameter	W (mm)	W_L (mm)	T_L (mm)	D_L (mm)	D_C (mm)	G_{C1} (mm)	G_{C2} (mm)	G_L (mm)
Improved value	7.75	5.00	0.50	196.50	49.25	0.875	0.375	0.50
Previous value	6.75	4.00	0.50	196.50	43.75	0.875	0.375	0.50

Table 5.4 Corresponding electrical parameters obtained from the designs in **Table 5.3**

Parameter	σ (S/m)	$tan\ \delta$	f_0 (MHz)	C (pF)	L (nH)	κ	M (nH)	Z_{0M} (Ω)	Q_0
Improved value	2.96e007	0.006	63.90	22.24	278.94	0.684	95.52	38.35	40.96
Previous value	5.69e007	0.006	63.60	19.76	316.98	0.672	106.53	42.57	55.64

5.7 Overall Receiver Design

In this section, the finite MI cable system shown in Figure 5.20 is studied, with the aim of clarifying the designs of the resonant detector and the coupling transducer needed to connect to a conventional RF system. As can be seen, each resonant element in the cable is magnetically coupled its neighbours by a mutual inductance M. The detector is a further resonant element with slightly different resistance, inductance and capacitance R_D, L_D and C_D, and is coupled to the cable via a mutual inductance M_D. The transducer (or tap) is also a resonant element, again with different resistance, inductance and capacitance R_R, L_R and C_R which is connected directly to the scanner input, and coupled to the cable via mutual inductance M_R. All components must be tuned to the MR operating frequency of 63.8 MHz.

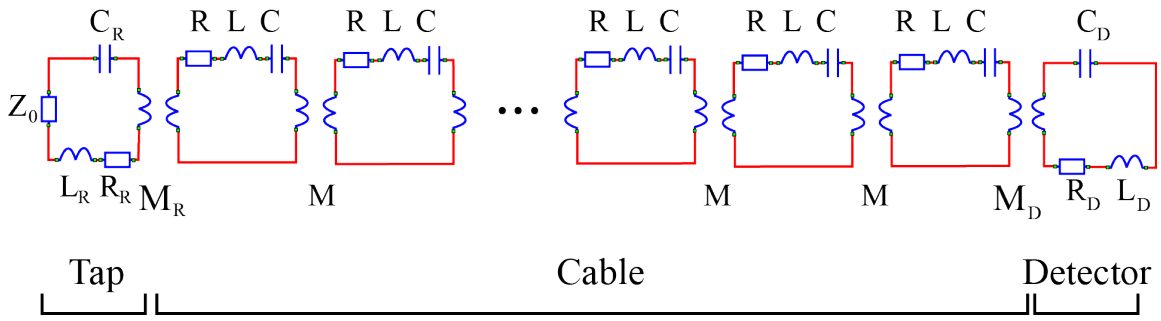


Figure 5.20 Complete receiver , with resonant detector, MR-safe cable and coupling transducer

We begin by considering impedance matching. In previous studies [119, 123], the characteristic impedance of the MI waveguide was found as:

$$Z_0 = j\omega M e^{-jka} \tag{5.12}$$

At the resonant frequency $\omega = \omega_0$ and $ka = \frac{\pi}{2}$, and Z_0 simply reduces to the real value:

$$Z_{0M} = \omega_0 M \tag{5.13}$$

We now consider the lumped element circuit in Figure 5.20 at the detector end. Using Kirchhoff's law it is simple to show that there will be no reflection at the detector if the mid-band impedance is matched to the detector. In this case:

$$Z_{0M} = \frac{\omega^2 M_D^2}{\left\{R_D + j\omega L_D - \frac{1}{j\omega C_D}\right\}} \tag{5.14}$$

If L_D and C_D also resonate properly, the matching Equation (5.14) reduces to:

$$Z_{0M} = \frac{\omega^2 M_D^2}{R_D} \tag{5.15}$$

Equation (5.15) implies that the MI cable can be matched to an arbitrary value of the load resistance R_D, merely by choosing the mutual inductance at the detector end to satisfy.

$$\omega_0 M_D = \sqrt{Z_{0M} R_D} \tag{5.16}$$

We now repeat the matching process at the transducer, whose function is to match the MI cable to the system input impedance Z_0. In this case, we obtain the alternative matching condition:

$$\omega_0 M_R = \sqrt{Z_{0M} Z_0} \tag{5.17}$$

Consequently, the mutual inductance M_R may be used to match the magneto-inductive cable to arbitrary input impedance. Note that the matching achieved is essentially narrow-band. Broadband matching may be used if $Z_{0M} = Z_0$, by choosing in addition $L_D = L_R = L/2$, and $C_D = C_R = 2C$ [124]. However, the results above show that narrow-band matching may be achieved even if $Z_{0M} \neq Z_0$.

From previous sections, we know $Z_{0M} < Z_0$ (Z_{0M} =38.35 Ω), so the tap must have a larger mutual inductance than the line. Consequently, the tap inductor should be multi-turn. Also, from Equation (5.**16**), it can be shown that $\omega_0 M_D < \omega_0 M$ so that the overlap area between an arbitrary detector and the final cable element must be relatively small. This assumption is proved using MWO in the next section.

5.8 Lumped Element Demonstration of Matching

To verify the matching strategy, the design principles of the previous section were combined with the extracted electrical parameters of the MR-safe cable in Table 5.4 in an AWR simulation of a complete receiver system. In this case, the in-built circuit simulator was used, rather than the AXIEM electromagnetic solver. First, it was verified that element parameters of L = 278.94 nH, C = 22.24 pF, R = 2.79 Ω, M = 95.53 nH and κ = 0.684 gave the correct bandwidth for the cable. Matching all the components was then achieved step by step, using a 9-section cable.

The first step was to match the tap and the cable without the resonant detector, using the modified system shown in Figure 5.21. Here, the lack of a suitable termination at the right hand end means that strong reflections should arise at this point. If, in addition, the left-hand end is not properly matched, reflections should arise at the left hand end. The overall structure should therefore be resonant. Conversely, if matching can be achieved at the left-hand end, the resonance should disappear.

Transducer matching was verified first, as follows. A two-turn inductor with a length and breadth similar to that of a halved cable element was first simulated using FastHenry, and its inductance (L_R) was estimated as 460 nH. Using this value, the capacitance (C_R) needed for resonance at 63.85 MHz was estimated as 13.48 pF. An AWR layout giving these parameters was then defined, and connected to Port 1 (which has impedance Z_0 = 50 Ω).

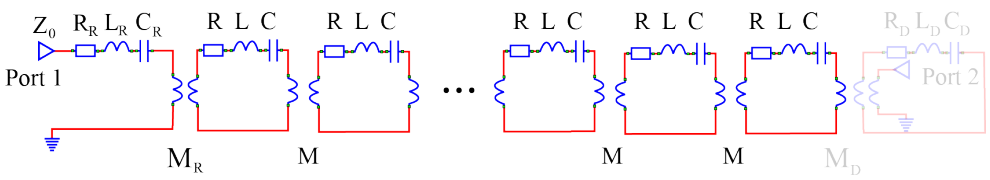


Figure 5.21 Circuit arrangement during matching of the transducer

The mutual inductance (M_R) between the tap and cable was first adjusted to couple the tap weakly to the line. The frequency variation of the reflected power S_{11} was obtained, and nine resonances were observed (with the central resonance at 63.9 MHz) as shown in Figure 5.22a. M_R was then gradually increased, by increasing the physical overlap between the tap and the first cable element, until the central resonance largely disappeared as shown in Figure 5.22b below. At this point, the transducer is in the correct position for matching.

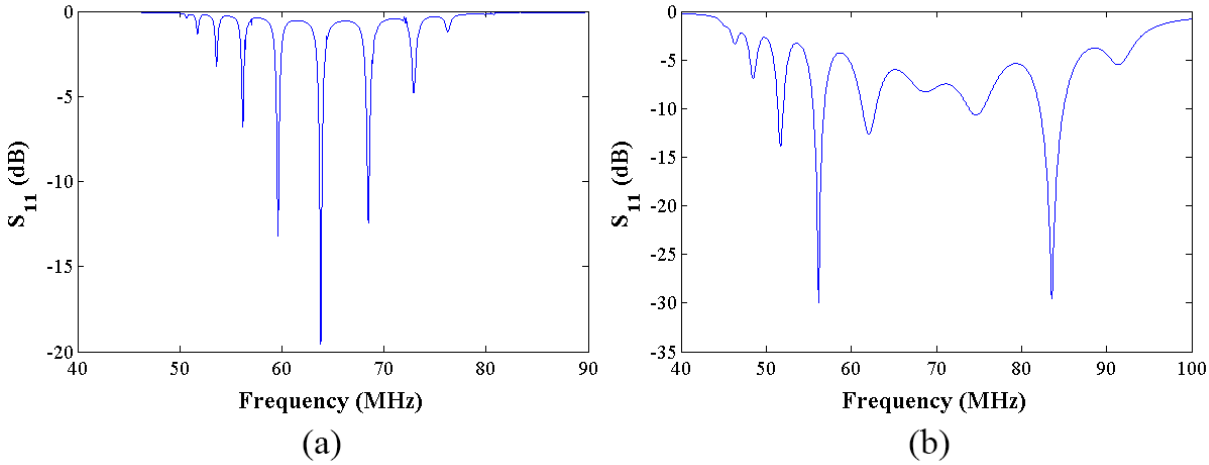


Figure 5.22 Frequency variation of S_{11} obtained at (a) the start, and (b) the end of the transducer matching process

Detector matching was then verified, as follows. A modified AWR layout containing a resonant detector was first defined as shown in Figure 5.23. The detector was deliberately chosen to be different from both the tap and the cable, and had the following electrical values: L_D = 360 nH, C_D = 17.29 pF, R_D = 4.80 Ω. These parameters can again allow resonance at 63.8 MHz. An additional single loop connected to port 2 with 50 Ω impedance was placed on one side of the detector to measure the transmitted power.

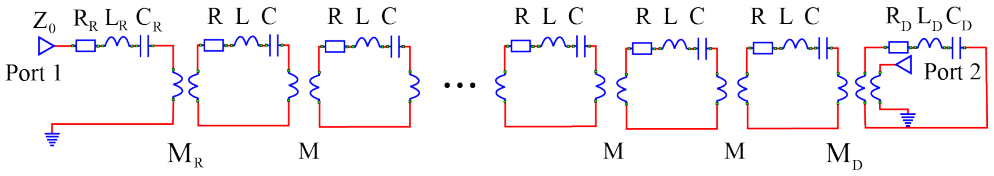


Figure 5.23 Circuit arrangement during matching of the detector

The mutual inductance (M_D) or the coupling coefficient (κ_D) between the cable and the detector was then adjusted to achieve a deep null in reflection or a maximum in transmission at 63.8 MHz as shown in Figure 5.24 below. This result shows the matching of all components can be achieved when κ_D = 0.2595. This value should be compared with the previously estimated value needed for matching, namely κ_D = 0.1628. The discrepancy may be attributable to the additional effects of parasitic capacitance, to be discussed later. The transmission is low because a weakly coupled external loop is being used as a transducer.

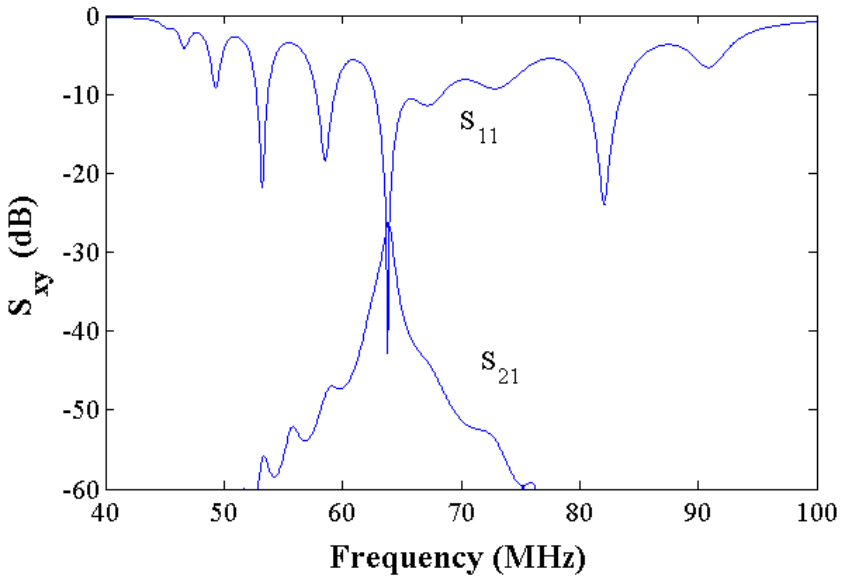


Figure 5.24 S_{11} and S_{21} measurement after matching of the detector

5.9 Electromagnetic Demonstration of Matching

We now present a full electromagnetic demonstration of matching, based on a realistic physical layout of a complete receiver. We first consider the RF detector. As previously described, the detector can be formed from a single element of the MI cable, as shown in Figure 5.25a, since it is already an LC resonator. However, a possible alternative design is a narrow-band transducer based on the two-turn spiral coil previously discussed in Chapter 4 [45]. Such a design is likely to have a higher Q-factor, In this case, longer and thinner capacitors are required to obtain sufficient flexibility. However, one of these must extend in front of the detector as shown in Figure 5.25b. Since this arrangement may prove dangerous, the single turn coil is almost certainly better. Both designs must be placed at the end of the magneto-inductive waveguide, overlapping the final element by an amount *b*. Their position can therefore be defined by a ratio *b*/*a*, where *a* is the period.

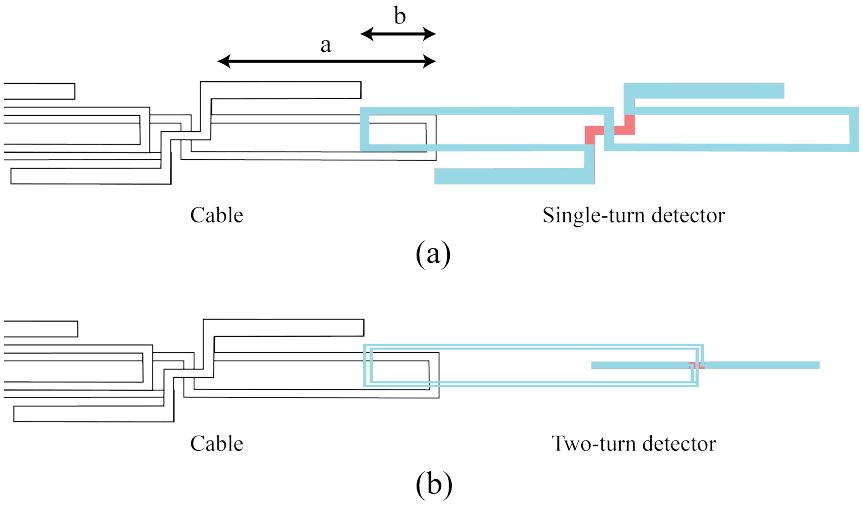


Figure 5.25 Alternative RF detectors based on (a) single turn and (b) two-turn inductors

Broadband or narrow-band transducers may be used as detachable taps as shown in **Figure 5.26**. The former is equivalent to a half of a single cable element, and the latter is again based on the previous design of a multi-turn RF coil in Chapter 4 [45]. However, the tuning and

matching capacitors are again made longer and thinner to improve flexibility, and additional tracks are attached to the two capacitors to allow connection to a 50 Ω system.

The mid-band impedance of the cable (Z_{0M}) will help us to determine which type of transducer is best for the application. Z_{0M} was previously estimated using our numerical model as approximately 38 Ω. Since this value differs significantly from 50 Ω, the two-turn spiral transducer is likely to provide better matching.

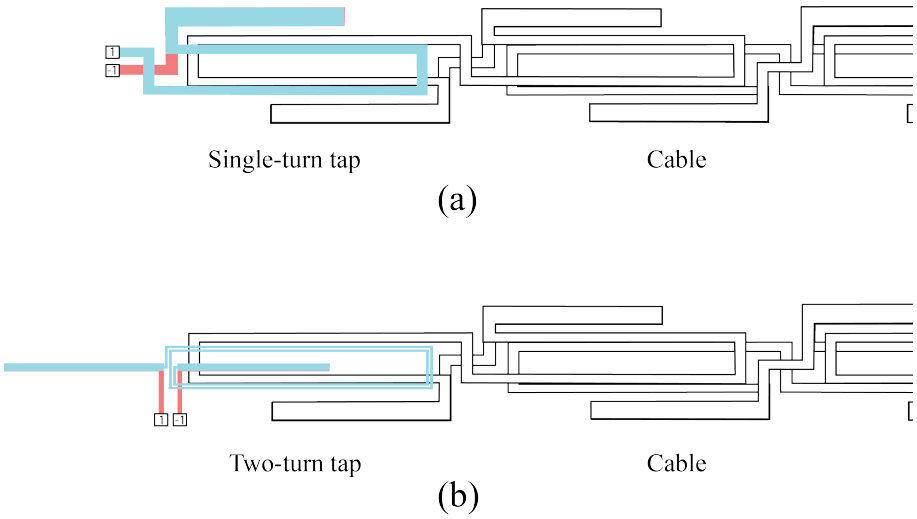


Figure 5.26 Detachable taps based on (a) single-turn and (b) two-turn transducers

In the real system, the complete thin film circuit, apart from the detachable tap, is mounted in a catheter using heat shrink tubing as shown in Figure 5.27. The detachable tap is then adjusted longitudinally to achieve impedance matching.

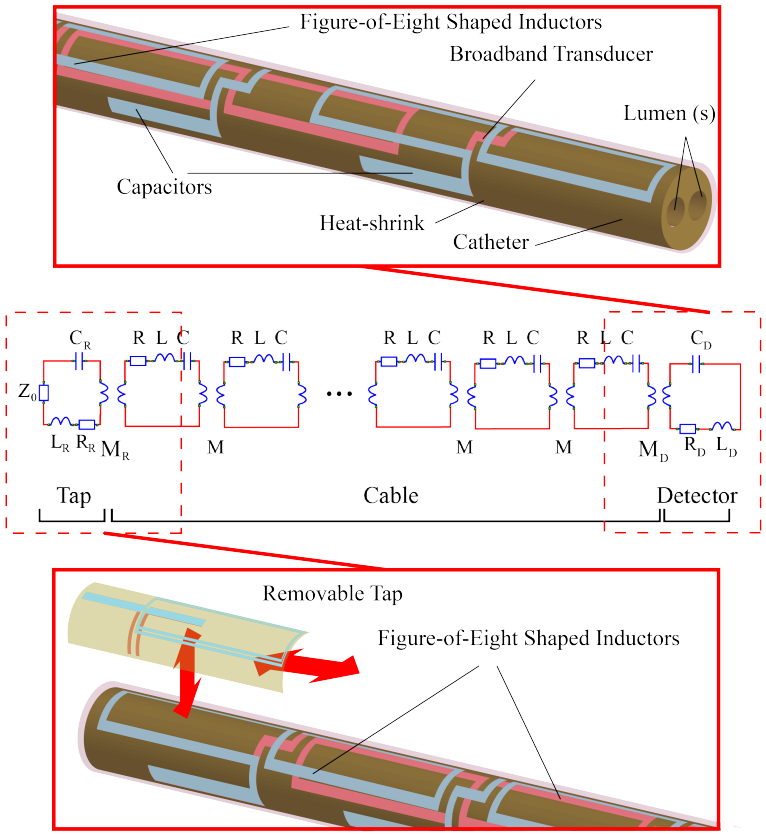


Figure 5.27 Catheter mounting of the complete RF receiver

The value of the ratio b/a determining the overlap between the detector and the final cable element needed for matching can be mathematically estimated using Equations (5.**15**) and as follows. When the two overlap completely, so that $b/a = 1$, the mutual inductance between them must be equal to M. Assuming that the mutual inductance is linearly proportional to the overlap, we will more generally obtain a value $M(b/a)$. Matching will therefore be achieved if $M_D = M(\frac{b}{a})$. We therefore require:

$$\frac{(\omega_0 M(\frac{b}{a}))^2}{R_D} = Z_0 \tag{5.18}$$

Rearrangement then leads to the optimum value of b/a of:

$$b/a = \sqrt{\frac{R_D}{Z_0}} \tag{5.19}$$

For example, if Z_0 = 50 Ω and R_D = 2.79 Ω, we obtain b/a = 0.23, implying that 23% overlap is needed for matching.

5.10 Simulation of Complete MR-safe Cable

A system with broadband transducers at either end of a MR-safe cable with the parameters previously given in Table 5.3 was first modelled using AWR MWO as shown in Figure 5.28. A DELL precision T7500 workstation with six cores of Intel® Xeon® CPU X5680 operating at 3.33 GHz, 24.0 GB of RAM and 64-bit operating system was used. This system has sufficient processing power to provide effective simulations of up to 9 sections of MR-safe cable. Previously extracted material and dimensional parameters were used ($tan\ \delta$ = 0.006, σ = 2.96 e+007 S/m, and W_L = 5.0 mm). The variations of reflection and transmission (S_{11} and S_{21}) were compared with the predictions of a Matlab implementation of the analytical equations previously given in section 5.7). This model is fully described in Appendix B.

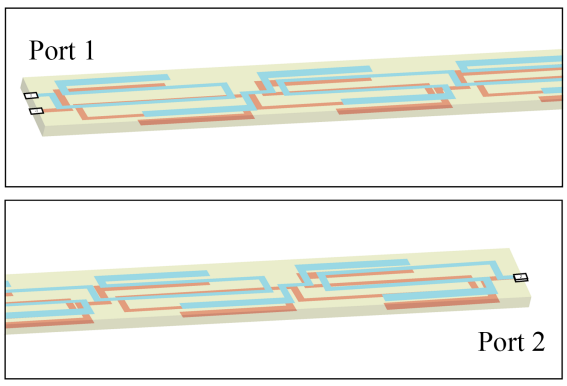


Figure 5.28 AWR model of a MR-safe cable with broadband transducers

Figure 5.29 compares the frequency variations of S_{11} and S_{21} obtained using the analytical and numerical models, after adjustment of the transducer positions. As can be seen, the results are very similar. The magneto-inductive band ranges from 50 to 120 MHz. Peak transmission through the system is around -5 dB, implying that propagation losses are low. Furthermore, the reflection coefficient shows a deep null (S_{11} ~20 dB) over the majority of the MI band, indicating that broadband impedance matching has indeed been achieved.

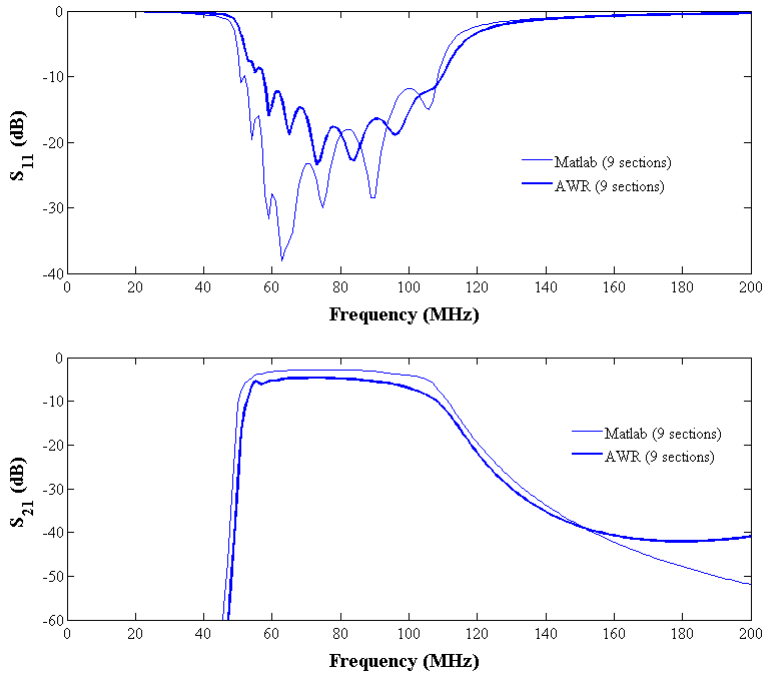


Figure 5.29 Variations of S_{11} and S_{21} with frequency for a 9-section MR-safe cable with broadband transducers, predicted by Matlab and AWR MWO

A complete RF receiver based on a two-turn tap and a single-turn detector integrated with the same 9-section length of MR-safe cable was then modelled using AWR MWO as shown in Figure 5.30. In reality, the signal should be injected at the detector. However, since the system is reciprocal, the system was injected at the tap (port 1) for simplicity. An additional rectangular loop was placed near the detector to detect the output. The detector position was first adjusted to achieve matching, which required an overlap b/a = 0.26. This value should be compared with the previous estimate of 0.23; the two values are in good agreement.

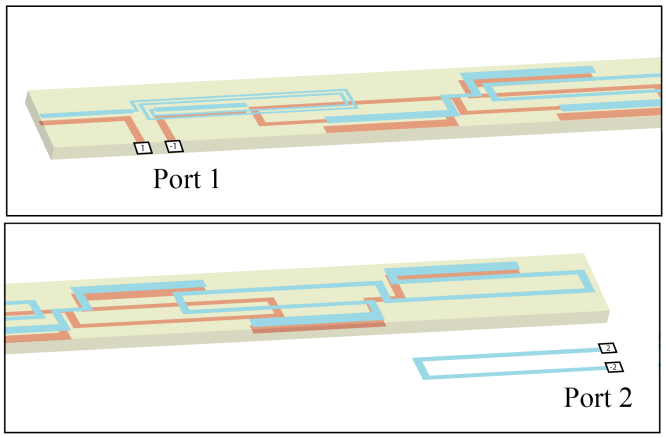


Figure 5.30 AWR model of 9-section MI cable with a two-turn tap and a resonant detector

Figure 5.31 shows the frequency variations of transmission and reflection (S_{21} and S_{11}) obtained using AWR MWO, and also using a simple MATLAB implementation of the analytic model (again, described in Appendix B). To compensate for the use of a weak inductive tap, the numerical variation of S_{21} is is raised up by +29 dB for comparison with the analytical model. Once again, two results are in excellent agreement. However, in each case there is now a sharp peak in transmission at the resonant frequency (63.8 MHz) indicating that the system is functioning as a resonant detector, with a Q-factor of 40.

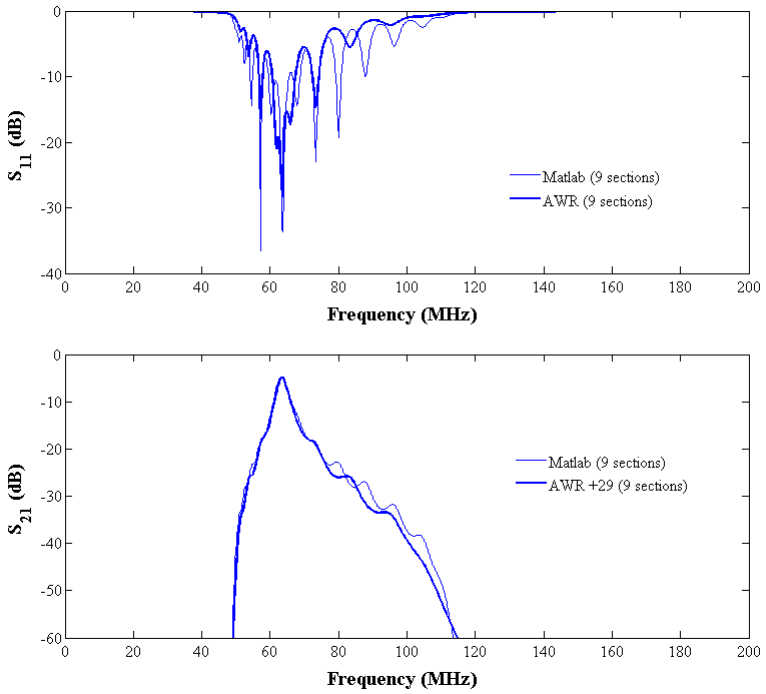
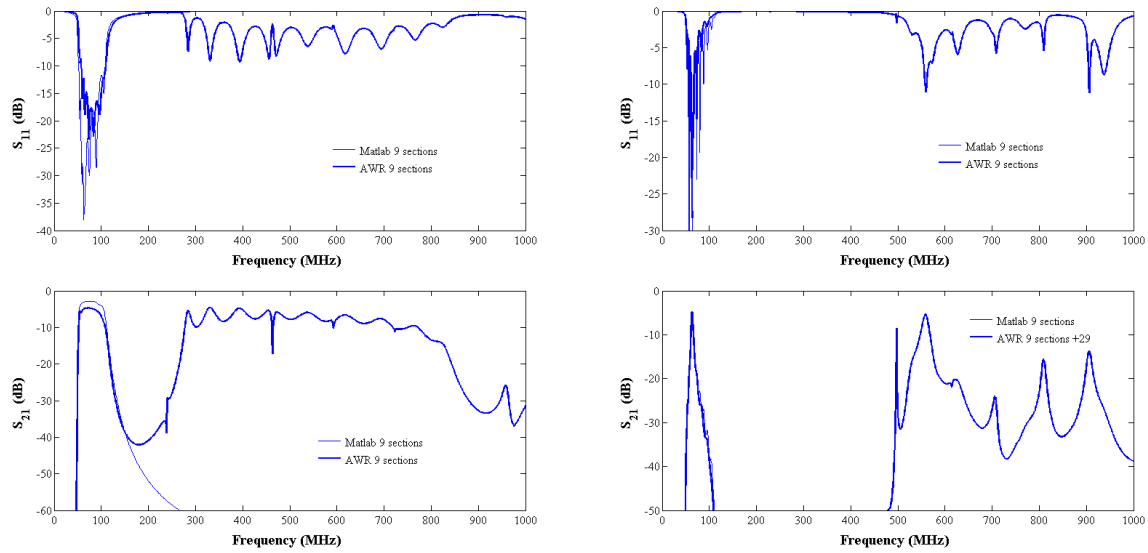


Figure 5.31 Variation of S_{11} and S_{21} with frequency for a MR-safe receiver based on a single turn detector and a two-turn transducer, as predicted by Matlab and AWR MWO

5.11 Parasitic Capacitance

We now consider the possibility of electric coupling between adjacent elements of MI cable, caused by parasitic capacitance between closely spaced tracks in the region where the inductors are overlaid to achieve strong magnetic coupling. This effect has previously been shown to introduce additional unwanted transmission bands at high frequency [125].

To do so, the numerical models previously shown in Figure 5.28 and Figure 5.30 were simulated again, this time over an extended frequency range. The frequency variations of S_{11} and S_{21} obtained in each case are shown in Figure 5.32a and Figure 5.32b respectively. An additional high frequency band ranging from 280-820 MHz can be seen, especially in Figure 5.32a, confirming the predictions of [125]. However, apart from high frequency propagation, the effect does not appear to compromise the operation of the receiver system significantly.



(a) (b)

Figure 5.32 High frequency performance of the systems in **Figure 5.27** and **Figure 5.28**

5.12 Experimental Verification of Detector Integrated with MR-Safe Thin-film Cable

Complete MR-safe receiver systems with variations in the detector overlap ratio b/a were fabricated in copper-clad polyimide by Clarydon. The main physical dimensions are as given in Table 5.1, assuming an inductor width of W_L = 4 mm. 15-element cables give an overall length of (15+1) x 200/2 = 1600 mm, sufficient to pass the biopsy channel of the endoscope (1400 mm length) with around 100 mm excess at either end. Figure 5.33 shows a complete panel of receivers. Individual circuits were then separated using a scalpel, the capacitors in each element were tuned to set the resonant frequency to the correct value, and the circuits were then mounted on hollow plastic scaffolds using heatshrink tubing to form complete catheter-based receivers [126].

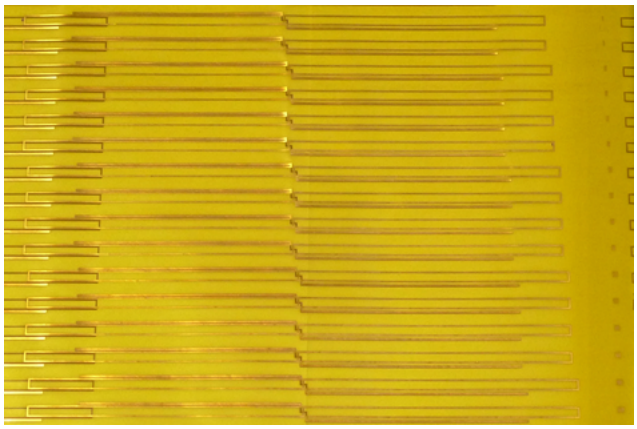


Figure 5.33 Experimental PCB panel, showing resonant detectors integrated with MR-safe cables

A demountable tap was constructed from a two-turn thin-film spiral inductor mounted in a split Perspex clamp, and the electrical performance of the completed receiver was measured using an Agilent electronic network analyser in an air environment. Frequency variations of the scattering parameters were obtained as shown in Figure 5.34. As can be seen, impedance matching and resonant detection are both achieved at the required frequency (63.8 MHz) and a loaded Q-factor of 30 is obtained [126]. Once again the transmission is low because a weakly coupled external loop is being used as a transducer.

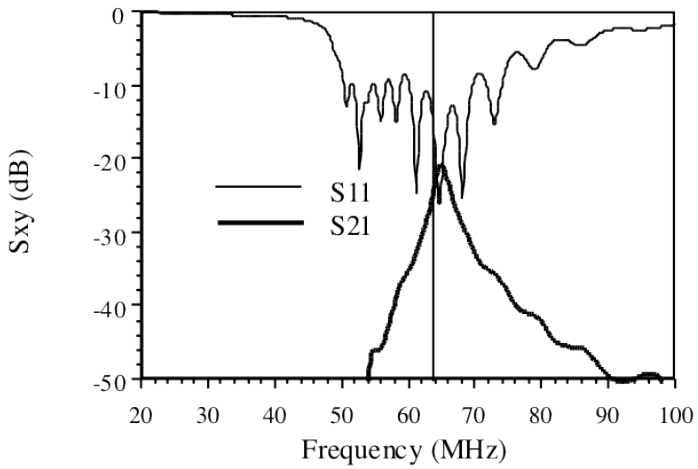
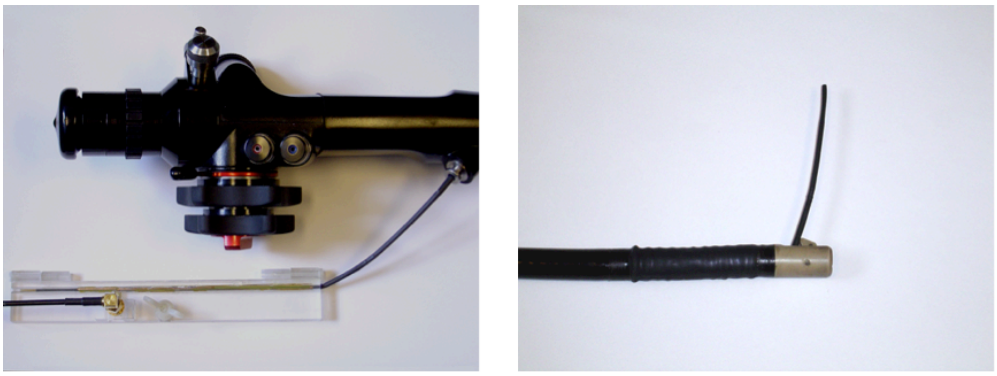


Figure 5.34 Response of completed experimental catheter receiver in air

5.13 Endoscopic Application

The mechanical flexibility is required to enter into the duct after all the thin-film MI-safe cable mounted over the catheter. Use of the completed catheter in conjunction with an existing non-magnetic, side-opening gastroscope was then demonstrated by Prof. Richard Syms and Dr. Munir Ahmad, as shown in Figure 5.35a. Clearly, the catheter is capable of passing the entire length of the biopsy channel, and emerging at the distal end with a 90^{o} bend [126].



(a) (b)

Figure 5.35 Catheter passing gastroscope, at (a) proximal and (b) distal ends

Frequency variations of the scattering parameters were then obtained with the catheter completely immersed inside the gastroscope, as shown in Figure 5.36. Compared with the results obtained in air, the main effects observed are a degradation of the impedance matching and a reduction of the Q-factor to around 23, presumably due resistive losses in a curved metal section subsequently found to be located at the input of the biopsy channel. Additional important mechanical problems were also found. Inserted catheters could not be removed from the gastroscope without damage. The curved metal section was found to act as a very effective wire stripper, removing the majority of the heatshrink sleeve and much of the cable beneath. Further work is therefore clearly required to improve mechanical and electrical compatibility of the gastroscope. A solution has been found for a newly completed

gastroscope; the curved metal section responsible for the mechanical damage has been replaced with a plastic section with no sharp edges, fabricated using rapid prototyping.

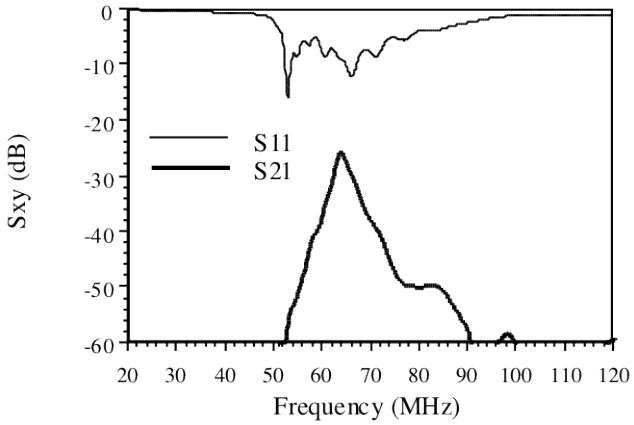


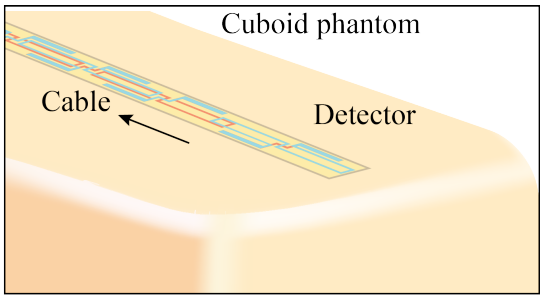
Figure 5.36 Response of completed experimental catheter receiver in gastroscope

5.14 Magnetic Resonance Imaging

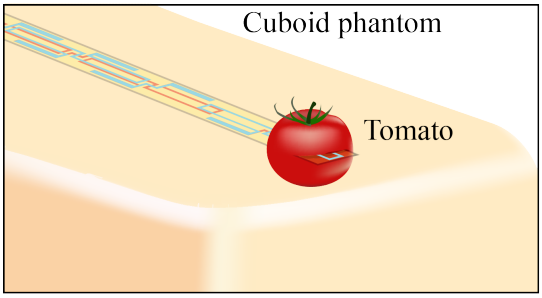
^{1}H MR imaging was carried out by Prof. Richard Syms and Dr Marc Rea using a 1.5 GE Signa Excite clinical scanner at St. Mary's hospital, Paddington. Two experiments were carried out, using the arrangements shown in Figure 5.37. In the first experiment, the catheter receiver was placed on top of a cuboid phantom containing a doped water solution as shown in Figure 5.37a. Imaging was performed using a 2D Axial T2 sequence, with an excitation time TE = 3.44 msec, a repetition time TR = 68 msec and a flip angle of 30^{o}. Images were obtained as a set of coronal slices, with a slice thickness of 5 mm and a slice separation of 5.5 mm. Figure 5.38a shows a slice immediately beneath the catheter receiver. The image clearly consists of a linear array of bright segments, each derived from signals detected near half of one of the figure-of-eight loops of the circuit. The receiver clearly generates a short-range image along its length, right up to the tip of the catheter.

In the second experiment, the tip of the catheter was inserted into a plum tomato as shown in Figure 5.37b. Imaging was again performed using a 2D Axial T2 sequence, with TR = 120 ms and TE = 2.936 ms, a flip angle of 35^{o}, 3 mm slice thickness, and 3.3 mm slice

separation. Figure 5.38b shows a coronal slice sequence in a layer enclosing the catheter, which can be identified as a darker central track. An image is clearly obtained over the whole volume of the tomato, albeit with a signal-to-noise ratio that decreases with radial distance. At present, the SNR is somewhat worse than was achieved using thin-film coils with conventional miniature coaxial output cables in previous study [41]. However, these experiments confirm that the catheter receiver is capable of MRI imaging.

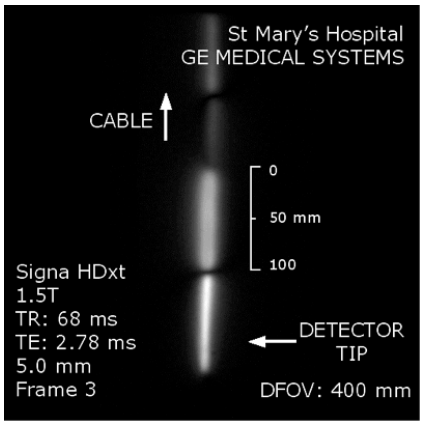


(a)

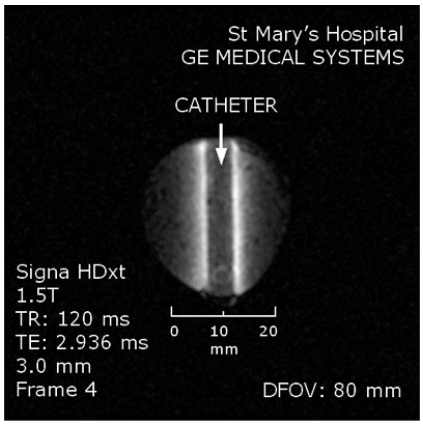


(b)

Figure 5.37 Arrangements for magnetic resonance imaging



(a)



(b)

Figure 5.38 ^{1}H MR imaging results: (a) phantom, showing catheter track and (b) tomato

5.15 Discussion

MR-safe magneto-inductive cables, which are intended to prevent the RF heating effect observed in a continuous conductive wire, have been modelled using analytic theory and numerical EM simulation. The results show that the correct resonant frequency for ^{1}H MRI imaging at 1.5 T can be obtained, but the cable itself cannot easily achieve an impedance of 50 Ω. Transformer matching schemes have been proposed to provide impedance matching. The mid-band impedance (Z_{0M}) determines which type should be used; broad-band transducers can be used if the cable impedance matches the system impedance, and narrow-band transducers otherwise. The agreement between the analytic model and numerical simulation is good. Prototype MR-safe receivers have been fabricated and assembled onto catheter scaffolds. Their electrical performance has been evaluated in isolation, and also in conjunction with a non-magnetic gastroscope, and some mechanical and electrical difficulties have been identified. Finally, initial ^{1}H MR imaging experiments have been carried out, and images of phantoms have been successfully obtained. However, further work is required to verify electrical safety in tissue, and the effect of plastic cladding materials. This work is described in the following Chapter.

5.16 Publication

The work presented in this Chapter has resulted in this publication:

"Design of Magneto-Inductive Magnetic Resonance Imaging Catheters". by K. Segkhoonthod, R.R.A. Syms, I.R. Young, Sensors Journal, IEEE, 2014. **PP**(99): p. 1-1.

6. HEATING EFFECT

In previous Chapters, the fundamental causes of RF heating were introduced, together with their effect on the design of MR-safe cables for internal MRI. In this chapter we consider in detail the different effects of electrical and magnetic decoupling, and also investigate of the plastic surrounding effects on the cables, which were previously neglected.

6.1 MR Safety and Compatibility Standards

A number of regulatory agencies are concerned with the safety of patients and staff during MRI examinations. These include the Federal Communication Commission (FCC), the Food and Drug Administration (FDA), the European Union (EU) Notified Bodies, the International Commission on Non-Ionizing Radiation Protection (ICNIRP), the European Committee for Electrotechnical Standardization (Cenelec), the International Committee on Electromagnetic Safety (ICES - IEEE Standard C95.3-2002) and ASTM International. These organisations are responsible for approving any new surgical tools, medical implants, electronic and mechatronic equipment to be used within a MR environment. Three safety concerns have been highlighted by these organisations: magnetically induced torques or forces, RF induced heating, and MR compatibility, which are affected by static magnetic fields, pulsed radiofrequency (RF) energy and time-varying gradients, respectively [127, 128].

Magnetically induced torques and forces are clearly important, but in this thesis, RF induced heating is the main focus. Heating effects are commonly described in term of the specific absorption rate (*SAR*) in microwave applications. *SAR* can be expressed as:

$$SAR = \frac{P}{\rho} = \frac{\sigma E^2}{2\rho_t} = \frac{J^2}{2\rho\sigma} \tag{6.1}$$

Where P is the power loss density, E is the electric field strength, J is the current density, and the unit of *SAR* is W/kg. The limit of heating specified by the MR Safety standards such as ASTM F2503 and IEC can be represented in terms of *SAR* as:

US and Canada	1.6 W/kg averaged over 1g of tissue
EU, Japan & Brazil	2.0 W/kg averaged over 10g of tissue

A further aspect of MR compatibility (which does not affect patient safety) involves image artefacts. Artefacts are local image distortions, which may have a variety of causes including the insertion of materials with non-zero or varying magnetic susceptibility that locally alter the magnetic field. Artefact generation can be affected by many factors such as the magnitude of the B_0 field, the RF pulse sequence used, and device materials and orientation. Here, we focus on materials. Since the catheter receiver is to be delivered using a duodenoscope, the majority of the device structure must be plastic to allow sufficient flexibility. Although plastics are low-susceptibility materials, they all contain hydrogen (^{1}H), which may in principle result in image artefacts. A number of different plastics are used in the catheter receiver. These include the thin-film PCB substrate, the catheter scaffold and the heat-shrink tubing, made of polyimide (PI), polyolefin, and polytetrafluoroethylene (PTFT) respectively. Figure 6.1 shows the overall structure of an immersed catheter, which will be a key focus of later simulations.

In fact, experiments have not so far revealed any susceptibility effects with these materials. We therefore focus on B_1 and E field decoupling, and the effect of the various plastics on electrical parameters such as the effective permittivity (ε_r) of the surround, the parasitic capacitance (C_S) in the cable, the quality factor (Q_0) of the resonant elements and their coupling coefficient (κ), and finally *SAR* estimation.

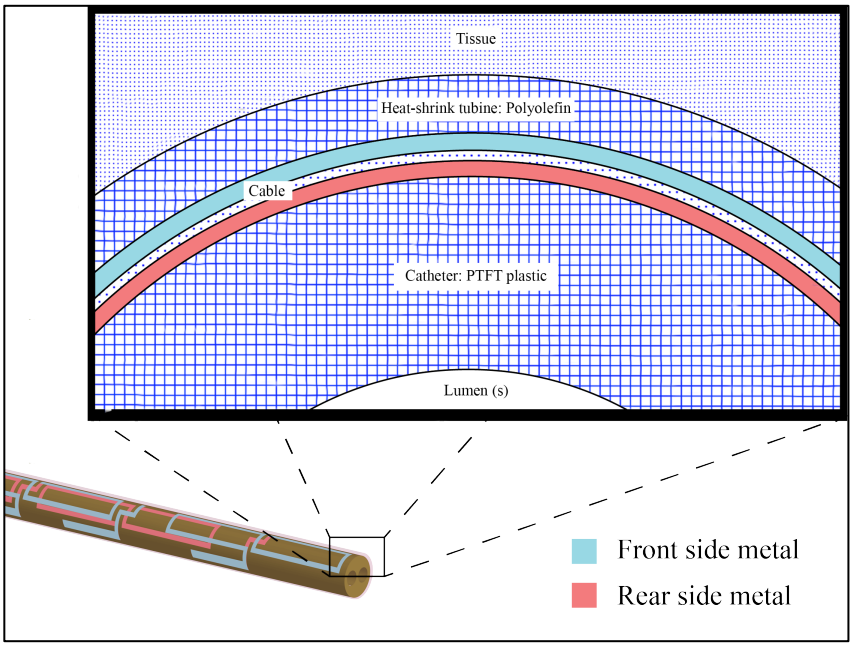


Figure 6.1 Material composition of immersed catheter receiver

6.2 MR Biological Models

RF energy can couple to the surrounding biological tissue, causing RF absorption and heating. The electromagnetic properties of any internal organs such as the dielectric constant (ε_r) and dielectric conductivity (σ) depend strongly on frequency, irradiation time, organ size and physiological function, and patient size, age and condition. These different variables all strongly affect the interaction of electromagnetic radiation at the cellular and molecular level. The EM properties of human tissue have been studied for several decades [129-131]. For example, Figure 6.2 shows typical frequency variations of ε_r and σ for different internal organs. Because of this variation, simulation of human anatomy in a MR application is extremely difficult and complicated, especially given additional patient-to-patient variability.

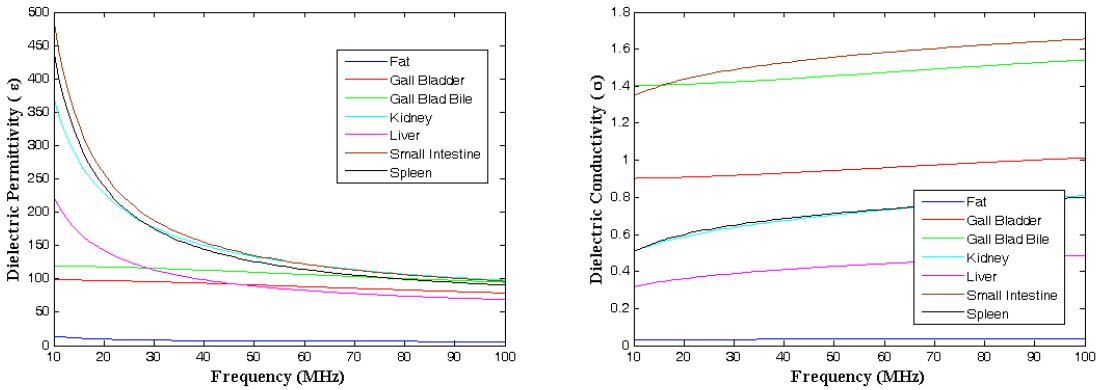


Figure 6.2 Frequency variations of body tissue dielectric parameters: (a) dielectric permittivity and (b) conductivity [131]

Based on data of this type, several commercial EM software packages such as ANSYS HFSS and CST-Computer Simulation Technology offer anatomical models for simulation of RF heating. For example, in the CST STUDIO SUITE, the anatomical models HUGO and DONNA are provided, simulating adult males and females respectively. Figure 6.3 shows HUGO, which is based on anatomical data obtained during the Visible Human Project®. HUGO can be used together with the bioheat formulae to modelling the temperature rise caused by RF heating in a human liver [132], and allows a number of electrical parameters such as the local electric field, power loss, and temperature distribution to be obtained. However, these models are costly, and require considerable resource such as a high performance workstation to operate effectively.

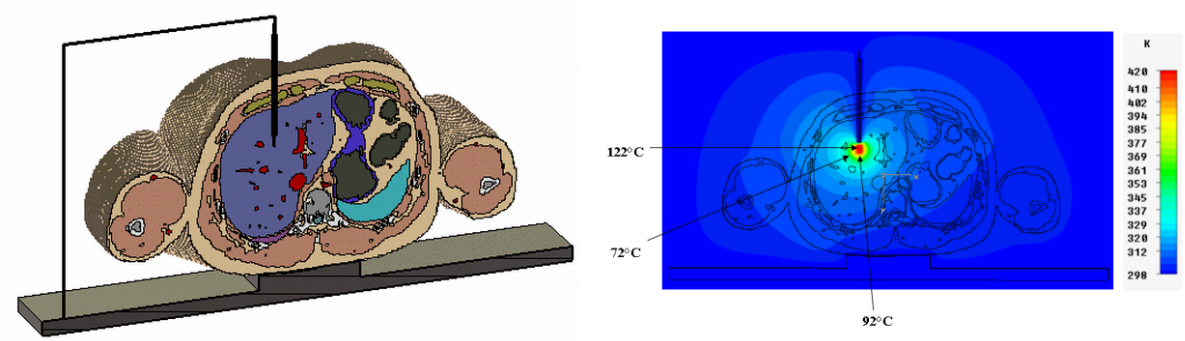


Figure 6.3 HUGO anatomical model used to model heating effects in CST [132]

Simpler models consider the surrounding environment simply to be a homogeneous fluid. This approach is realistic for environments that may be considered locally constant, such our internal MRI system. There are two types of fluids in a human body; intracellular and extracellular fluids, which are composed of the principal cation and anion (K^+, HPO_4^{2-} and Na^+, Cl^- respectively). Consequently, non-biological solutions such as NaCl, $CuSO_4$, $NiCl_2$ that resemble body fluids are widely in tissue phantoms to mimic the surrounding tissues or small organs because these chemical solutions represent electrolytes in the human cell [63, 71]. Solutions such as NaCl are often used to measure temperature effects when conducting wires are immersed in MRI phantoms [133, 134]. Here we will use NaCl in simulations. At room temperature, NaCl has dielectric constant ε_r = 77, conductivity σ = 0.45 S/m, and density ρ = 1066 kg/m^3. Note that, these EM properties depend on the solution concentration. The phantom in this work is a low salinity of NaCl dissolved in water (2.4 g/L NaCl).

6.3 Capacitor-Segmented Transmission Lines

As previously stated, electrical heating of insulated wires in conductive media can occur during internal MRI, if resonances are excited on long conductors by the electric field near transmitter coil capacitors. Electrical heating can be reduced by subdivision; however this strategy may fail if (as is the case for MR-safe cable) there is additional parasitic capacitance between nominally divided segments. Parasitic capacitance is expected in MR-safe cable because the elements are overlaid closely to achieve strong magnetic coupling. This parasitic capacitance limits the effective subdivision of the cable, and hence its ability to prevent RF heating. Furthermore, the value of the parasitic capacitance is not stable, and will increase when the cable is immersed in a material with high dielectric constant such as tissue. In this section, we develop an analytic model for wave propagation in imperfectly segmented immersed conductors.

We start by considering infinite systems. We model the immersed conductor as a transmission line, whose inductance and capacitance are chosen to represent the surrounding

medium. For a medium with permeability μ_0 and permittivity $\varepsilon_0\varepsilon_r$ the line has a per-unit-length inductance and capacitance $L_P = \mu_0$ and $C_P = \varepsilon_0\varepsilon_r$. For an infinite line, these values yield a characteristic impedance $Z_0 = (L_P/C_P)^{1/2} = (\mu_0/\varepsilon_0\varepsilon_r)^{1/2}$ and a propagation constant $k = \omega(\mu_0\varepsilon_0\varepsilon_r)^{1/2}$ in the lossless case. However, a per unit length resistance R_P can be introduced to represent losses.

Imperfectly segmented lines can be modelled by introducing lumped-element series capacitors C_S at regular intervals d, as shown in Figure 6.4. This arrangement is analogous to the Kronig-Penny model of the periodic potential of a one-dimensional crystal in solid-state physics, and a similar approach can be used for the analysis.

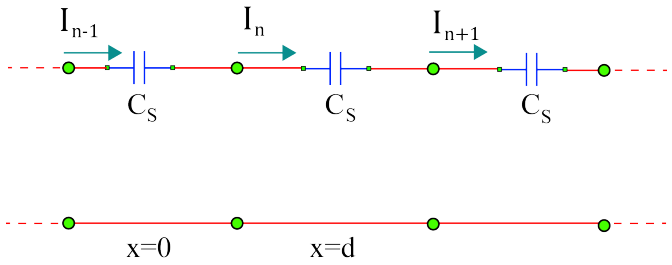


Figure 6.4 Infinite transmission line periodically loaded with capacitors

To model propagation of waves along the line, we assume that the solution for the current at point x along the nth section can be written in the form of a Bloch wave (a periodically repeating pattern of forward- and backward-travelling waves used to represent lattice waves in solid-state physics), namely:

$$I_n(x) = \{I_F e^{-jkx} + I_B e^{+jkx}\} e^{-jn\phi} \tag{6.2}$$

Here, I_F and I_B are the amplitudes of the two waves and ϕ is the phase shift per section. The

current must of course be continuous everywhere. For example, matching at the junction between sections n and $n+1$ we must have $I_n(d) = I_{n+1}(0)$, and hence:

$$\{I_F e^{-jkd} + I_B e^{+jkd}\}e^{-jn\phi} = (I_F + I_B)e^{-j(n+1)\phi} \tag{6.3}$$

Regrouping terms, this result can be re-arranged as:

$$I_F\{e^{-jkd} - e^{-j\phi}\} + I_B\{e^{+jkd} - e^{-j\phi}\} = 0 \tag{6.4}$$

Hence the amplitude of the backward-going wave can be written as $I_B = rI_F$, where the reflection coefficient r is:

$$r = -\{e^{-jkd} - e^{-j\phi}\}/\{e^{+jkd} - e^{-j\phi}\} \tag{6.5}$$

Accompanying the current waves must be voltage waves. Their amplitudes may be found by multiplying the current amplitudes by Z_0 (including a minus sign for backward going waves). Thus we have:

$$V_n(x) = Z_0\{I_F e^{-jkx} - I_B e^{+jkx}\}e^{-jn\phi} \tag{6.6}$$

The voltage must also satisfy boundary conditions, in the form of an impedance condition at each capacitor. For example, at the junction between sections n and n+1 we must have $V_n(d) - V_{n+1}(0) = I_n(d)/j\omega C_S$ and hence:

$$Z_0\{I_F e^{-jkd} + I_B e^{+jkd}\}e^{-jn\phi} - Z_0(I_F - I_B)e^{-j(n+1)\phi} = \{I_F e^{-jkd} + I_B e^{+jkd}\}e^{-jn\phi}/j\omega C_S \quad (6.7)$$

Re-arranging, and defining a new term $\propto = jZ_0\omega C_S$ we obtain:

$$I_F\{(\alpha - 1)e^{-jkd} - \alpha e^{-j\phi}\} - I_B\{(\alpha + 1)e^{+jkd} - \alpha e^{-j\phi}\} = 0 \quad (6.8)$$

Equations (6.4) and (6.8) represent two simultaneous equations that relate I_F and I_B. Eliminating either I_F and I_B then leads to the determinant equation:

$$\{e^{-jkd} - e^{-j\phi}\}\{(\alpha + 1)e^{+jkd} - \alpha e^{-j\phi}\} + \{e^{+jkd} - e^{-j\phi}\}\{(\alpha - 1)e^{-jkd} - \alpha e^{-j\phi}\} = 0 \quad (6.9)$$

Multiplying out the brackets and combining terms, we then obtain:

$$4\alpha\cos(\phi) - 4\alpha\cos(kd) - 2j\sin(kd) = 0 \quad (6.10)$$

Substituting for $\propto$, we then obtain:

$$\sin(kd)/\{\cos(\phi) - \cos(kd)\} = 2Z_0\omega C_S \quad (6.11)$$

Since $k = \omega/V_{ph}$, where V_{ph} is the phase velocity of the unloaded line, we may write this result as:

$$\sin(\omega d/V_{ph})/\{\cos(\phi) - \cos(\omega d/V_{ph})\} = 2Z_0\omega C_S \quad (6.12)$$

Equation (6.**12**) is of course the dispersion equation of the loaded line, since it defines the relation between ω and ϕ. We now note that if the RHS above is zero (which would be the case of $C_S = 0$, and the line is completely segmented), the equation simplifies to:

$$\sin\left(\omega d/V_{ph}\right) = 0 \tag{6.13}$$

This equation of course defines the resonant frequencies of a single isolated section of length d. Its solution is:

$$\omega d/V_{ph} = \upsilon\pi \tag{6.14}$$

At each of these frequencies, the current forms a standing wave pattern with a whole number of half-wavelengths along each isolated segment. The dispersion equation may then be written in terns of the lowest order of these resonances (ω_1), as:

$$\sin(\pi\omega/\omega_1)/\{\cos(\phi) - \cos(\pi\omega/\omega_1)\} = 2Z_0\omega C_S \tag{6.15}$$

Introducing now the normalised quantities $w = \omega/\omega_1$ and $Z_n = Z_0\omega_1 C_S$ we obtain:

$$\sin(\pi w)/\{\cos(\phi) - \cos(\pi w)\} = 2Z_n w \tag{6.16}$$

The only 'structural' parameter above is Z_n, the ratio of Z_0 to the modulus of the impedance of the capacitor C_S at W_1. Consequently, the value of Z_n completely controls the behaviour of the system, and hence determines the effectiveness of the subdivision.

Normally, a dispersion equation of this type would be solved numerically to obtain w for a given Z_n. However, in this case, the equation can simply be re-arranged to yield Z_n for a given value of w, as:

$$Z_n = \sin(\pi w)/\{2w[\cos(\phi) - \cos(\pi w)]\} \tag{6.17}$$

Figure 6.5 shows the results obtained for the two cases of (a) $Z_n = 0.01$ and (b) $Z_n = 0.5$. In the former case, the line is effectively segmented, and the dispersion diagram approximates to the sets of straight lines $w = v$. In the latter case, bands start to appear, as might be expected from the analogy with solid-state physics. In the lowest band, it can be seen that w is significantly less than unity for small ϕ.

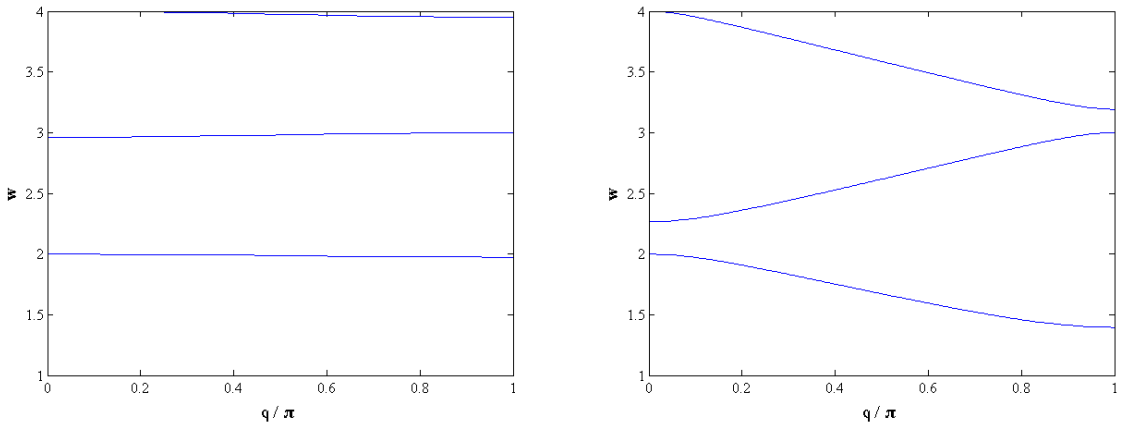


Figure 6.5 Dispersion diagram for an infinite capacitor-loaded line, for normalised impedances of (a) $Z_n = 0.01$ and (b) $Z_n = 0.5$

We now consider finite systems. Figure 6.6 shows a finite capacitor-segmented line, which consists of N segments of length d, starting at $n = 0$ and ending at $n = N-1$. A solution may be constructed for this case from the solution for an infinite line, merely by allowing the current to consist of two Bloch waves travelling in opposite directions, and choosing their parameters to satisfy the boundary conditions.

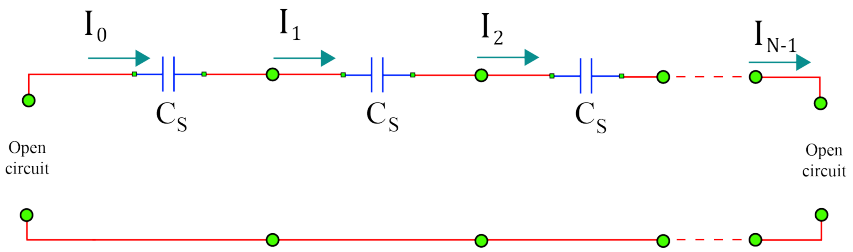


Figure 6.6 Finite transmission line periodically loaded with capacitors

A backward Bloch wave is simply obtained by taking the complex conjugate of a forward Bloch wave. In terms of the ration *r*, we may therefore write the total current as:

$$I_n(\mathrm{x}) = I_A\{e^{-jkx} + re^{+jkx}\}e^{-jn\phi} + I_B\{e^{+jkx} + r^*e^{-jkx}\}e^{+jn\phi} \tag{6.18}$$

Here I_A and I_B are the amplitudes of the two Bloch waves.

The boundary conditions for a finite line are that the current must be zero at either end, since the line is open circuited (OC). At th left-hand end we have $I_n(0) = 0$, and hence:

$$I_A(1 + r) + I_B(1 + r^*) = 0 \tag{6.19}$$

Consequently $I_B = sI_A$, where $s = -(1+r)/(1+r^*)$. The total current is now:

$$I_n(\mathrm{x}) = I_A\{e^{-jkx} + re^{+jkx}\}e^{-jn\phi} + sI_A\{e^{+jkx} + r^*e^{-jkx}\}e^{+jn\phi} \tag{6.20}$$

At the right-hand end, we have $I_{N-1}(d) = 0$ and hence:

$$I_A\{e^{-jkd} + re^{+jkd}\}e^{-j(N-1)\phi} + sI_A\{e^{+jkd} + r^*e^{-jkd}\}e^{+j(N-1)\phi} = 0 \tag{6.21}$$

Substituting for *s* and re-arranging slightly, we obtain:

$$(1 + r^*)\{e^{-jkd} + re^{+jkd}\}e^{+j\phi}e^{-jN\phi} + -(1 + r)\{e^{+jkd} + r^*e^{-jkd}\}e^{-j\phi}e^{+jN\phi} = 0 \quad (6.22)$$

At this point we note that:

$$(1 + r) = 2j\sin(kd)/[e^{+jkd} - e^{-j\phi}] \quad (6.23)$$

And:

$$\{e^{-jkd} + re^{+jkd}\} = 2j\sin(kd)e^{-j\phi}/[e^{+jkd} - e^{-j\phi}] \quad (6.24)$$

Consequently:

$$\{e^{-jkd} + re^{+jkd}\}e^{+j\phi} = 1 + r \quad (6.25)$$

And Equation (6.**22**) simplifies to:

$$(1 + r^*)(1 + r)e^{-jN\phi} - (1 + \mathrm{r})(1 + \mathrm{r}^*)e^{+jN\phi} = 0 \quad (6.26)$$

Or:

$$\sin(N\phi) = 0 \quad (6.27)$$

This result is particularly simple, since it implies that ϕ can only take the discrete values:

$$\phi = \mu\pi/N \tag{6.28}$$

Here μ is an integer. Combining this result with the dispersion characteristic for an infinite line, we obtain the following equation for the resonant frequencies of all finite lines, as:

$$\sin(\pi\omega/\omega_1)/\{\cos(\phi) - \cos(\pi\omega/\omega_1)\} = 2Z_0\omega C_S \tag{6.29}$$

In terms of the normalised quantities $w = \omega_1/\omega$ and $Z_n = Z_0\omega_1 C_S$ thus can be written as:

$$\sin(\pi w)/\{\cos(\mu\pi/N) - \cos(\pi w)\} = 2Z_n w \tag{6.30}$$

As we saw before, when Z_n tends to zero, Equation approximates to $sin(\pi w) = 0$ and hence has the solutions w = 1, 2, … (the resonant frequencies for isolated segments). Similarly, when Z_n tends to infinity, Equation approximates to $cos(\mu\pi/N) - cos(\pi w) = 0$ and has the solutions $w = 1/N, 2/N$ … (the resonant frequencies for a continuous line whose total length is equal to Nd).

Once again, this equation can be re-arranged to yield Z_n for a given value of w, as:

$$Z_n = \sin(\pi w)/\{2w[\cos(\mu\pi/N) - \cos(\pi w)]\} \tag{6.31}$$

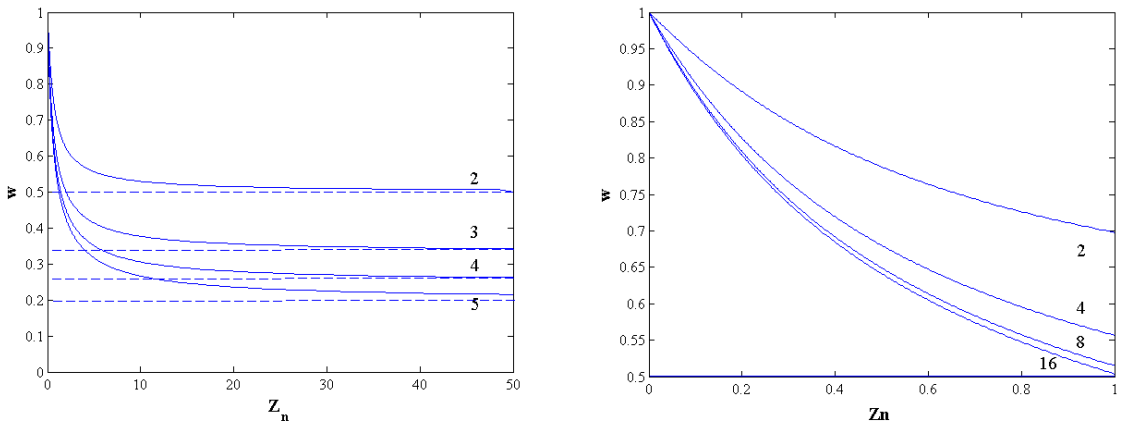
In studying RF-induced heating, we will general be interested in the lowest order mode, since this lies at the lowest frequency. More particularly, we will wish to arrange that the lowest resonant frequency of an immersed line always lies above the operating frequency of the MRI system. Thus, we focus now on the case when $\mu = 1$. Figure 6.7a shows the variation of w with Z_n, for lines of length N = 2, 3, 4, and 5. As can be seen, the solution is always w =

1 when $Z_n = 0$, but tends gradually to the limit $w = 1/N$ as Z_n increases. Thus, imperfect segmentation due to parasitic capacitance tends to reduce the lowest-order resonant frequency, with the effect being worse for longer lines than shorter ones.

However, Figure 6.7b shows a similar plot, focusing now on smaller values of Z_n and larger values of N (longer lines). Here we see that the effect shown above does have a limit; the line with $N = 16$ does not perform significantly worse than the line with $n = 8$. In fact, as N tends to infinity, the curves must all tend to:

$$Z_n = \sin(\pi w)/\{2w[1-\cos(\pi w)]\} \tag{6.32}$$

To operate correctly, a MR-Safe cable must be designed so that each isolated segment has a resonant frequency ω_1 higher than the operating frequency ω_0. If $w = \omega_0/\omega_1$ is higher than the lowest order resonance of an immersed cable, it will not be possible to excite a resonance, whatever the immersed length. The maximum value of Z_n that can be tolerated is then given by Equation (6.**32**).



(a) (b)

Figure 6.7 Variation of the lowest-order normalised resonant frequency with Z_n, for lines with different numbers of segments

We now consider the implications of the theory for MR-safe magneto-inductive cable. Figure 6.8a to Figure 6.8c show the layout of the cable and the common path, respectively. Note that, because of the overlay of adjacent sections, there are effectively two sets of parasitic capacitance per section, so that the segmentation distance is d = 10 cm, not the element length of 20 cm. Now, the critical length for a medium with ε_r = 77 (human tissue, at 63.85 MHz frequency) is around 27 cm. Assuming this value is roughly independent of frequency, a single segment of length 10 cm will resonate at f_1 = 63.85 x 27/10 = 172 MHz. The value of w is therefore 10/27 = 0.32. From Equation (6.**32**), it can be seen that the maximum allowed value of Z_n is approximately 2.

Previously we have estimated C_S as the series sum of two capacitors, a parasitic capacitance C_A and a capacitance C_B used to set the loop resonance, as shown in the cross-sectional sketch in Figure 6.8d. From measurements we have C_A = 5.8 pF (measured by making C_A resonate a known inductor) and C_B = 45.8 pF (twice the value used to set the resonance of each loop). Consequently, C_A is very small and should provide effective subdivision. The equivalent circuit of the capacitor subdivision is shown in Figure 6.8e. Using this data we have $1/C_S = 1/5.8 + 1/45.8$, leading to C_S = 5.2 pF. Consequently the normalised impedance Z_n is $43 \times 2 \times 172 \times 10^6 \times 5.2 \times 10^{-12} = 0.24$. Since $Z_n << 2$, the cable should never resonate at 63.85 MHz, whatever length is immersed. However, the experiments used to measure C_A were performed in air. Since C_A is a fringe-field capacitance, it will be larger if the air on one side is replaced with tissue having a high dielectric constant. However, its value would have to rise considerably to make much difference. We now consider how this may be estimated.

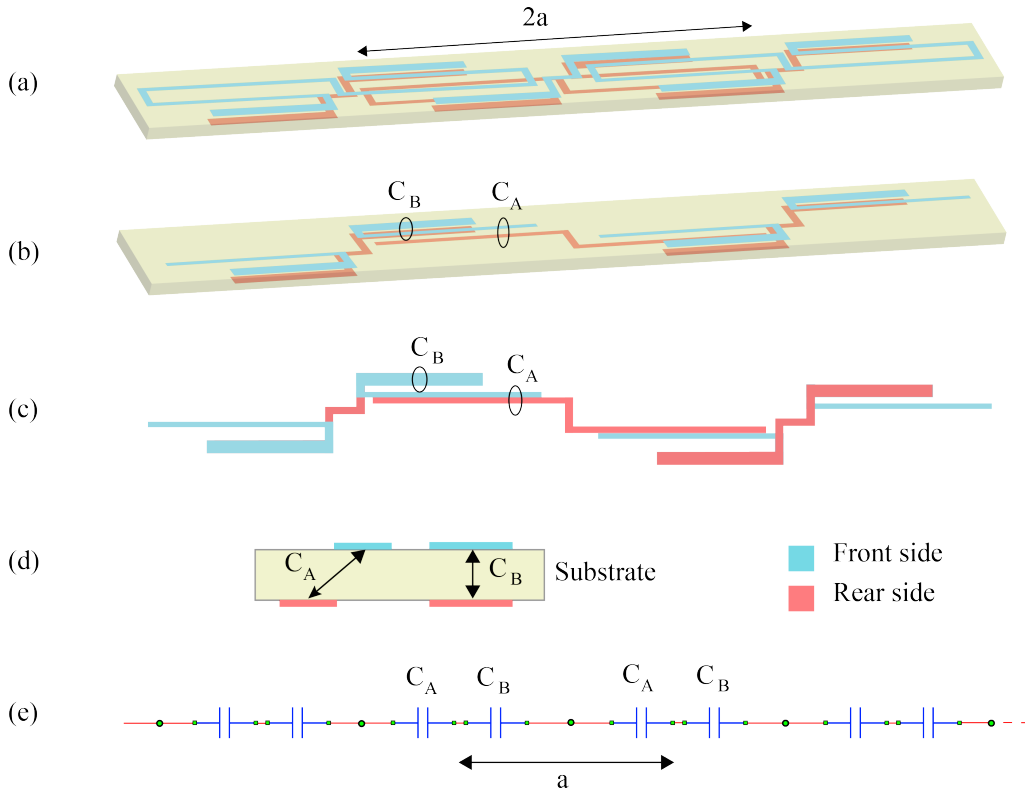


Figure 6.8 MR-safe cable (a) full 3D model, (b) and (b) 3D and 2D layout of the common mode path, (d) capacitors contributing to C_S (e) equivalent circuit of common mode path

6.4 Numerical Evaluation of Parasitic Capacitance

Analytic estimation of fringe-field capacitance is generally an extremely difficult problem, especially when (as here) an asymmetric distribution of surrounding material is involved. However, in this case only the magnitude of C_S is required, rather than a complete field distribution. This value may be found from an electromagnetic simulation of the resonance of an L-C circuit containing C_S as the capacitor, which may easily be carried out using AWR Microwave Office. To carry out such a simulation, we first note that the closely overlaid inductors in MR-safe cable can be simplified to a simple L-C circuit as shown in Figure 6.9 below. To find C_S, the value of the inductance L forming the resulting resonant circuit must be known. This can easily be found, by first simulating a circuit with L connected to a capacitor of known value. This procedure yielded a value $L \sim 125.62$ nH.

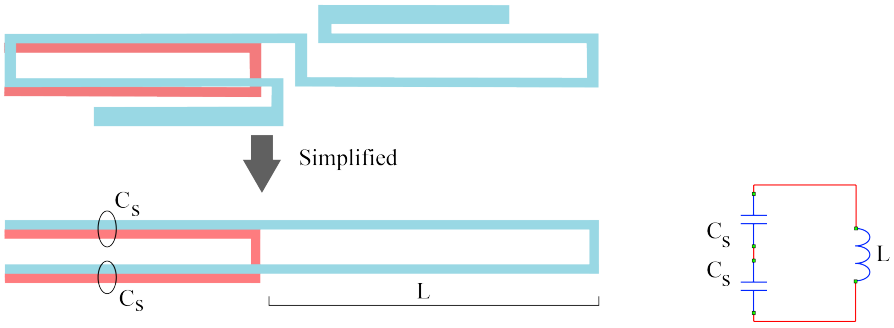


Figure 6.9 Layout used for simulation of parasitic capacitance

To find C_S with different surrounding environments, a resonant circuit based on two U-shaped metallic loops on a polyimide substrate was first defined as shown in Figure 6.10 together with ports labelled 1 and -1 for signal injection and extraction. Different environments were then created using combinations of air, tissue, polyimide, and polyolefin layers. These have relative dielectric constants of 1, 77, 3.4, and 2.7 respectively. The combinations investigated are represented as different seven layer structures labelled 6.1.1, 6.1.2 and 6.1.3 as shown in Table 6.1. The first has an air surround, the second has a tissue surround, and the third has a tissue layer above a thin polyolefin layer at the top, and a pure polyolefin layer at the bottom. In each case, the resonant frequency (f_0) could easily be obtained in an AWR simulation by inspection of the frequency-dependence of S_{11} or S_{21}. Once this has been done, the value of C_S was found from a standard equation for resonance, namely $\frac{C_S}{2} = \frac{1}{\omega_0^2 L}$. The values obtained for each of the models investigated are also shown in Table 6.1.

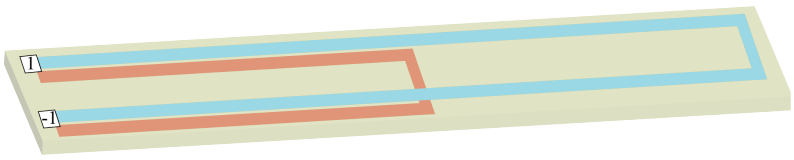
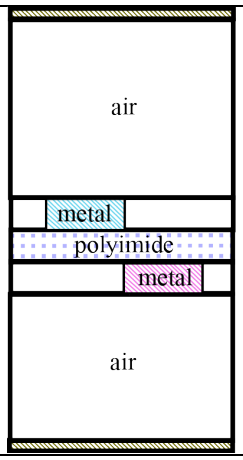
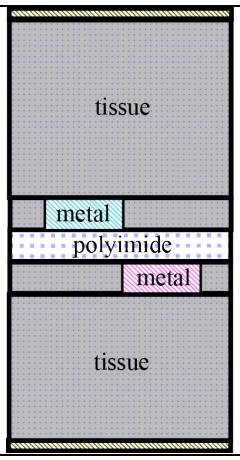
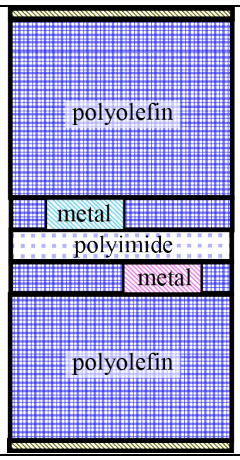
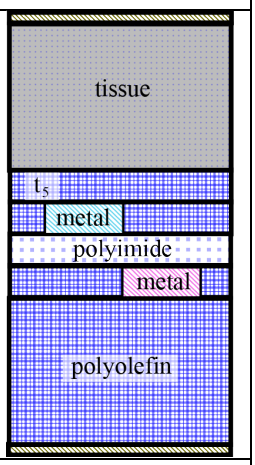


Figure 6.10 AWR model for parasitic capacitance simulation

As can be seen, the value of C_S (3.01 pF) obtained in a pure air environment (model 6.1.1) is in good agreement the estimation from the earlier analytical model. However, C_S is greatly increased (to 52.08 pF) if the closely overlaid inductors are completely surrounded by medium that has high dielectric constant such as tissue (model 6.1.2). Such a high value of C_S would be disastrous in a practical device, since it would effectively nullify the segmentation of the conductors. But if the surrounding medium is changed from tissue to plastic (model 6.1.3), C_S is greatly reduced to 6.11 pF. Fortunately, the thin-film circuit is mounted on a plastic catheter, and held in place using heat shrink tubing, also greatly reducing the dielectric constant of the immediate surround. Such a structure is represented in model 6.1.4. As can be seen, a greatly reduced value (7.56 pF) is now obtained. As a result, the thickness of any plastic under- and over-layers may be considered crucial in retaining effective segmentation.

Table 6.1 Extracted values of parasitic capacitance with different cable environments

Structure	**6.1.1**	**6.1.2**	**6.1.3**	**6.1.4**
t_6 (30 mm) t_5 (0.250 mm) t_4 (0.035 mm) t_3 (0.025 mm) t_2 (0.035 mm) t_1 (30 mm)				
f_0 **(MHz)**	366	88	257	231
C_S **(pF)**	3.01	52.08	6.11	7.56

We therefore consider this effect in slightly more detail, particularly since the thickness of the heat-shrink tubing (here represented as t_5) must be small (~ 250 um) in a practical catheter. Figure 6.11 shows the variation in C_S with heat-shrink thickness. C_S clearly reduces gradually from an initial value of 27.87 pF equivalent to ($C_{S\text{ of tissue}} + C_{S\text{ of polyolefin}}$)/2 when t_5 = 0 to a limiting value of around 6.11 pF when t_5 is large. However, only a few hundred microns thickness of heatshrink tubing are required to approach the limiting value.

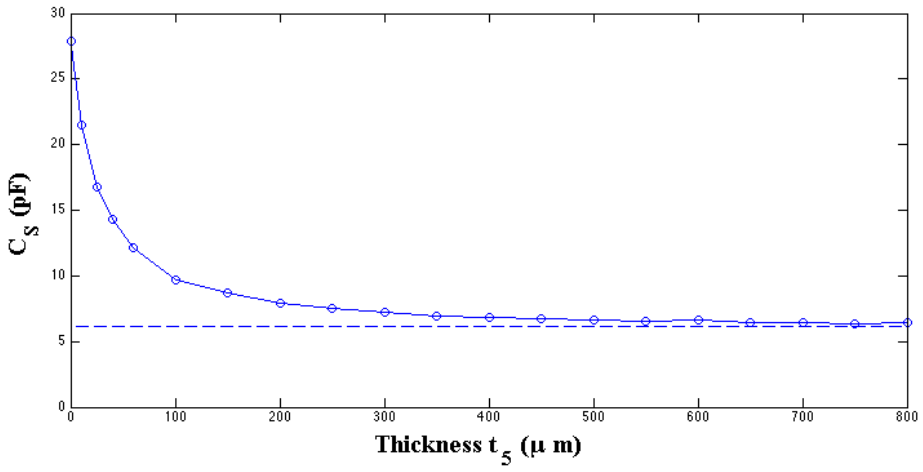


Figure 6.11 Variation of parasitic capacitance with heatshrink thickness t_6

6.5 Numerical Evaluation of Surface Wave Propagation

In previous section, we know that ε_r is strongly affected by any plastic surrounding layers. To study the effect on the propagation of surface waves, which can arise when a long conductive structure couples with the electric field produced in MR scanner, we first rearrange Equation (5.**3**) (which gave the resonant frequencies for surface waves on linear conductors) as:

$$\varepsilon_r \approx \frac{c^2}{(2l_d f_{1st})^2} \tag{6.33}$$

Using this formula, it is simple to extract the effective dielectric constant of the surround from a numerical calculation of the resonant frequency of a known length of conductor using AWR MWO. We now present the results of such a calculation.

In any such calculation, a system for electrical excitation and detection is required. Here, we chose to use dipole antennas as transmitters and receivers. A dipole is a length of conductor, with an excitation port at its midpoint, which resonates when its length approaches half a wavelength. For example, for resonance at 63.9 MHz in tissue, the dipole length (L_D) should

be $\frac{\lambda/2}{\sqrt{\varepsilon_r}} = \frac{2.351}{\sqrt{77}}$ =26.79 cm. The dipole antenna was first modelled and simulated using AWR MWO as shown in Figure 6.12a. Figure 6.12b shows the corresponding frequency variation of S_{11}, which clearly indicates that resonance at frequencies corresponding to λ/2, 3λ/2, and 5λ/2 can be achieved when the width of the conductor strips (W_D) is 1 mm. Note that even resonances do not occur, since these cannot be excited with a midpoint excitation. For use as a transducer, it is important to avoid resonance. The antenna length was therefore reduced closer to λ/10, and its layout was optimised to improve accuracy in the numerical calculation, leading to a final width of 0.25 mm and length of 400 mm.

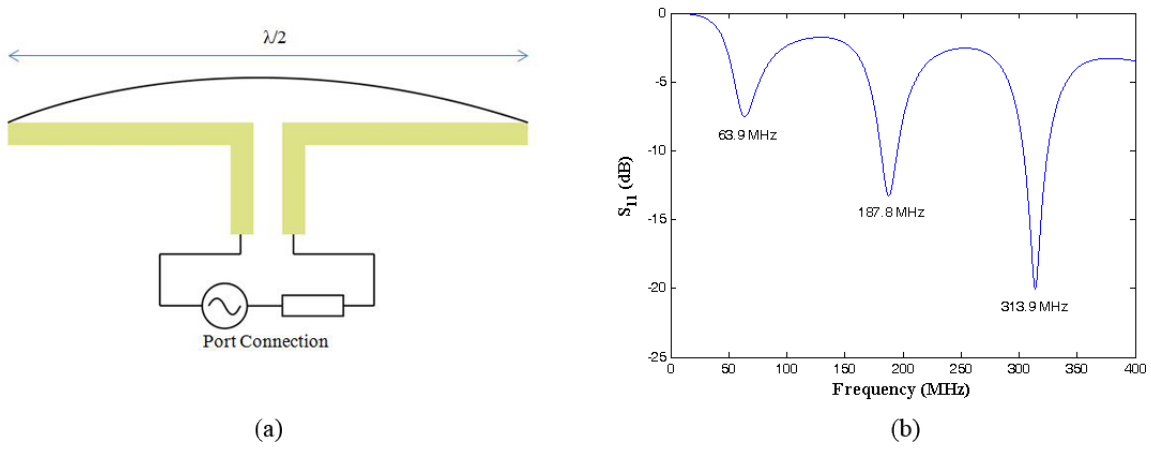


Figure 6.12 Electrical transducer: (a) half-wave dipole (b) corresponding frequency variation of S_{11}

The transducers were then used to excite and detect resonances in an immersed section of continuous conductor, as shown in Figure 6.13. Efficient excitation required the transducers to be located very close to the wire, so that L_G = 1.65 mm. Once again, different surrounding environments were investigated. The immediate surrounding layers were polyolefin and tissue. The lower polyolefin thickness was 35 mm thick, the copper was 35 μm thick, the tissue was 35 mm thick, and the thickness of the upper polyolefin cover layer was considered as a variable.

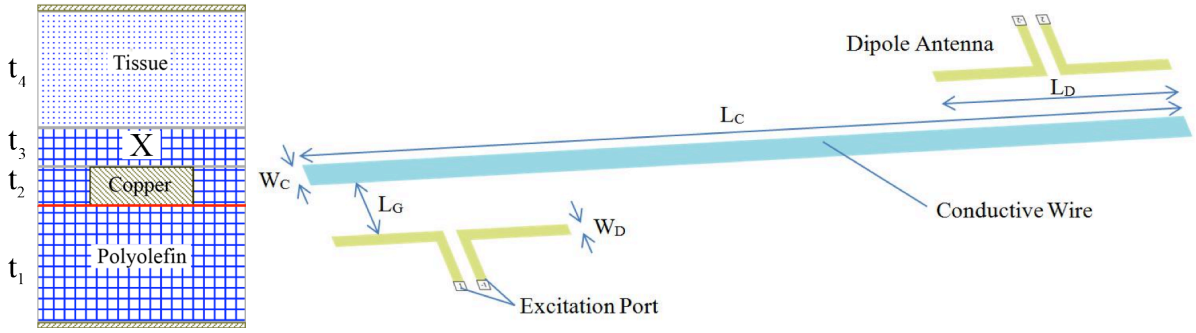


Figure 6.13 Layout used for simulation of immersed wires

The resonant frequency f_1 of the wire was first extracted from simulations of the transmission S_{21} between the transducers. This value then allowed allow the effective relative dielectric constant ε_r of the surround to be extracted using Equation (6.**33**). Figure 6.14 shows the variation of ε_r with the thickness of the polyolefin cover layer. When this thickness is zero, a value of ε_r is 39.10 is obtained. Since $(\varepsilon_{r\ \text{of tissue}} + \varepsilon_{r\ \text{of polyolefin}})/2 = (77+2.7)/2 = 39.85$, this result suggests that that the relative permittivity seen by the wire with a plastic substrate, a tissue cover but no heatshrink cladding is the average of the values of the two surrounding materials. However as the thickness of the polyolefin cover increases, ε_r falls towards 2.7, the value that would be obtained complete immersion of polyolefin. Consequently, the polyolefin heatshrink has the important feature of reducing the wavelength-shortening effect that arises during tissue immersion. Even relatively thin (a few hundred micron) heatshrink layers therefore provide additional protection.

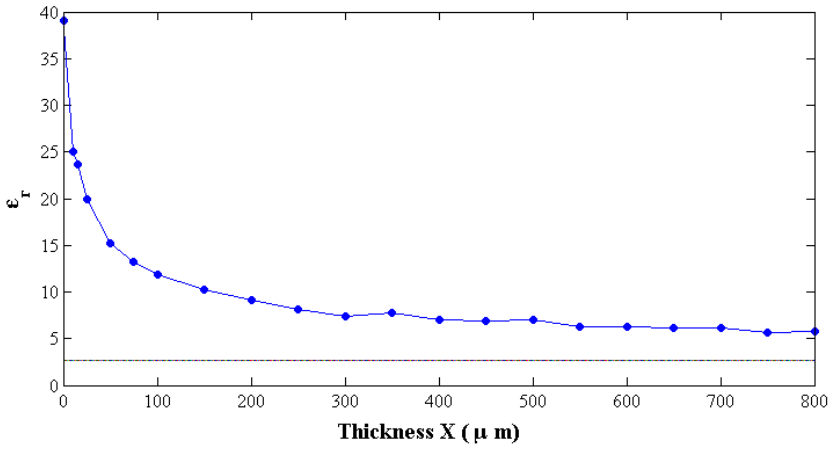


Figure 6.14 Variation of effective relative dielectric constant with cover layer thickness

An investigation was also carried out into the possible effect of the surrounding media on other, predominantly magnetic. The AWR models previously shown in Figure 5.10 and Figure 5.12 were re-investigated using air and polyolefin surrounds, to obtain the coupling coefficient (κ), resonant frequency (f_0), and quality factor (Q_0) variations shown in Figure 6.15. As can be seen, there is very little difference when the surrounding environment is altered from air to plastic, meaning that external dielectrics have little effect on magnetic parameters.

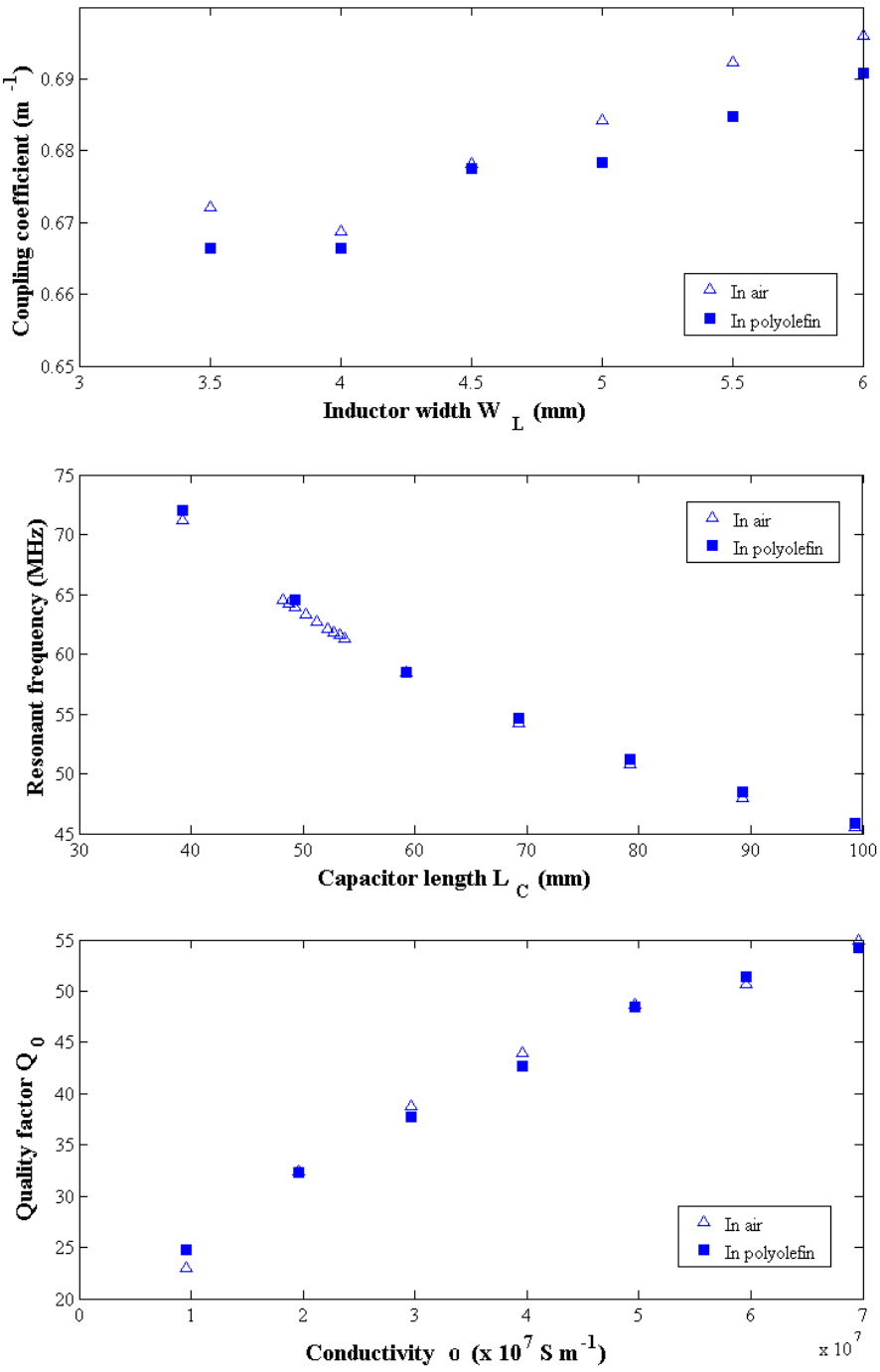


Figure 6.15 Variation of κ with W_L, f_0 with L_C, and Q_0 with σ for MR-safe cable in different environments (air and polyolefin)

6.6 Magnetic Decoupling

MR-safe cable is segmented into figure-of-eight-shaped resonant elements, to avoid coupling to external magnetic and electric fields. We now show how a simulation of magnetic decoupling can be carried out using AWR MWO. In this case, transducers generating suitable external magnetic fields are required. These can be provided using simple inductive loops. Two different coil sizes were investigated; a small coil (measuring 5 mm x 97 mm), and a large coil (18 mm x 100 mm), which is more homogeneous than the small coil. These coils were used to excite a single resonant element of the magneto-inductive cable as shown in Figure 6.16a and Figure 6.16b. The much smaller receiver coil (5 mm x 49 mm) on the right hand side is used to detect any current flowing as a result of magnetic induction. Two excitation patterns were considered, involving symmetric and asymmetric excitation for imitating common- and differential-mode current, respectively.

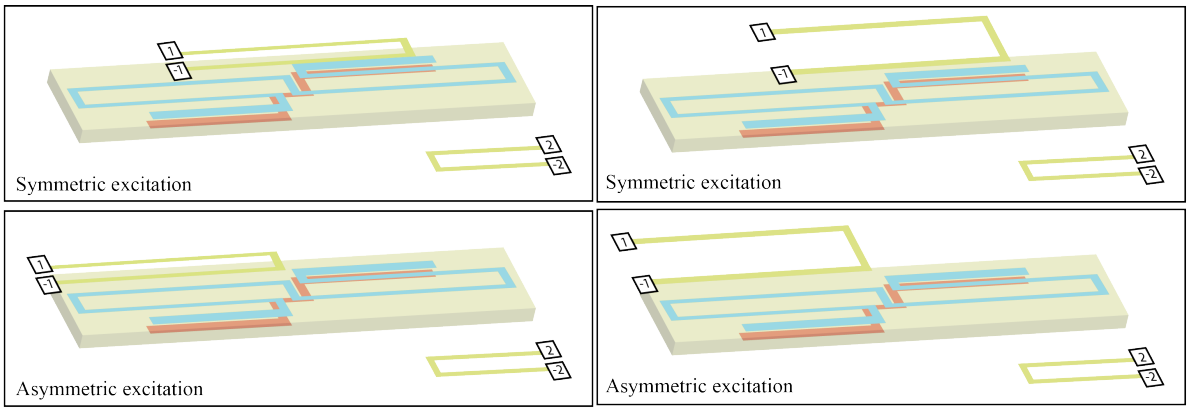
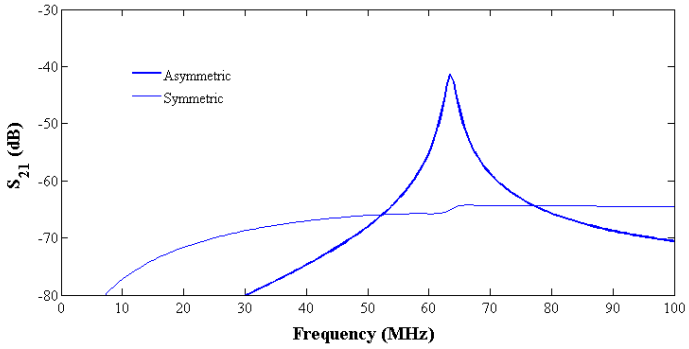


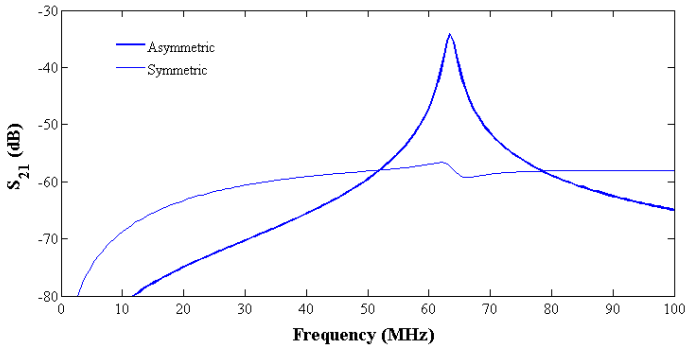
Figure 6.16 Simulation of magnetic decoupling (a) less uniform excitation (b) more uniform excitation

In symmetric case, the excitation coil was placed centrally above the figure-of-eight resonator to imitate the B_1 field that the MR scanner produces during excitation, and the frequency variations of the transmission S_{21} between the two external coils were simulated as shown in Figure 6.17. As can be seen, resonance at 63.85 MHz is largely absent, due to cancellation of the induction. In the asymmetric case, the excitation coil was shifted to the

left-hand side of the resonant element to imitate the signal detection from tissue. A strong resonance can now be seen, implying that cancellation of the induction do longer occurs. Similar results are clearly obtained from the two sizes of excitation coil, but the larger coil generates a larger signal.



(a)



(b)

Figure 6.17 Frequency variation of S_{21} predicted by AWR during magnetic excitation by (a) small and (b) large external coils

6.7 Electric Decoupling

We now show how a simulation of electric decoupling can be carried out using AWR MWO. In this case, transducers generating suitable external electric fields are required. These can again be provided using short dipoles. These were used to excite and detect signals on a 7-section length of MR-safe cable. For comparison, a similar simulation was also carried out using a uniform strip conductor of the same length (L_C ~ 797 mm), with 2 mm of width (W_C) and 35 μm thickness. In each case, the transmitting and receiving dipoles were placed 12.5 mm from the structures, at either end, as shown in Figure 6.18.

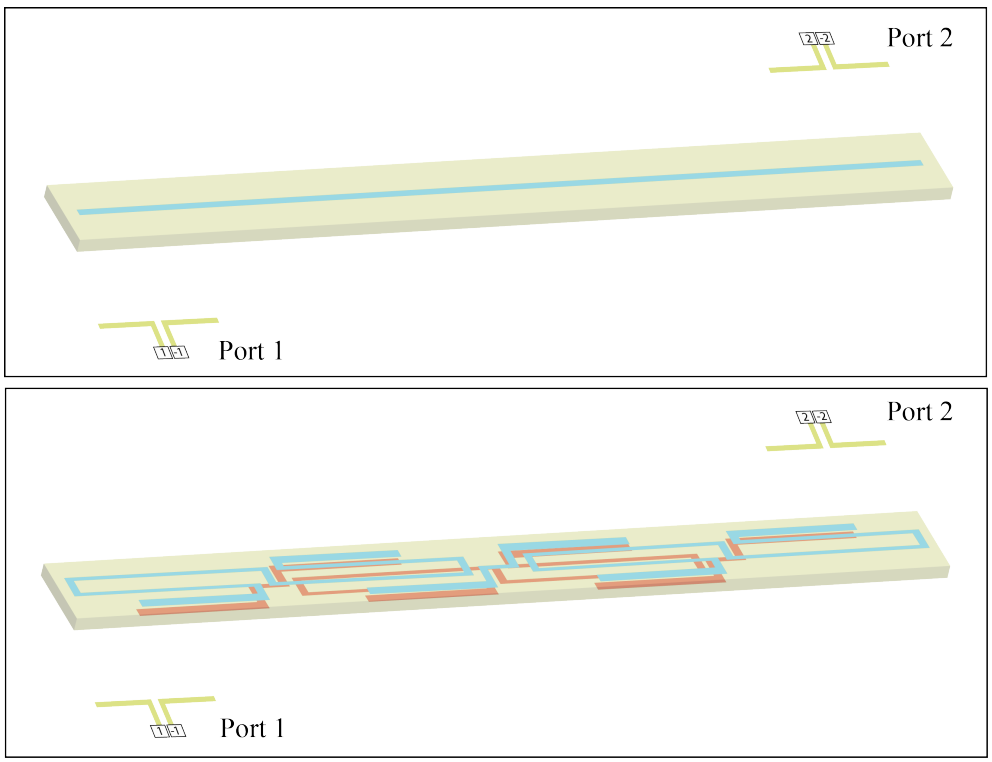


Figure 6.18 Simulation of electric decoupling models

Simulation were carried out under two test conditions; a) when the structures were fully immersed in tissue (structure 6.1.2 in Table 6.1), and b) when the structures were mounted on a polyolefin substrate and covered with a thick layer of tissue (structure 6.1.4 in Table 6.1). The electromagnetic properties of tissue are relative permittivity $\varepsilon_r = 77$ and conductivity $\sigma =$

0.45 S/m. Structures were evaluated a) with no upper cladding and b) with a 250 μm thick polyolefin heatshrink cladding.

The frequency variations of transmission S_{21} are obtained from the different arrangements as shown in Figure 6.19 below. For the undivided wire (Figure 6.19a), many resonances can be seen, extending to frequencies as low as 20 MHz (f_1 = 21.44 MHz) when fully immersed in tissue. The effect of the polyolefin heatshrink is to minimise the effective permittivity seen by the wire, and shift the lowest order resonance to the higher frequency of 90.8 MHz (estimated shifted lowest f_1 = 65.76 MHz when the extracted ε_r of 250 μm cladding is 8.19).

For the MR-safe cable, the effect of subdivision is, as expected, to raise the frequency of the lowest order resonance from 20 MHz (for strip conductor model) to 55.1 MHz as shown in Figure 6.19b. However, the raised lowest order resonance of the unclad system still lies below 63.85 MHz implying that heating might occur when 1.5 T MRI is operated. This is because the relatively large value of parasitic capacitance C_S obtained for the unclad cable limits the effect of subdivision. The 250 μm cladding then effectively helps to decrease the effective permittivity seen by conductors and to reduce C_S resulting in no resonant peak observed up to at least 150 MHz, and the attenuation in transmission compared with the undivided conductor is very substantial indeed. Because resonances never occur at the operating frequency, a strong surface wave cannot be formed. Therefore, the subdivided cable with a heat-shrink cladding provides extremely effective protection against external electric fields.

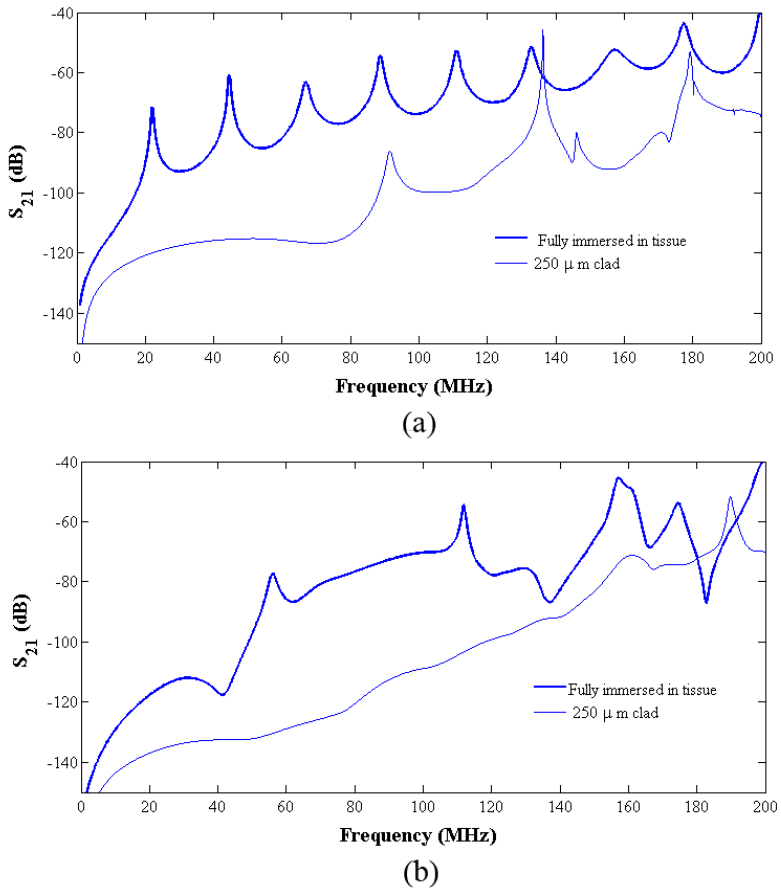


Figure 6.19 Frequency variation of transmission coefficient (S_{21}) predicted by AWR for (a) conductive wire and (b) MR-safe cable with electrical excitation

6.8 SAR Measurement

As previously described, MR safety is quantified by the specific absorption rate (SAR). In this Section, we use a numerical simulation to compare the likely SAR obtained using immersed MR-safe cable with that obtained using a linear conductive wire. For this work, CST Microwave Studio, which allows the post processing of SAR calculations, was used. The electromagnetic properties of the surround were fixed as $\varepsilon_r = 77$, $\sigma = 0.45$ S/m, $\rho = 1066$ kg/m^3 to mimic a 100 x 100 x 100 m^3 cubical volume of a saline solution within which any electrical test structures could be submerged.

Figure 6.20 shows the CST model for simulation of MR-safe cable. The E-field vector was arranged parallel to the cable axis, which itself lay along Z-axis. Similarly, the H-field vector was perpendicular to E-field, and hence lay along the Y-axis. This arrangement allowed the magnetic field to couple with resonant loops, and the electric field to couple to longitudinal conductors. In this geometry, the XY, XZ, and YZ planes correspond to the transverse, coronal, and sagittal planes used in MRI imaging. CST does not require an additional transducer to apply external fields, but allows these to be specified directly. Typically, the pulsed RF or B_1 field used for excitation in an MRI scanner is circularly polarized. However, for simplicity a Gaussian plane wave with 20 V/m electric field strength was used in this simulation. A similar model was constructed for excitation of a linear conductive wire (here take as a flat copper strip constructed on a 2 mm wide thin-film polyimide substrate).

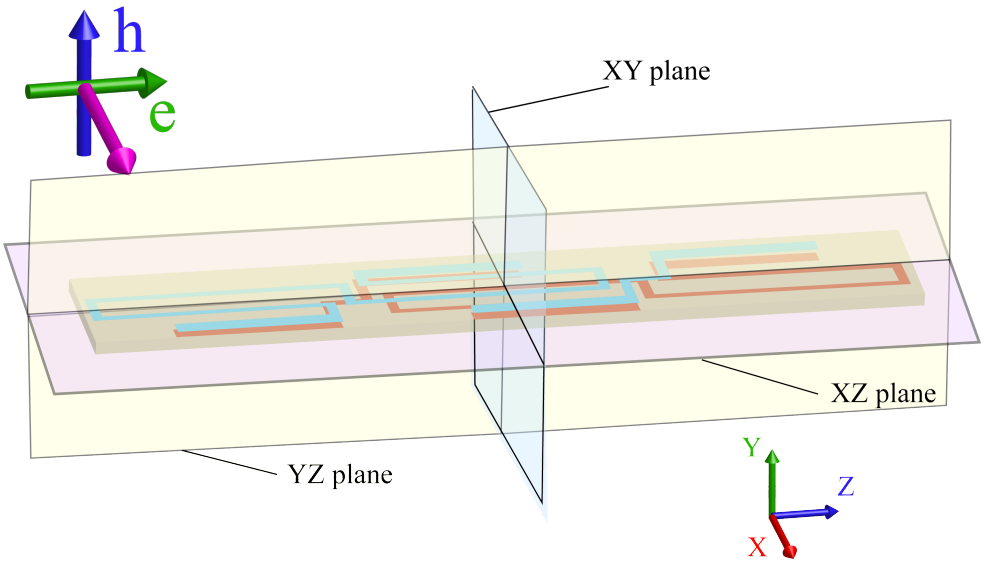


Figure 6.20 Excitation of MR-safe cable in the CST simulation

Even though the simulation above cannot provide an absolute estimate of the SAR as defined by the International standard (ASTM F2503 [135]), it still allows the relative performance of the two structures to be compared. For example, Figure 6.21 shows SAR maps for the conductive wire and the MR-safe cable over the XY, XZ, and YZ planes. The MR-safe cable clearly shows a significant reduction in SAR when compared to the continuous conductor. Particularly, a standing wave is formed in the continuous conductor,

and this effect is largely absent in the MR-safe cable. As a result, little heating can be observed in the MR-safe cable, especially at the ends (where the most dangerous effects occur on the continuous conductor).

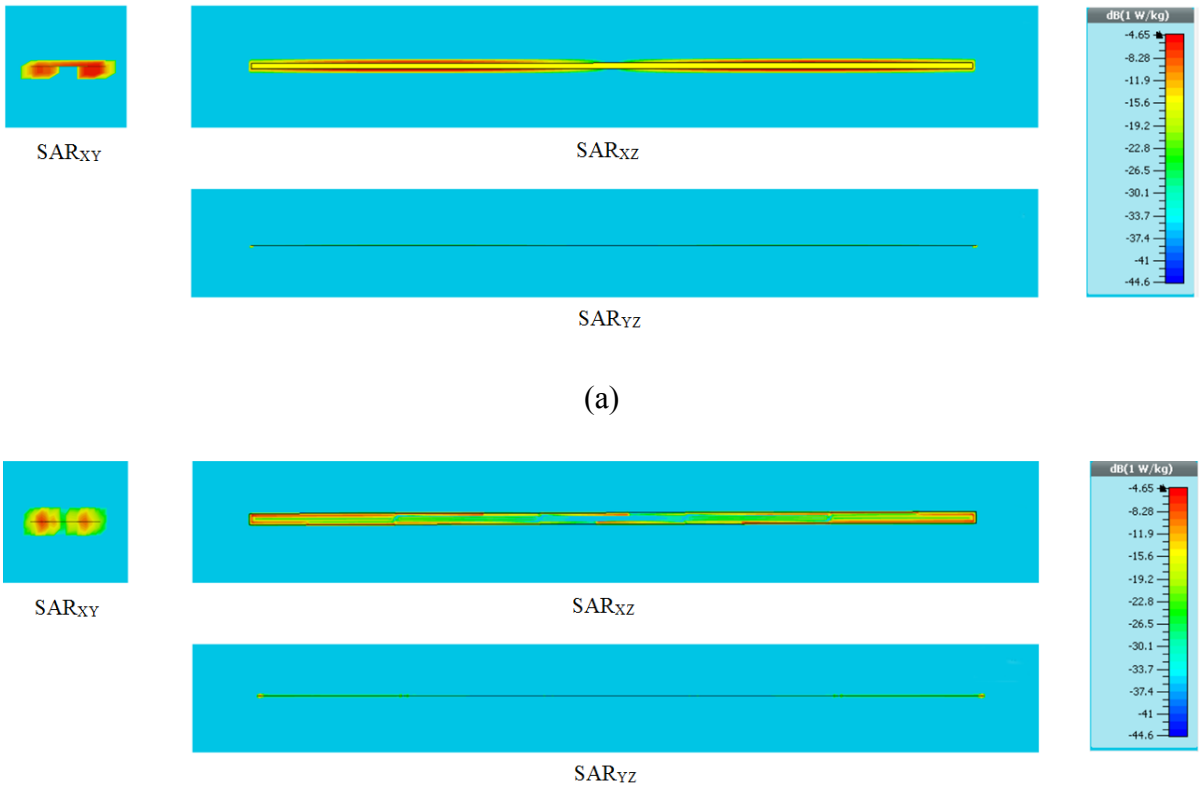


Figure 6.21 SAR maps on the XY, XZ, and YZ planes for (a) continuous conductor and (b) MR-safe cable

6.9 Numerical Simulation of Complete MR-safe Systems

The results above have shown that the plastic scaffold and the heatshrink tubing provide an effective isolation between the thin-film circuit and any surrounding tissue. Unfortunately, the most realistic structure (consisting of 7 layers of tissue and plastic shown in model 6.1.3 in Table 6.1) could not be modelled using the available computing hardware. The MR-safe

systems previously simulated (an MR-safe point-to-point link, shown in Figure 5.28, and an MR-safe resonant detector, shown in Figure 5.30) were therefore modelled again, this time as if the circuit were entirely embedded in polyolefin. To reduce computation time, the number of sections in the cable was reduced to 7.

Figure 6.22. compares the frequency variations of S_{11} and S_{21} obtained using different surrounding environments of a) air and b) polyolefin. As can be seen, the low-frequency magneto-inductive band is still retained even the surrounding environment is changed, demonstrating that the systems both have high tolerance to the surrounding medium. However, in each case, the effect of increasing the relative permittivity of the surrounding medium is to shift the unwanted high frequency propagation bands down towards lower frequency. Fortunately the effect is relatively small, and the spurious band does not interfere with propagation in the MI band.

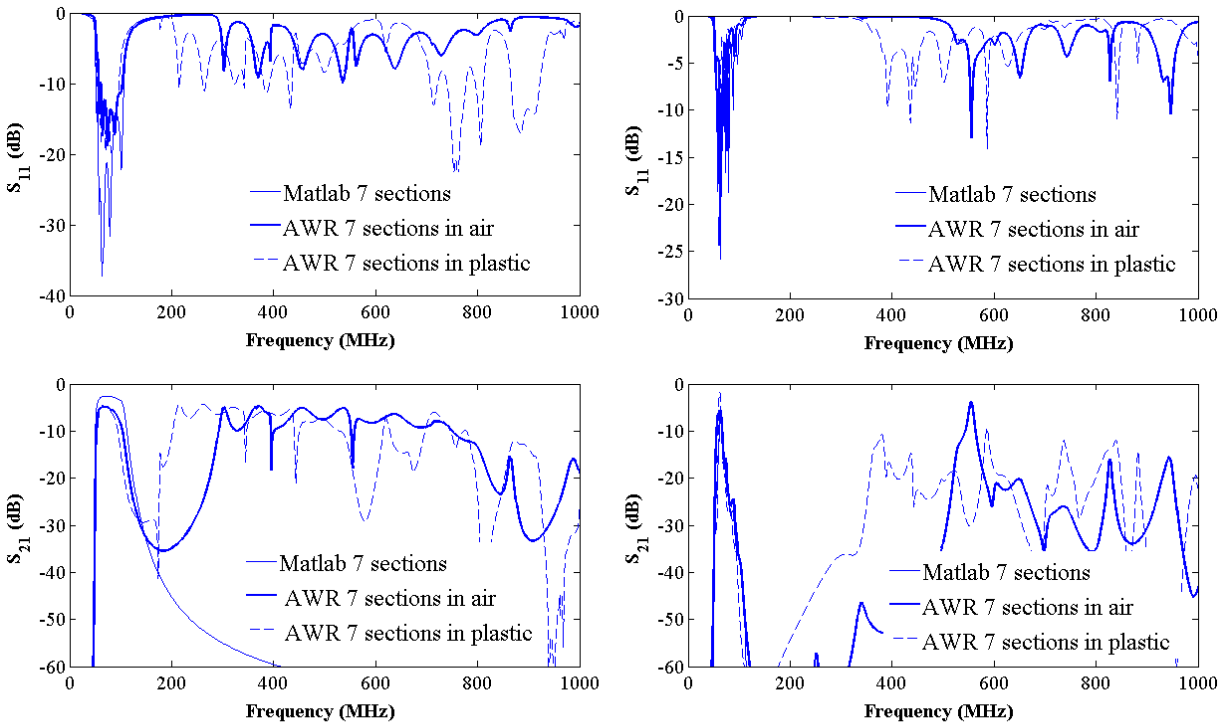


Figure 6.22 Frequency variation of S_{11} and S_{21}, as predicted by Matlab and AWR in air and plastic environments, for (a) point-to-point link, and (b) resonant detector with a MR-safe cable

6.10 Magnetic Resonance Imaging

To demonstrate the effectiveness of the decoupling from external fields, further ^{1}H magnetic resonance imaging experiments were carried out at St. Mary's Hospital using a 1.5 T GE Signa Excite clinical scanner, as described in [136]. A cuboid phantom, filled with a solution containing 3.37 g/L $NiCl_2.6H_2O$ and 2.4 g/L NaCl (with time constants T1 = 500-800 ms and T2 = 100-200 ms) was used, and the catheter with MR-safe detector integration was taped on top of the cuboid phantom in a spiral racetrack arrangement as shown in Figure 6.23. The excitation is from the system body coil, and signal detection is performed using different receiver; the body coil and the catheter coil. Imaging was carried out using a 2D spin echo sequence, with a repetition time TR = 520 ms, an echo time TE » 8.088 ms, an echo train length ETL = 2, 50% phase field of view and a 90^{o} flip angle.

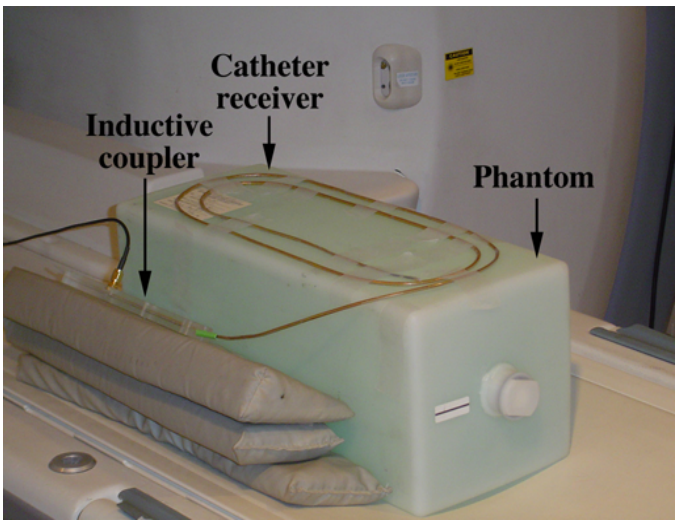


Figure 6.23 Arrangement for MR imaging [136]

Figure 6.24a shows a coronal slice image of the liquid below the catheter obtained using the body coil. The bright rectangular area represents the cuboid phantom, while the bright spiral 'shadow' represents an artefact due to incomplete decoupling of the catheter receiver. Compared with an entirely undecoupled system, the image brightness is reasonably uniform, indicating that a passive decoupling mechanism based on figure-of-eight-shaped resonant elements does indeed perform reasonably well.

Figure 6.24b shows a coronal slice image of the liquid below the catheter obtained using the body coil. The bright rectangular area represents the cuboid phantom, while the bright spiral 'shadow' represents an artefact due to incomplete decoupling of the catheter receiver. Compared with an entirely undecoupled system, the image brightness is reasonably uniform, indicating that a passive decoupling mechanism based on figure-of-eight-shaped resonant elements does indeed perform reasonably well.

Figure 6.24b shows the corresponding slice image obtained using the catheter coil. The image clearly depicts the layout of the catheter, which is represented as a set of bright rectangular lobes. Each bright lobe corresponds to one half of a figure-of-eight element and the dark spaces between the bright lobes correspond to the track crossover regions. The brightest regions are position 1, 3, and 4 representing the self-terminating detector at the tip of the catheter coil. The brightness is reduced after position 4 (which corresponds to the start of the cable) but climbs thereafter as signal is coupled into elements closer to the scanner input, due to the steadily reducing effect of propagation losses. These results confirm that the catheter images along its entire length, and causes minimal perturbation to the local magnetisation due to direct coupling effects.

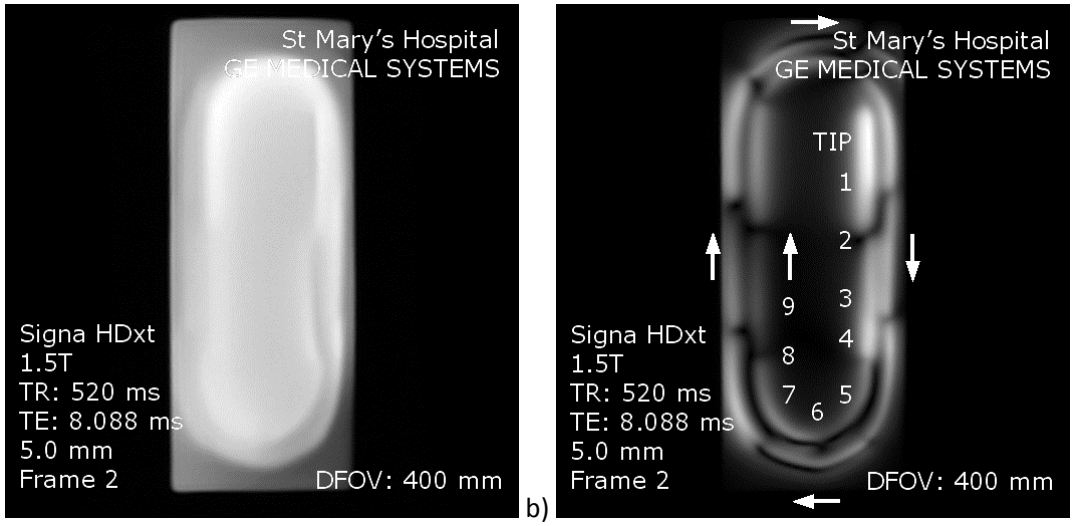


Figure 6.24 Coronal images of racetrack catheter on cuboid phantom obtained using (a) the body coil and (b) the catheter coil [136]

6.11 Discussion

The effect of realistic environments on MR-safe receiver systems (particularly, plastic substrate and sheath materials, and tissue surrounds) has been considered in detail using a full numerical model. An analytical model of cable subdivision has also been developed to provide an understanding of the effect of parasitic capacitance on cable segmentation. The effects of plastic surrounds on cable parameters such as effective permittivity (ε_r), parasitic capacitance (C_S), quality factor (Q_0), coupling coefficient (κ) have been clarified. It has been clearly shown that plastic sheath materials can be used to control affect ε_r and C_S, providing inherent patient safety even when the cable is fully immersed in tissue. The effectiveness of segmentation and the use of a figure-of-eight element shave on B_1 and E field decoupling have been confirmed. Post processing of data to yield a SAR estimation in CST MWO have been used to confirm the heating reduction obtained using MR-safe cable. Complete MR-safe systems have been simulated in a plastic environment, and it has been shown that a usable magneto-inductive band is still retained even the surrounding environment is changed. ^{1}H MR imaging has been carried out using experimental magneto-inductive catheters, and the effectiveness of B_1 decoupling has been confirmed.

6.12 Publication

The work presented here has resulted in this publication:

"Design of Magneto-Inductive Magnetic Resonance Imaging Catheters". by K. Segkhoonthod, R.R.A. Syms, I.R. Young, Sensors Journal, IEEE, 2014. **PP**(99): p. 1-1.

7. CONCLUSIONS AND FUTURE WORKS

7.1 Contributions

The aim of this thesis has been to investigate RF detection systems for a novel non-invasive diagnostic methodology provisionally named as non-surgical intrabiliary MRI, with the overall aim of improving early detection of cholangiocarcinoma, a deadly cancer of the ductal system between the liver and the duodenum. This imaging modality should provide superior soft-tissue contrast and improved signal-to-noise ratio, leading to the possibility of high-resolution imaging of the biliary ductal system using endoscopically delivered detectors.

Since the biopsy channel of the duodenoscope has very small diameter (ca 3 mm), and a 90^{o} turn is involved in cannulation of the ductal system, the entire receiver must be based on a long, smooth catheter. This constraint in turn requires that the electrical detection system must be based on a flexible thin film circuit that is entirely integrated and contains no protrusions or detachable components. These mechanical constraints, together with the required operating frequency of 63.8 MHz (for ^{1}H imaging at 1.5 T) and system impedance of 50 Ω influence the designs of the resonant detector used for signal detection and the transmission line used for signal transmission out of the body.

Four different thin-film structures have been simulated and studied, but just two embodiments of such a system can provide impedance matching as shown in Table 7.1. These second-generation receiver systems were then investigated in detail. Only one satisfies the additional constraints of mechanical flexibility and MR safety, the magneto-inductive MR-safe cable. This variant has already demonstrated excellent SNR in magnetic resonance imaging, and consequently is under further development. Its performance is mainly limited by the moderate Q-factor of the resonant elements. Partly this may be due to the low tan(d) of the dielectric material (Kapton), and there is scope to explore alternatives such as PTFE.

Table 7.1 Designs of the cable presented in this thesis

Structures on Thin-film	Impedance Matching (50 Ω)	MR-Safe	Mechanical Constraint (flexibility)	Q-factor
Microstrip	×	×	×	-
Coplanar Waveguide	×	×	×	-
Photonic Bandgap	✓	×	×	23
Magneto-inductive with figure-of-eight	✓	✓	✓	40

The first generation receiver system consisted of a flexible microcoil detector combined with a periodically patterned thin-film waveguide. Using this system, mechanical flexibility, resonant detection, low loss signal transmission and high signal to noise ratio during imaging were all demonstrated. Good agreement between analytical and numerical models was obtained, albeit with some small discrepancies in loss estimation arising from inaccuracy in the parameters of the thin-film materials specified by the manufacturer. Experimental components were shown to provide high-resolution MR images of resected porcine liver, encouraging the belief that systems of this type may indeed be suitable for internal MRI. However, since the system contained long, continuous conductors, the important issue of patient safety was not properly addressed.

The second generation of system combined a resonant detector with a different form of waveguide, magnetoinductive cable, with the aim of introducing inherent safety. Once again both circuits were fabricated in thin film form. The MI waveguide consisted of a set of magnetically coupled resonant elements with a figure-of-eight shape. The aim of segmentation was to prevent RF heating by electrical excitation of surface wave resonances during the excitation phase of MRI, while the purpose of the figure-of-eight layout was to prevent direct coupling to external magnetic fields during excitation while still responding during the detection phase.

Once again, the system was designed to satisfy the mechanical and electrical constraints involved in endoscopic delivery and use with a standard MRI scanner. Numerical simulations of point-to-point links and resonant detectors based on a variety of transducers were carried out, using corrected values for material properties. Dimensional parameters were adjusted to obtain good agreement with experiment. An analytical model was developed to determine the effectiveness of the segmentation. The effect of the surrounding media (a plastic support and heatshrink surround, and a tissue immersion medium) was studied in detail. It was found that the external environment mostly affects the effective permittivity of surface waves and a parasitic capacitance that tends to nullify the effect of segmentation. However, it was demonstrated that MR-safe cable can provide a significant reduction in RF-induced heating and SAR compared with similar systems based on continuous conductors, merely given a sufficient thickness of heatshrink tubing as an isolating medium.

^{1}H MR imaging was carried out at 1.5 T using a standard clinical scanner, using experimental thin-film circuits mounted on a plastic catheter with heat-shrink tubing. Images were obtained to demonstrate the effectiveness of the decoupling, and imaging both at the tip and along the length of the catheter receiver. These initial results clearly demonstrate the potential of magneto-inductive for internal MRI. The performance of components that have subsequently been developed at Imperial College is now increasing rapidly, and higher SNR has now been demonstrated at 1.5T and 3T than is achievable using a surface chest coil array, the best coil sets available locally for comparison.

7.2 Future Work

There are a number of directions for future work. Firstly, it is clear that the propagation losses of magneto-inductive cable are high. Consequently, because of thermal noise generated in the MR-safe cable, some of the SNR advantage obtained by placing the detector close to the target tissue is lost. Thermal noise is also introduced by tissue near the cable, between the resonant detector and input to the MRI scanner. The signal-to-noise ratio of the

entire detection system should therefore be carefully simulated, and efforts should be devoted to reduction of cable propagation loss.

Secondly, for a system intended for human clinical use, safety aspects still require further investigation. Detailed SAR simulations (for example, using the CST anatomical model HUGO) should be carried out to demonstrate that MR-safe cable fully complies with the standards of international organizations as FDA and ASTM. Animal testing should then be carried out to confirm the safety of immersion imaging. Finally, clinical testing should be carried out in humans to investigate whether motion artefacts negate the resolution enhancements expected from internal MRI.

APPENDIX A: Electromagnetic Analysis Software

To analyse coils and transmission lines above, the computational electromagnetics (CEM) software is introduced here. There are many commercial electromagnetic analysis software such as AWR Microwave Office (MWO), Computer Simulation Technology Microwave Studio (CST MWS), ANSYS HFSS, COMSOL Multiphysics, etc. These packages use different calculation methods such as the finite difference time domain (FDTD) method, the finite element method (FEM), the method of moments (MoM), and the finite integration technique (FIT) for low frequency applications. For high frequency applications, rather different methods such as the geometrical theory of diffraction (GTD), physical optics (PO), and shooting and bouncing rays (SBR) are used [137]. However, the MRI application considered here involves radio frequencies, so the former are more relevant. Each type of software makes use of Maxwell's electromagnetic equations to provide solutions.

The differential form of Maxwell's equations consists of a set of coupled vector equations relating the electromagnetic field quantities. For time-varying fields at angular frequency ω, these may be written in time-independent form as [137]:

$$\nabla \times \boldsymbol{E} = -\boldsymbol{M} - j\omega\mu\boldsymbol{H} \tag{A.1}$$

$$\nabla \times \mathbf{H} = \boldsymbol{J} + j\omega\epsilon\boldsymbol{E} \tag{A.2}$$

$$\nabla \cdot \boldsymbol{D} = q_e \tag{A.3}$$

$$\nabla \cdot \boldsymbol{B} = q_m \tag{A.4}$$

Here $\boldsymbol{E}$ and $\boldsymbol{H}$ are the electric and magnetic fields, $\boldsymbol{D}$ and $\boldsymbol{B}$ are the electric and magnetic flux densities, ε and μ are the permittivity and permeability, $\boldsymbol{J}$ and $\boldsymbol{M}$ are electric and magnetic current densities, and q_{e} and q_{m} are electric and magnetic charges. Together with these equations, the material equations $\boldsymbol{D} = \epsilon\boldsymbol{E}$ and $\boldsymbol{B} = \mu\boldsymbol{H}$ are required. Note that $\boldsymbol{M}$ and q_{m} are

not found in nature, but they are frequently used in numerical software to since their presence symmetrises the equations.

Similarly, the integral form (valid for arbitrary time variations) can be written as:

$$\oint_{\partial s} \vec{E} \cdot \overrightarrow{dl} = -\iint_{s} \frac{\partial \vec{B}}{\partial t} \cdot \overrightarrow{dS} \tag{A.5}$$

$$\oint_{\partial s} \vec{E} \cdot \overrightarrow{dl} = -\iint_{s} \frac{\partial \vec{B}}{\partial t} \cdot \overrightarrow{dS} \tag{A.6}$$

$$\oiint_{\partial V} \vec{D} \cdot \overrightarrow{dS} = \iiint_{V} \rho \, dV \tag{A.7}$$

$$\oiint_{\partial V} \vec{B} \cdot \overrightarrow{dS} = 0 \tag{A.8}$$

The approaches that use the integral equations are the method of moments (MoM), the fast multipole method (FMM), and the surface and volume integral equation (SIE and VIE) method. Similarly, the approaches that use the differential equations are the finite integral technique (FIT), the finite difference time domain (FDTD) method, and the finite element method (FEM). In this thesis, just two commercial products were used for EM analysis; AWR Microwave Office (MWO) and Computer Simulation Technology Microwave Studio (CST MWS) which use MoM and FIT, respectively.

Electromagnetic Solvers in Microwave Office (MWO)

In MWO, there are two well-known electromagnetic solvers: EM Sight and Axiem. Both are based on a modified spectral-domain MoM and can provide an analysis of an arbitrary multi-layered electrical structure using the integral forms of Maxwell's equations to obtain multi-

port scattering parameters for any specified planar structure [138], The differences between EM Sight and Axiem are described below.

Firstly, EM Sight requires a specific enclosure that is represented as a ground wall for analysis. However, Axiem has no need for a specific enclosure and instead assumes that the dielectric layers extend to infinity in the X-Y plane as shown in Figure A.1 below.

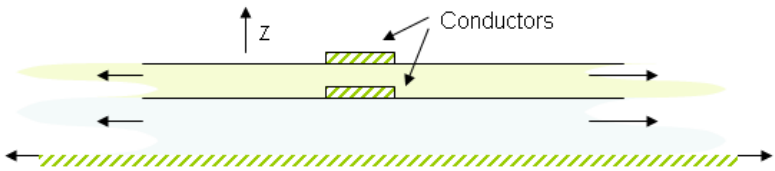


Figure A.1 Axiem's enclosure box environment [138]

Secondly, EM Sight only supports the edge port definition, while Axiem can support both edge and differential port types. As a result, Axiem is a better option for this twork, because the transmission lines in the later chapters require ports defined between layers and a modified ground plane. The edge ports are shown in Figure A.2a, and assume that the ports are directly connected to an ideal ground plane that cannot be modified. However, differential ports are shown in Figure A.2b, and allow an editable structure ground plane to be connected.

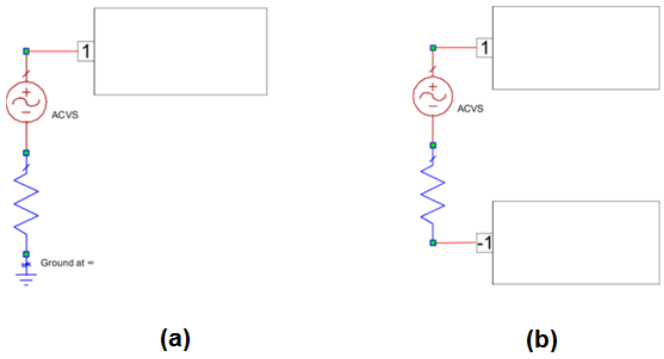


Figure A.2 Excitation ports provided by MWO (a) edge and (b) differential [138]

Another difference between EM Sight and Axiem is the meshing algorithm. Axiem offers an intelligent hybrid meshing that uses rectangles and triangles in an effective and efficient way as shown in Figure A.3, while EM Sight can only allows rectangle or staircase meshing [139]. All other important concerns such as boundary conditions and and material settings are stated in more detail in specific designs later on.

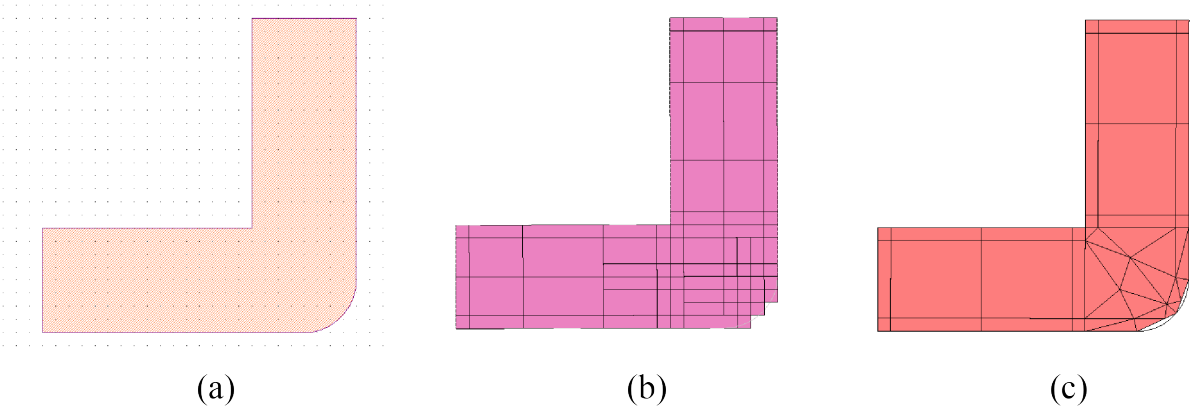


Figure A.3 Meshing mechanism of MWO (a) original (b) meshed by EM Sight (c) meshed by Axiem

Electromagnetic Solvers in Computer Simulation Technology (CST)

The Computer Simulation Technology Microwave Studio (CST MWS) is based on the FIT method derived from Maxwell's differential equations. FIT is not suited to the open-environment problem because it requires a discretization of the entire space, which often requires very considerable computational resource (CPU and memory). CST MWS offers many solvers (a transient simulator, frequency domain simulator, integral equation simulator, multilayer simulator, asymptotic simulator, eigenmode simulator etc). to solve different 3D electromagnetic problems. The boundary condition in CST is a specific enclosure that must be declared. CST MWS can generate scattering parameters, and also provide a full field analysis. In this thesis, the transient or time-domain solver is chosen to analyse the post-

processing results such as *E* and *H* fields, and to perform Specific Absorption Rate (*SAR*) calculation or simulations of RF heating described in a later chapter.

CST MWS works differently from MWO, for example, the samples are constructed on a full Cartesian grid, not as a planar-stacked arrangement as in MWO. Port definitions in CST may also e chosen for many different applications, for example, as waveguide ports, discrete ports, and plane wave ports. For example, to calculate the *SAR*, a plane wave port that imitates a RF transmitter in a MRI scanner, can be used. CST MWS provides three different mesh types; hexahedron, tetrahedron, and surface meshing as shown below.

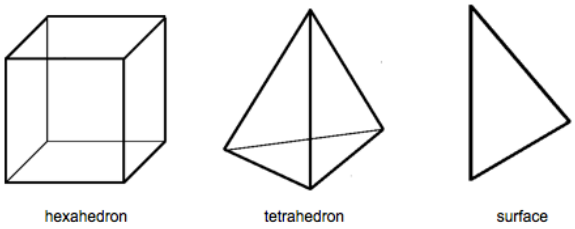


Figure A.4 Meshing types in CST MWS

MWO requires considerably less computer resources than CST Microwave Studio. Since it can run much faster, it is therefore used for all calculations involving determination of simple properties of structures with a complex layout topology (for example, scattering parameters). However, CST is still required for aspects requiring a full field analysis (for example, as in Chapter 6).

APPENDIX B: Measurement of tan δ

The dissipation factor or loss tangent (*tan δ*) of 0.0018 taken from the technical datasheet for Dupont Kapton HN Polyimide [120] results in a major disagreement in the experimental and theoretical measurements of loss in thin-film MR-safe devices. The most likely explanation is that the values of dielectric constant (ε_r) and *tan δ* are obtained using the ASTM D-150-92 Standard Test Method for AC Loss Characteristics and Permittivity of Solid Electrical Insulation [140], which uses the specific conditions of 23°C, 1 kHz frequency and 50% humidity. These conditions are not realistic for the much higher frequencies used in MRI. We therefore now describe a method of extracting *tan δ* under the appropriate conditions for ^{1}H imaging at 1.5 T.

Dielectric loss in a real capacitor (C_{real}) can be described in terms of an equivalent series resistance (*ESR*) connected in series with an ideal capacitance (C_{ideal}) as shown in Figure B.1 below [141, 142].

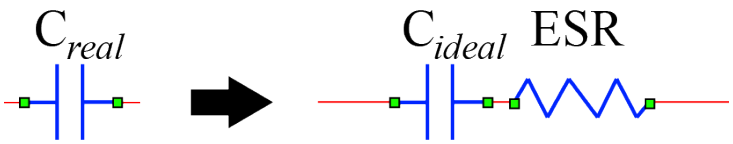


Figure B.1 Non-ideal capacitor modelled as an ideal capacitor connected in series with ESR

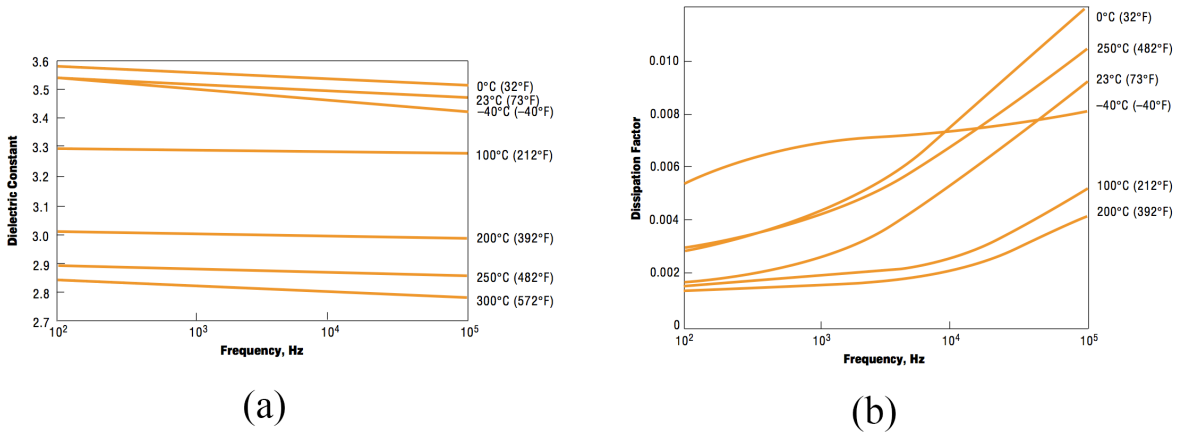
The dissipation factor is directly proportional to the *ESR* as shown in Equations (B.**1**) and (B.**2**), so that *tan δ* and *ESR* mainly depend on the angular frequency (ω).

$$ESR = \frac{\sigma}{\varepsilon\omega^2 C_{ideal}} \tag{B.1}$$

$$tan\,\delta = \omega C_{ideal} \cdot ESR = \frac{\sigma}{\varepsilon\omega} = \frac{1}{Q} \tag{B.2}$$

Here ε is the lossless permittivity and σ is the bulk conductivity of the dielectric and Q is the quality factor.

Figure B.2 shows measured variations of ε_r and *tan* δ with frequency at different temperatures, for 25 μm thick Dupont Kapton HN film, obtained from the manufacturer's datasheet [59]. As can be seen, the relative permittivity is almost constant, and appears mainly to be affected by temperature. However, the dissipation factor also clearly varies strongly with frequency, increasing rapidly above around 10 kHz.



(a) (b)

Figure B.2 Frequency dependence of (a) dielectric constant (b) dissipation factor [59]

Figure B.3 shows other factors such as humidity and temperature that affect ε_r and *tan* δ [59]. As can be seen, the value of 3.5 for the relative dielectric constant provided in the data sheet is still relevant for the MRI application. However, the value of *tan* δ varies not only with temperature and frequency, but also with humidity. Further experiments are therefore required to determine a suitable value.

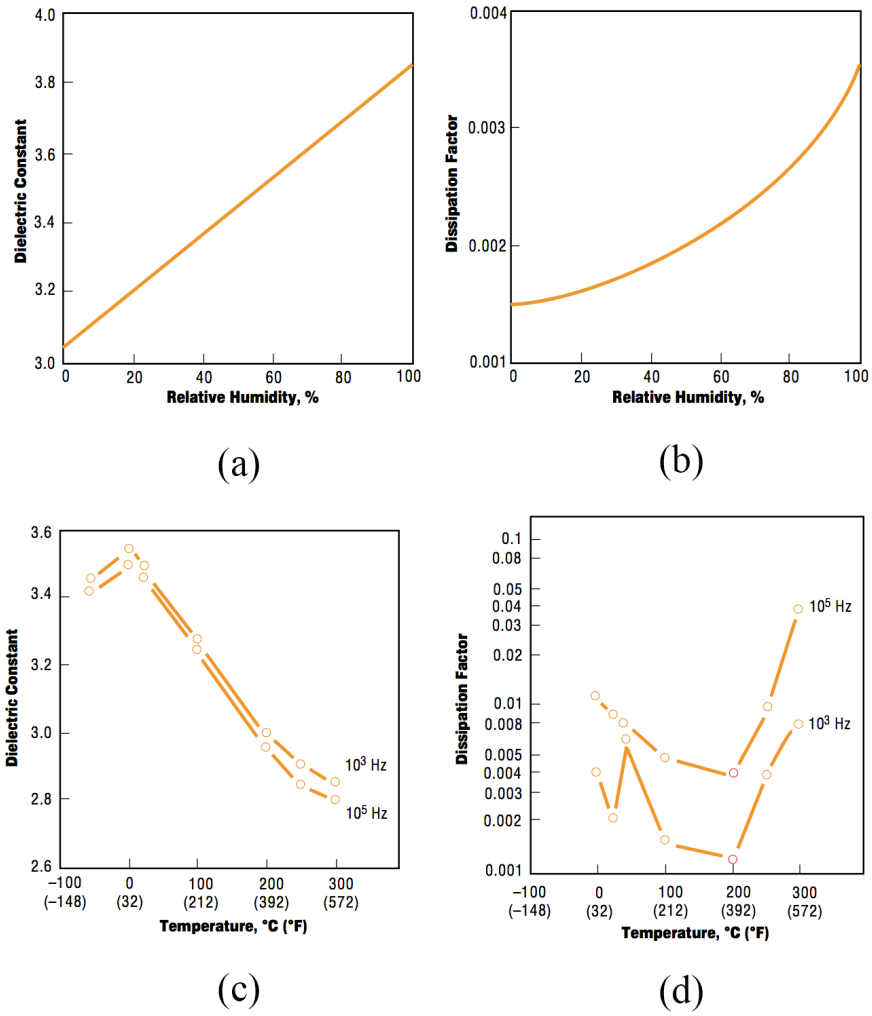


Figure B.3 Effect of humidity on the values of (a) dielectric constant (b) dissipation factor , and effect of temperature on the values of (c) dielectric constant (d) dissipation factor [59]

Several methods can be used measure the dissipation factor, such as the Schering bridge, the unbalanced bridge, and polarization/depolarization current (PDC) [143, 144]. However, for the RF application here, we chose a simpler method based on a L-C resonator consisting of a lossy inductor and a lossy capacitor with a Kapton interlayer as shown in Figure B.4 below. Again, R_L and R_C are represented as losses or *ESR* in non-ideal inductor and capacitor.

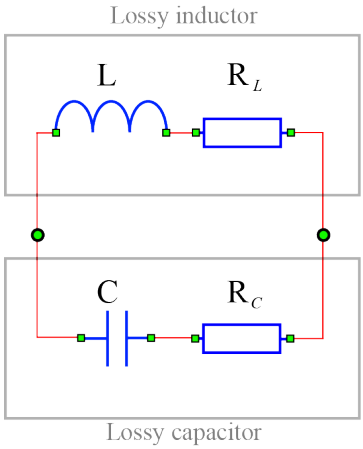


Figure B.4 L-C resonator using a piece of high quality wire and a Kapton-based capacitor

The Q-factor that we want to measure can be simply expressed as:

$$Q = \frac{\omega L}{R} \tag{B.3}$$

Where $R = R_L + R_C$ as shown in Figure B.4. If $R_C \gg R_L$ (which means using a large diameter of wire, so R_L can effectively be neglected), then Equation (B.**3**) simplifies to:

$$Q \approx \frac{\omega L}{R_C} \tag{B.4}$$

Since the resonance of an L-C resonator can also be expressed as $\omega^2 = \frac{1}{LC}$. Equation (B.**4**) can also be written as:

$$Q = \frac{1}{\omega C R_C} \tag{B.5}$$

In fact, the *ESR* in Equation (B.**2**) and the resistance in Equation (B.**5**) have the same meaning. Combining Equations (B.**2**) and (B.**5**), we then get:

$$Q = \frac{1}{tan\,\delta} \tag{B.6}$$

Consequently, *tan* δ may be found directly from simple measurements of Q-factor, which may easily be carried out using a network analyser.

The L-C resonator in Figure B.4 can be physically constructed using a rectangular area of copper-clad polyimide taken from the experimental PCB as a capacitor, and a loop wire as inductor. Using this approach, a variety of resonators with different resonant frequencies over the range 30 MHz – 130 MHz were constructed as shown in Figure B.5.



Figure B.5 Experimental L-C resonators for measuring Q-factor and dissipation factor

The resonant frequencies and Q-factors of these devices were experimentally measured using a network analyser, using very weak inductively coupled probes for signal injection and

detection. Figure B.6 shows the resulting variation of *tan δ* with resonant frequency. Over the frequency range shown, *tan δ* is highly consistant, with an average value of 0.006.

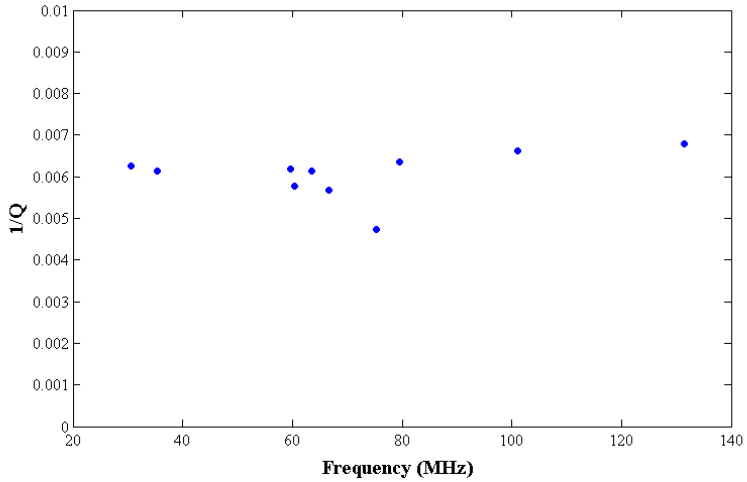
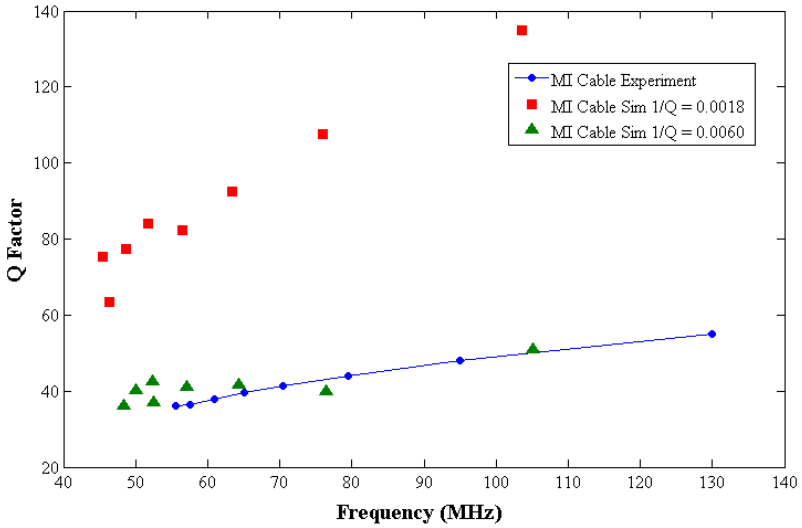
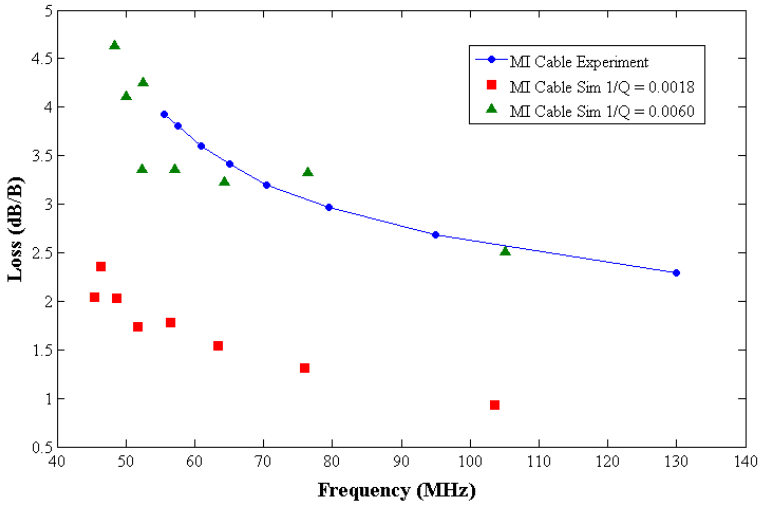


Figure B.6 Experimental variation of *tan δ* with frequency

The new value of *tan δ* (0.006) was verified by simulating the behaviour of a single resonant element using AWR MWO. For comparison, the simulations were repeated using the manufacturer's value (0.0018). The simulation results were compared with experimental data for the frequency variation of Q-factor and loss in experimental MI cables taken from [119], as shown in Figure B.7a and Figure B.7b, respectively. As can be seen, the models with *tan δ* = 0.006 agree with the experimental data considerably better than those with *tan δ* = 0.0018. The former value was therefore adopted for all later simulations in this thesis.



(a)



(b)

Figure B.7 Comparison of experimental and numerical results obtained with tan δ = 0.0060 and 0.0018: (a) variation of Q factor with frequency (b) variation of loss with frequency

APPENDIX C: MATLAB Codes in the Study of MR-Safe Scattering Parameters Estimation

This programme is developed by Prof. Richard Syms, which this thesis used for comparing to the simulation data.

```
clear all;
clc;
close all;
format long

%Program to calculate transmission through MI detector system;
%With varying frequency - either transducer;

%g = 1.6 - two-turn transducer; g=1 - std transducer; g=0.5 - broadband
transducer;
g=0.5;
%g=1;
%g=0.5;
%Set parameters;
nmax=1000;
fmin=1e6;
fmax=1000e6;
Z0=50;
Z0M=38.35;
kappa=0.6849;
Q0=40;
f0=63.6e6;
w0=2*pi*f0;
M=Z0M/w0;
L=2*M/kappa;
C=1/(w0*w0*L);
R=w0*L/Q0;
M1=sqrt(Z0*Z0M)/w0;
M2=sqrt(R*Z0M)/w0;
a=0.1;

nel=11;
%Set=electrical arrays for cable;
ZL=zeros(nel,nel);
VL=zeros(nel,1);
IL=zeros(nel,1);
%Set output arrays for cable;
freqL=zeros(nmax);
s11L=zeros(nmax);
s21L=zeros(nmax);
tL=zeros(nmax);

%Calculate response of cable;
for n = 1:nmax;
    f=fmin+(fmax-fmin)*n/nmax;
```

```
    w=2*pi*f;
    freqL(n)=f/1e6;

    for i=1:nel;
        ZL(i,i)=R + 1j*w*L - 1j/(w*C);
        for j=1:nel;
            if abs(i-j)==1;
                ZL(i,j)=1j*w*M;
            end;
        end;
    end;
    %Final elements;
    ZL(1,1)=R + 1j*w*L*g - 1j/(w*C/g) + Z0;
    ZL(nel,nel)=R + 1j*w*L*g - 1j/(w*C/g) + Z0;
    ZL(1,2)=1j*w*M1;
    ZL(2,1)=1j*w*M1;
    ZL(nel-1,nel)=1j*w*M1;
    ZL(nel,nel-1)=1j*w*M1;

    VS=1;
    VL(1,1)=VS;
    IL=ZL\VL;
    Iin=IL(1,1);
    Iout=IL(nel,1);
    RV=1-2*Iin*Z0/VS;
    TV=(Iout*Z0/(VS-Iin*Z0))*(1+RV);
    s11L(n)=10*log10(RV*conj(RV));
    s21L(n)=10*log10(TV*conj(TV));
    tL(n)=10*log10(RV*conj(RV)+TV*conj(TV));
end;

nel=16;
%Set electrical arrays for detector;
ZD=zeros(nel,nel);
VD=zeros(nel,1);
ID=zeros(nel,1);
%Set output arrays for detector;
freqD=zeros(nmax);
s11D=zeros(nmax);
s21D=zeros(nmax);
tD=zeros(nmax);

%Calculate response of detector;
for n=1:nmax;
    f=fmin+(fmax-fmin)*n/nmax;
    w=2*pi*f;
    freqD(n)=f/1e6;

    for i=1:nel;
        ZD(i,i)=R + 1j*w*L - 1j/(w*C);
        for j=1:nel;
            if abs(i-j)==1;
                ZD(i,j)=1j*w*M;
            end;
        end;
    end;
    %Set initial and final elements;
    ZD(1,1)=R + 1j*w*L*g - 1j/(w*C/g) + Z0;
    ZD(1,2)=1j*w*M1;
```

```
    ZD(2,1)=1j*w*M1;
    ZD(nel-1,nel)=1j*w*M2;
    ZD(nel,nel-1)=1j*w*M2;

    VS=1;
    VD(1,1)=VS;
    ID=ZD\VD;
    Iin=ID(1,1);
    Iout=ID(nel,1);
    Vin=VS-Iin*Z0;
    RV=1-2*Iin*Z0/VS;
    I0=Iin/(1-RV);
    s11D(n)=10*log10(RV*conj(RV));
    s21D(n)=10*log10(Iout*conj(Iout)*R/(I0*conj(I0)*Z0));
    tD(n)=10*log10(RV*conj(RV)+TV*conj(TV));
end;

%Plot response of cable;
figure;
p=plot(freqL,s11L);
set(p,'Color','black','LineWidth',2);
hold on;
p=plot(freqL,s21L);
set(p,'Color','blue','LineWidth',2);
hold off;
set(gca,'Fontname','Times','FontSize',20);
xlabel('Frequency (MHz)','Fontsize',20)
ylabel('Efficiency (dB)','Fontsize',20)
axis([fmin/1e6 fmax/1e6 -50 10]);
title('Cable: Black - reflection; blue -
transmission','Fontname','Times','Fontsize',20);

%Plot response of detector;
figure;
p=plot(freqD,s11D);
set(p,'Color','black','LineWidth',2);
hold on;
p=plot(freqD,s21D);
set(p,'Color','blue','LineWidth',2);
hold off;
set(gca,'Fontname','Times','FontSize',20);
xlabel('Frequency (MHz)','Fontname','Times','Fontsize',20)
ylabel('Efficiency (dB)','Fontname','Times','Fontsize',20)
axis([fmin/1e6 fmax/1e6 -50 10]);
title('Detector: Black - reflection; blue -
transmission','Fontname','Times','Fontsize',20);
```

References

1. Patel, T., *Cholangiocarcinoma.* Nat Clin Pract Gastroenterol Hepatol, 2006. **3**(1): p. 33-42.

2. Khan, S.A., et al., *Cholangiocarcinoma.* Lancet, 2005. **366**(9493): p. 1303-14.

3. Anderson, C.D., et al., *Diagnosis and treatment of cholangiocarcinoma.* Oncologist, 2004. **9**(1): p. 43-57.

4. Shin, H.R., et al., *Epidemiology of cholangiocarcinoma: an update focusing on risk factors.* Cancer Sci, 2010. **101**(3): p. 579-85.

5. Sripa, B., et al., *Opisthorchiasis and Opisthorchis-associated cholangiocarcinoma in Thailand and Laos.* Acta Tropica, 2011. **120, Supplement 1**(0): p. S158-S168.

6. Taylor-Robinson, S.D., et al., *Increase in mortality rates from intrahepatic cholangiocarcinoma in England and Wales 1968-1998.* Gut, 2001. **48**(6): p. 816-820.

7. Unknown. *ERCP*. 2010 17 Febuary 2010 [cited 2010 30, August]; .]. Available from: http://www.patient.co.uk/health/ERCP.htm.

8. Modric, J., *Gallbladder Tests: Ultrasound, CT, HIDA Scan, ERCP*. healthhype.com.

9. Pettegrew, J.W., *NMR : principles and applications to biomedical research*. 1989, Berlin: Springer.

10. Slichter, C.P., *Principles of magnetic resonance*. 3rd enl. and updated ed. Springer series in solid-state sciences. 1990, Berlin ; London: Springer.

11. Technology, H.K.S.o.M.R.I. *Introductory MRI Course I.* [cited 2010 30, August]; Available from: http://www.hksmrit.org.hk/course_1.htm.

12. McRobbie, D.W., *MRI from picture to proton*. 2nd ed. 2007, Cambridge, UK.: Cambridge University Press. xii, 394 p., [8] p. of plates.

13. Coyne, K. *MRI: A Guided Tour*. [cited 2010 30, August]; Available from: http://www.magnet.fsu.edu/education/tutorials/magnetacademy/mri/.

14. Hoult, D.I. and R.E. Richards, *The signal-to-noise ratio of the nuclear magnetic resonance experiment.* Journal of Magnetic Resonance (1969), 1976. **24**(1): p. 71-85.

15. AILab Co., L., *MRI system Magfinder II*. medonica.

16. Adamek, H.E., et al., *A prospective evaluation of magnetic resonance cholangiopancreatography in patients with suspected bile duct obstruction.* Gut, 1998. **43**(5): p. 680-3.

17. Manfredi, R., et al., *MR imaging and MRCP of hilar cholangiocarcinoma.* Abdom Imaging, 2003. **28**(3): p. 319-25.

18. Arepally, A., et al., *Hilar cholangiocarcinoma: staging with intrabiliary MRI.* AJR Am J Roentgenol, 2004. **183**(4): p. 1071-4.

19. Weiss, C.R., et al., *Intrabiliary MR Imaging: Assessment of Biliary Obstruction with Use of an Intraluminal MR Receiver Coil.* Journal of Vascular and Interventional Radiology, 2006. **17**(5): p. 845-853.

20. Lee, R.F., R.O. Giaquinto, and C.J. Hardy, *Coupling and decoupling theory and its application to the MRI phased array.* Magn Reson Med, 2002. **48**(1): p. 203-13.

21. Hurst, G.C., et al., *Intravascular (catheter) NMR receiver probe: preliminary design analysis and application to canine iliofemoral imaging.* Magn Reson Med, 1992. **24**(2): p. 343-57.

22. Atalar, E., et al., *High resolution intravascular MRI and MRS by using a catheter receiver coil.* Magn Reson Med, 1996. **36**(4): p. 596-605.

23. Ocali, O. and E. Atalar, *Intravascular magnetic resonance imaging using a loopless catheter antenna.* Magn Reson Med, 1997. **37**(1): p. 112-8.

24. Worthley, S.G., et al., *A novel nonobstructive intravascular MRI coil: in vivo imaging of experimental atherosclerosis.* Arterioscler Thromb Vasc Biol, 2003. **23**(2): p. 346-50.

25. Zuehlsdorff, S., et al., *MR coil design for simultaneous tip tracking and curvature delineation of a catheter.* Magn Reson Med, 2004. **52**(1): p. 214-8.

26. Hillenbrand, C.M., et al., *Active device tracking and high-resolution intravascular MRI using a novel catheter-based, opposed-solenoid phased array coil.* Magn Reson Med, 2004. **51**(4): p. 668-75.

27. McCann, C. and M.D. Sherar, *Development of a novel loosely wound helical coil for interstitial radiofrequency thermal therapy.* Physics in Medicine and Biology, 2006. **51**(15): p. 3835-3850.

28. McCann, C. and M.D. Sherar, *The use of a dispersive ground electrode with a loosely wound helical coil for interstitial radiofrequency thermal therapy.* Physics in Medicine and Biology, 2006. **51**(15): p. 3851-3863.

29. Cabuy, E. *Energy-Based Therapies for Cancer Treatment*. 2011.

30. Takemura, Y., *Resonant circuit as magnetic device for cancer therapy.* 1st International Symposium on Spintronic Devices and Commercialization (Issdc2010), 2011. **263**.

31. Peck, T.L., et al., *NMR microspectroscopy using 100 microns planar RF coils fabricated on gallium arsenide substrates.* IEEE Trans Biomed Eng, 1994. **41**(7): p. 706-9.

32. Stocker, J.E., et al., *Nanoliter volume, high-resolution NMR microspectroscopy using a 60-micron planar microcoil.* IEEE Trans Biomed Eng, 1997. **44**(11): p. 1122-7.

33. Neagu, C.R., et al., *Characterization of a planar microcoil for implantable microsystems.* Sensors and Actuators A: Physical, 1997. **62**(1–3): p. 599-611.

34. Renaud, L., et al., *Implantable planar rf microcoils for NMR microspectroscopy.* Sensors and Actuators A: Physical, 2002. **99**(3): p. 244-248.

35. Dechow, J., et al., *Fabrication of NMR — Microsensors for nanoliter sample volumes.* Microelectronic Engineering, 2000. **53**(1–4): p. 517-519.

36. Massin, C., et al., *High-Q factor RF planar microcoils for micro-scale NMR spectroscopy.* Sensors and Actuators A: Physical, 2002. **97–98**(0): p. 280-288.

37. Coutrot, A.L., et al., *Copper micromoulding process for NMR microinductors realization.* Sensors and Actuators A: Physical, 2002. **99**(1–2): p. 49-54.

38. Uelzen, T., et al., *Mechanical and electrical properties of electroplated copper for MR-imaging coils.* Microsyst. Technol., 2006. **12**(4): p. 343-351.

39. Woytasik, M., et al., *Characterization of flexible RF microcoils dedicated to local MRI.* Microsystem Technologies, 2007. **13**(11): p. 1575-1580.

40. Schaefers, G., *Testing MR safety and compatibility.* IEEE Engineering in Medicine and Biology Magazine, 2008. **27**(3): p. 23-27.

41. Ahmad, M.M., et al., *Catheter-based flexible microcoil RF detectors for internal magnetic resonance imaging.* Journal of Micromechanics and Microengineering, 2009. **19**(7).

42. Liboff, R.L. and G.C. Dalman, *Transmission lines, waveguides and Smith charts*. 1985, New York London ;: Macmillan ; Collier Macmillan.

43. Schwarz, S.E., *Electromagnetics for engineers* 1990, Philadilphia: Saunders College Publishing

44. Syms, R.R.A., *Chapter 4: Transmission Line Devices*. 2010, Imperial College London: Imperial College London.

45. Syms, R.R.A., et al., *Thin-Film Detector System for Internal Magnetic Resonance Imaging.* Sensors and Actuators a-Physical, 2010. **163**(1): p. 15-24.

46. Wheeler, H.A., *Transmission-Line Properties of a Strip on a Dielectric Sheet on a Plane.* Ieee Transactions on Microwave Theory and Techniques, 1977. **25**(8): p. 631-647.

47. Wheeler, H.A., *Transmission-Line Properties of a Strip Line between Parallel Planes.* Ieee Transactions on Microwave Theory and Techniques, 1978. **26**(11): p. 866-876.

48. Edwards, T.C., *Fundations for microstrip circuit design*. 2nd ed. 1991: Chichester: Wiley.

49. Wen, C.P., *Coplanar Waveguide: A Surface Strip Transmission Line Suitable for Nonreciprocal Gyromagnetic Device Applications.* Microwave Theory and Techniques, IEEE Transactions on, 1969. **17**(12): p. 1087-1090.

50. Radisic, V., et al., *Novel 2-D photonic bandgap structure for microstrip lines.* Ieee Microwave and Guided Wave Letters, 1998. **8**(2): p. 69-71.

51. Radisic, V., Y.X. Qian, and T. Itoh, *Broad-band power amplifier using dielectric photonic bandgap structure.* Ieee Microwave and Guided Wave Letters, 1998. **8**(1): p. 13-14.

52. Rumsey, I., M. Piket-May, and P.K. Kelly, *Photonic bandgap structures used as filters in microstrip circuits.* Ieee Microwave and Guided Wave Letters, 1998. **8**(10): p. 336-338.

53. Bera, S.C., et al., *A novel PBG structure for filter application.* Microwave and Optical Technology Letters, 2006. **48**(1): p. 188-190.

54. Chen, W.L., et al., *A novel wide stopband PBG structure with fractal features and its application to the design of microstrip low-pass filter.* 2006 7th International Symposium on Antennas, Propagation and EM Theory, Vols 1 and 2, Proceedings, 2006: p. 292-295.

55. Kroll, N., D.R. Smith, and S. Schultz, *Photonic Band-Gap Structures - a New Approach to Accelerator Cavities.* Advanced Accelerator Concepts, 1993. **279**: p. 197-211.

56. Pang, Y.B. and B.X. Gao, *Novel 1-D photonic bandgap structure and resonator for microstrip circuits.* 2002 3rd International Conference on Microwave and Millimeter Wave Technology Proceedings, 2002: p. 1059-1062.

57. Zhang, G.H., et al., *A. novel PBG structure for microstrip lines.* 2002 3rd International Conference on Microwave and Millimeter Wave Technology Proceedings, 2002: p. 1040-1042.

58. Brillouin, L., *Wave propagation in periodic structures : electric filters and crystal lattices*. 2nd ed. International series in pure and applied physics. 1953, New York ; London: Dover.

59. Dupont *Summary of Kapton Properties*.

60. Shellock, F.G. and E. Kanal, *Magnetic resonance : bioeffects, safety, and patient management*. 2nd ed. 1996, Philadelphia: Lippincott-Raven. xi,342p.

61. Shellock, F.G. and E. Kanal, *Burns associated with the use of monitoring equipment during MR procedures.* Jmri-Journal of Magnetic Resonance Imaging, 1996. **6**(1): p. 271-272.

62. Wildermuth, S., et al., *MR-guided percutaneous angioplasty: assessment of tracking safety, catheter handling and functionality.* Cardiovasc Intervent Radiol, 1998. **21**(5): p. 404-10.

63. Ladd, M.E., et al. *RF heating of actively visualized catheters and guidewires*. in *6th Scientific Meeting and Exhibition*. 1998. Sydney Convention & Exhibition Centre: ISMRM.

64. Konings, M.K., et al., *Heating around intravascular guidewires by resonating RF waves.* Journal of Magnetic Resonance Imaging, 2000. **12**(1): p. 79-85.

65. Nitz, W.R., et al., *On the heating of linear conductive structures as guide wires and catheters in interventional MRI.* J Magn Reson Imaging, 2001. **13**(1): p. 105-14.

66. Lauck, G., et al., *Effects of nuclear magnetic resonance imaging on cardiac pacemakers.* Pacing Clin Electrophysiol, 1995. **18**(8): p. 1549-55.

67. Achenbach, S., et al., *Effects of magnetic resonance imaging on cardiac pacemakers and electrodes.* Am Heart J, 1997. **134**(3): p. 467-73.

68. Sommer, T., et al., *MR imaging and cardiac pacemakers: in-vitro evaluation and in-vivo studies in 51 patients at 0.5 T.* Radiology, 2000. **215**(3): p. 869-79.

69. Duru, F., R. Luechinger, and R. Candinas, *MR imaging in patients with cardiac pacemakers.* Radiology, 2001. **219**(3): p. 856-8.

70. Chou, C.K., J.A. McDougall, and K.W. Chan, *RF heating of implanted spinal fusion stimulator during magnetic resonance imaging.* IEEE Trans Biomed Eng, 1997. **44**(5): p. 367-73.

71. Konings, M.K. and C.J.B. Bakker. *Intolerable heating by resonating RF waves around guidewires*. in *7th Scientific Meeting and Exhibition*. 1999. Pennsylvania Convention Centre: ISMRM.

72. Liu, C.Y., et al., *Safety of MRI-guided endovascular guidewire applications.* J Magn Reson Imaging, 2000. **12**(1): p. 75-8.

73. Buchli, R., P. Boesiger, and D. Meier, *Heating effects of metallic implants by MRI examinations.* Magn Reson Med, 1988. **7**(3): p. 255-61.

74. Surowiec, A., et al., *In vitro dielectric properties of human tissues at radiofrequencies.* Phys Med Biol, 1987. **32**(5): p. 615-21.

75. Barnes, F.S. and B. Greenebaum, *Handbook of biological effects of electromagnetic fields. Biological and biophysical aspects of electromagnetic fields*. 3rd ed. 2007, Boca Raton: CRC Press. 440 p.

76. Surowiec, A., et al., *Invitro Dielectric-Properties of Human-Tissues at Radiofrequencies.* Physics in Medicine and Biology, 1987. **32**(5): p. 615-621.

77. Atalar, E. *Safe Coaxial Cables*. in *7th Scientific Meeting and Exhibition*. 1999. Pennsylvania Convention Centre.

78. Syms, R.R.A., L. Solymar, and I.R. Young, *Periodic Analysis of MR-Safe Transmission Lines.* Ieee Journal of Selected Topics in Quantum Electronics, 2010. **16**(2): p. 433-440.

79. Memis, O.G., *Miniaturized fiber optic transmission system for magnetic resonance imaging signals*, in *Electrical and Electronics Engineering*. 2005: the institute of engineering and science of bilkent university.

80. Memis, O.G., et al., *Miniaturized fiber-optic transmission system for MRI signals.* Magn Reson Med, 2008. **59**(1): p. 165-73.

81. Schnall, M.D., et al., *Wireless implanted magnetic resonance probes for in vivo nmr.* J Magn Reson, 1986. **68**: p. 161-7.

82. Scott, G. and K. Yu. *Wireless Transponders for Parallel MRI: Systems Issues*. in *Second International Workshop on Parallel MRI*. 2004. Zurich, Switzerland: ISMRM and ESMRMB.

83. Ladd, M.E. and H.H. Quick, *Reduction of resonant RF heating in intravascular catheters using coaxial chokes.* Magn Reson Med, 2000. **43**(4): p. 615-9.

84. Ladd, M.E. and H.H. Quick. *A 0.7 mm triaxial cable for significantly reducing RF heating in interventional MR*. in *7th Scientific Meeting and Exhibition*. 1999. Pennsylvania Convention Centre.

85. Weiss, S., et al., *Transmission line for improved RF safety of interventional devices.* Magn Reson Med, 2005. **54**(1): p. 182-9.

86. Vernickel, P., et al., *A safe transmission line for MRI.* IEEE Trans Biomed Eng, 2005. **52**(6): p. 1094-102.

87. Krafft, A., et al., *B1 field-insensitive transformers for RF-safe transmission lines.* MAGMA, 2006. **19**(5): p. 257-66.

88. Veselago, V.G., *The Electrodynamics of Substances with Simultaneously Negative Values of ε and μ.* Soviet Physics Uspekhi, 1968. **10**(4): p. 509.

89. Pendry, J.B., *Negative refraction.* Contemporary Physics, 2004. **45**(3): p. 191-202.

90. Pendry, J.B., et al., *Magnetism from conductors and enhanced nonlinear phenomena.* Ieee Transactions on Microwave Theory and Techniques, 1999. **47**(11): p. 2075-2084.

91. Smith, D.R., et al., *Composite medium with simultaneously negative permeability and permittivity.* Phys Rev Lett, 2000. **84**(18): p. 4184-4187.

92. Pendry, J.B., *Negative refraction makes a perfect lens.* Phys Rev Lett, 2000. **85**(18): p. 3966-9.

93. Freire, M.J. and R. Marques, *Planar magnetoinductive lens for three-dimensional subwavelength imaging.* Applied Physics Letters, 2005. **86**(182505).

94. Sun, Z. and I.F. Akyildiz, *Magnetic Induction Communications for Wireless Underground Sensor Networks.* Ieee Transactions on Antennas and Propagation, 2010. **58**(7): p. 2426-2435.

95. Caloz, C. and T. Itoh. *Application of the transmission line theory of left-handed (LH) materials to the realization of a microstrip "LH line".* in *Antennas and Propagation Society International Symposium, 2002. IEEE*. 2002.

96. Eleftheriades, G.V., A.K. Iyer, and P.C. Kremer, *Planar negative refractive index media using periodically L-C loaded transmission lines.* Ieee Transactions on Microwave Theory and Techniques, 2002. **50**(12): p. 2702-2712.

97. Pendry, J.B., D. Schurig, and D.R. Smith, *Controlling electromagnetic fields.* Science, 2006. **312**(5781): p. 1780-1782.

98. Schurig, D., et al., *Metamaterial electromagnetic cloak at microwave frequencies.* Science, 2006. **314**(5801): p. 977-980.

99. Chen, H.S., et al., *Electromagnetic wave interactions with a metamaterial cloak.* Physical Review Letters, 2007. **99**(6).

100. Wu, Q., et al., *Electromagnetic characteristics of metamaterial cloak covered dielectric cylinder illuminated by electric line source.* Iet Microwaves Antennas & Propagation, 2010. **4**(10): p. 1680-1688.

101. Moser, H.O., et al., *Terahertz response of a microfabricated rod-split-ring-resonator electromagnetic metamaterial.* Phys Rev Lett, 2005. **94**(6): p. 063901.

102. Wiltshire, M.C.K., et al., *Microstructured magnetic materials for RF flux guides in magnetic resonance imaging.* Science, 2001. **291**(5505): p. 849-851.

103. Shamonina, E., et al., *Magneto-inductive waveguide.* Electronics Letters, 2002. **38**(8): p. 371-373.

104. Shamonina, E., et al., *Magnetoinductive waves in one, two, and three dimensions.* Journal of Applied Physics, 2002. **92**(10): p. 6252-6261.

105. Shamonina, E., *Slow waves in magnetic metamaterials: history, fundamentals and applications.* Physica Status Solidi B-Basic Solid State Physics, 2008. **245**(8): p. 1471-1482.

106. Wiltshire, M.C.K., et al., *Dispersion characteristics of magneto-inductive waves: comparison between theory and experiment.* Electronics Letters, 2003. **39**(2): p. 215-217.

107. Syms, R.R.A., E. Shamonina, and L. Solymar, *Positive and negative refraction of magnetoinductive waves in two dimensions.* European Physical Journal B, 2005. **46**(2): p. 301-308.

108. Syms, R.R.A., et al., *A theory of metamaterials based on periodically loaded transmission lines: Interaction between magnetoinductive and electromagnetic waves.* Journal of Applied Physics, 2005. **97**(6): p. 064909.

109. Freire, M.J., et al., *Planar magnetoinductive wave transducers: Theory and applications.* Applied Physics Letters, 2004. **85**(19): p. 4439-4441.

110. Freire, M.J. and R. Marques, *Near-field imaging in the megahertz range by strongly coupled magnetoinductive surfaces: Experiment and ab initio analysis.* Journal of Applied Physics, 2006. **100**(6).

111. Nefedov, I.S. and S.A. Tretyakov, *On potential applications of metamaterials for the design of broadband phase shifters.* Microwave and Optical Technology Letters, 2005. **45**(2): p. 98-102.

112. Shamonina, E. and L. Solymar, *Magneto-inductive waves supported by metamaterial elements: components for a one-dimensional waveguide.* Journal of Physics D-Applied Physics, 2004. **37**(3): p. 362-367.

113. Syms, R.R.A., E. Shamonina, and L. Solymar, *Magneto-inductive waveguide devices.* Iee Proceedings-Microwaves Antennas and Propagation, 2006. **153**(2): p. 111-121.

114. Syms, R.R.A., I.R. Young, and L. Solymar, *Low-loss magneto-inductive waveguides.* Journal of Physics D-Applied Physics, 2006. **39**(18): p. 3945-3951.

115. Syms, R.R.A., et al., *Higher order interactions in magneto-inductive waveguides.* Metamaterials, 2007. **1**(1): p. 44-51.

116. Syms, R.R.A. and L. Solymar, *Bends in magneto-inductive waveguides.* Metamaterials, 2010. **4**(4): p. 161-169.

117. Solymar, L., et al., *Rotational resonance of magnetoinductive waves: Basic concept and application to nuclear magnetic resonance.* Journal of Applied Physics, 2006. **99**(12).

118. Syms, R.R.A., L. Solymar, and I.R. Young. *MR-Safe Cables – an Application of Magneto-inductive Waves?* in *Metamaterial's 2009 - 3rd International Congress on Advanced Electromagnetic Materials in Microwaves and Optics*. 2009. London, UK.

119. Syms, R.R.A., et al., *Thin-film magneto-inductive cables.* Journal of Physics D-Applied Physics, 2010. **43**(5).

120. DuPont *DuPont™ Kapton® HN polyimide film - Technical Data Sheet*.

121. Okamoto, K. and S. Kawai, *Electrical-Conduction and Phase-Transition of Copper Sulfides.* Japanese Journal of Applied Physics, 1973. **12**(8): p. 1130-1138.

122. Cardoso, J., et al., *Conductive copper sulfide thin films on polyimide foils for optical and optoelectronic applications.* Modern Physics Letters B, 2001. **15**(17-19): p. 774-777.

123. Solymar, L. and E. Shamonina, *Waves in metamaterials*. 2009, Oxford: Oxford University Press. xvi, 385 p., [16] p. of plates.

124. Syms, R.R.A., L. Solymar, and I.R. Young, *Broadband coupling transducers for magneto-inductive cables.* Journal of Physics D-Applied Physics, 2010. **43**(28).

125. Floume, T.S., R.R.A., *Electric coupling in strongly coupled magneto-inductive cable.* IEEE Trans. Micr. Theory. Tech., 2013.

126. Syms, R., et al., *Magneto-Inductive Catheter Receiver for Magnetic Resonance Imaging.* IEEE Trans Biomed Eng, 2013. **60**(9): p. 2421-31.

127. Nyenhuis, J.A., et al., *MRI and implanted medical devices: basic interactions with an emphasis on heating.* Device and Materials Reliability, IEEE Transactions on, 2005. **5**(3): p. 467-480.

128. De Wilde, J.P., et al., *Magnetic resonance imaging safety issues including an analysis of recorded incidents within the UK.* Progress in Nuclear Magnetic Resonance Spectroscopy, 2007. **51**(1): p. 37-48.

129. Gabriel, C., S. Gabriel, and E. Corthout, *The dielectric properties of biological tissues: I. Literature survey.* Phys Med Biol, 1996. **41**(11): p. 2231-49.

130. Peyman, A., et al., *Variation of the dielectric properties of tissues with age: the effect on the values of SAR in children when exposed to walkie-talkie devices (vol 54, pg 227, 2009).* Physics in Medicine and Biology, 2010. **55**(17): p. 5249-5249.

131. (FCC), F.C.C. *Radio Frequency Safety: Body Tissue Dielectric Parameters Tool*. Radio Frequency Safety 2010 [cited 2012 5 July 2012]; Available from: http://transition.fcc.gov/oet/rfsafety/dielectric.html.

132. CST. *Modeling Temperature Effects of RF Thermoablation in a Human Liver using the Bioheat Formulation in CST STUDIO SUITE*. 2013 [cited 2013; Available from: http://www.cst.com/Content/Applications/Article/Article.aspx?id=387.

133. Park, S.M., et al., *Gelled versus nongelled phantom material for measurement of MRI-induced temperature increases with bioimplants.* Ieee Transactions on Magnetics, 2003. **39**(5): p. 3367-3371.

134. Moore, R., *Effects of a surrounding conducting medium on antenna analysis.* Antennas and Propagation, IEEE Transactions on, 1963. **11**(3): p. 216-225.

135. International, A.S.o.T.a.M.A., *F2182-11a Standard Test Method for Measurement of Radio Frequency Induced Heating On or Near Passive Implants During Magnetic Resonance Imaging*. 2005, ASTM.

136. Syms, R.R.A., et al., *Magnetic resonance imaging using linear magneto-inductive waveguides.* Journal of Applied Physics, 2012. **112**(11).

137. Gibson, W.C., *The method of moments in electromagnetics*. 2008, Chapman & Hall/CRC: New York.

138. corp., A., *AWRDE Simulation and Analysis Guide* 2010, awrcorp.com.

139. Inc., A.W.R., *Layout-driven high frequency design gets boost from new em technology.* MICROWAVE JOURNAL, 2007.

140. International, A.S.o.T.a.M.A., *D150-11 Standard Test Methods for AC Loss Characteristics and Permittivity (Dielectric Constant) of Solid Electrical Insulation*. 2013, ASTM.

141. *Dissipation Factor (DF)*. Available from: http://www.cartage.org.lb/en/themes/sciences/physics/electromagnetism/electrostatics/Capacitors/Applications/BasicConsiderations/BasicConsiderations.htm.

142. Ramo, S., J.R. Whinnery, and T.V. Duzer, *Fields and Waves in Communication Electronics*. 1994, New York: John Wiley and Sons.

143. S., K., et al. *Comparison of methods for the dissipation factor measurement at practical example*. in *the 16th International Symposium on High Voltage Engineerin*. 2009. Innes House, Johannesburg: TUGRAZ [online].

144. Hague, B. and T.R. Foord, *Alternating current bridge methods*. 6th ed ed. 1971, London: Pitman.